Dynamics, Mechanics and Stability of Physical Gels

Thesis by
Ahmad Khalid Omar

In Partial Fulfillment of the Requirements for the
Degree of
Doctor of Philosophy

CALIFORNIA INSTITUTE OF TECHNOLOGY
Pasadena, California

2019
Defended June 3, 2019

Ahmad Khalid Omar
ORCID: 0000-0002-6404-7612

ACKNOWLEDGEMENTS

I will always look back at my time at Caltech as some of my most formative years due, in large part, to working with Prof. Zhen-Gang Wang. His example as a scholar has indelibly shaped my identity as a researcher and teacher. I will always be thankful for the intellectual freedom Zhen-Gang afforded me in allowing me to pursue any idea or collaboration that I was interested in. His patience and compassion during the difficult personal times I experienced in the fourth year of my Ph.D. are qualities of his that I will never forget.

I am thankful for my committee members, who have all served as great scientific mentors and have helped shape this work. Spending several hours in the afternoon discussing (arguing) science with Prof. John Brady (my "unofficial" co-advisor) was one of the highlights of my Ph.D. I am grateful for his generosity with both his time and knowledge. My collaboration with the group of Prof. David Tirrell was an invaluable experience. His scientific and professional guidance has made a lasting impact on me. I learned a great deal on associative polymers from my conversations with Prof. Julie Kornfield. The clarity of Prof. Julie Kornfield's lectures, both in the classroom and research context, set a standard that I can only hope to approach.

The Chemical Engineering staff have made my time at Caltech profoundly easier. Special thanks go to Kathy Bubash, Allison Ouellette, Sohee Lee and Martha Hepworth. Suresh Guptha, who patiently helped me solve an innumerable amount of computer problems, was a constant source of great conversations.

Collaborating with Peter Rapp was a terrific experience, both personally and scientifically. I am thankful for his patience in teaching me about "real" (e.g., experimental) polymeric systems. I had the privilege of mentoring Chloe Gao and Yanze Wu, two amazing summer undergraduate research students that brought much joy to the Wang and Brady groups.

My time in Zhen-Gang's group was made all the more enjoyable by the time I spent with Dr. Umi Yamamoto, Dr. Pengfei Zhang, Dr. JJ, Dr. ChangYun Son, Dr. Huikuan Chao, Dr. Nuo Wong, Dr. Rui Wang, Dr. Bilin Zhuang, Dr. Kevin Shen, Hyeongjoo Row, Andy Ylitalo, Chris Balzer, Rachel Krueger and Alex Vaschillo. Bilin, Kevin and Umi welcomed me into the group and were always a source of guidance, advice and laughs. Pengfei's unwavering optimism and happiness were a source of inspiration and I'll always look back fondly on JJ's stories. I would also

like to thank some of the many visitors that have passed through the Wang group, including Prof. Yuci Xu. The six months Prof. Frank Bates stayed with our group was one of the most illuminating and enjoyable periods of my time at Caltech.

Dr. Marco Heinen, Dr. Mu Wang, Dr. Wen Yan, Dr. Sho Takatori, Dr. Kevin Marshall, Dr. Eric Burkholder, Dr. Stewart Mallory, Dr. Karol Makuch, Austin Dulaney, Camilla Kjeldberg, Zhiwei Peng, Charlie Slominski, Isaac Fees and Mikey Phan from the Brady group were a great source of community and knowledge. Marco's mentorship during the early years of my Ph.D. shaped much of my scientific approach. Charlie, Isaac, Austin and Stew were terrific office mates and the source of countless discussions on science, sports, politics, etc. Life at Caltech would not have been the same without my friends and classmates, including Nick Porubsky and Mikey Phan.

Most importantly, I would like to thank my family. The seemingly endless sacrifices that my parents, Khalid and Azza, have made for me and my siblings to pursue our dreams are awe-inspiring. I do not have the words to fully express my gratitude to them. My brother, Amr, and sister, Salma, have been great sources of joy and inspiration throughout my life. From volunteering to assist me in traveling to conferences to visiting me in Pasadena, they have helped make this thesis possible.

I would also like to acknowledge support by the National Science Foundation Graduate Research Fellowship under Grant No. DGE-1144469 and an HHMI Gilliam Fellowship. These funding sources helped provide me with the freedom necessary to pursue some of the ideas presented in this work.

ABSTRACT

From the commercial products that we encounter in our daily lives to the mucous that lines our gut, gels assembled by the reversible association of polymers or colloids are a ubiquitous, important and fascinating class of soft materials. The dual solid and fluid-like (viscoelastic) properties of associative polymer gels render them useful in a number of applications including as tissue-regeneration scaffolds, drug delivery vectors and organic electronics and batter technologies. However, there remains a number of open questions regarding the microscopic origins of many of the dynamical and mechanical properties that make these materials so appealing. The wide range of length and timescales in physical gels present a formidable challenge towards the formulation of a complete microscopic dynamical and rheological portrait. My work has focused on the development of microscopically-informed and experimentally verifiable explanations for some of the fundamental dynamical and mechanical properties of associative gels. I first present our viewpoint, informed by computer simulation and experiment, on the origin of the long-time self-diffusivity of telechelic polymer gels. Our perspective and resulting theory compare favorably with experiments. Shearing an associative polymer gel is found to result in the emergence of new diffusive modes with applied shear that are can destabilize homogeneous flow for gels sufficiently close to the two phase boundary. This finding motivates the idea that nonequilibrium forcing may promote the relaxation of arrested colloidal materials, such as a colloidal gel, closer to their thermodynamic ground state. The driving force need not be externally applied. The induced collective motion in colloidal gels subject to internal driving forces (such as the presence of a small fraction of self-propelling colloids) can drive the system from a state of arrested metastablity to a state of lower free energy. I conclude by showing that the internal stress generated by the self-propelling particles – the active stress – is not a "true" stress, but rather an equivalent stress analogous to the dynamic pressure of fluids in a gravitational field. The importance of this finding is demonstrated in resolving the perplexing finding of a negative surface tension in phase separated active materials.

PUBLISHED CONTENT AND CONTRIBUTIONS

[1] Rapp, P. B.; Omar, A. K.; Shen, J. J.; Buck, M. E.; Wang, Z.-G.; Tirrell, D. A. Analysis and Control of Chain Mobility in Protein Hydrogels. *J. Am. Chem. Soc.* **2017**, *139*, 3796–3804. DOI:10.1021/jacs.6b13146.

[2] Omar, A. K.; Wang, Z.-G. Shear-Induced Heterogeneity in Associating Polymer Gels: Role of Network Structure and Dilatancy. *Phys. Rev. Lett.* **2017**, *119*, 117801. DOI:10.1103/PhysRevLett.119.117801.

[3] Rapp*, P. B.; Omar*, A. K.; Silverman, B. R.; Wang, Z.-G.; Tirrell, D. A. Mechanisms of Diffusion in Associative Polymer Networks: Evidence for Chain Hopping. *J. Am. Chem. Soc.* **2018**, *140*, 14185–14194. DOI:10.1021/jacs.8b07908.

[4] Omar, A. K.; Wu, Y.; Wang, Z.-G.; Brady, J. F. Swimming to Stability: Structural and Dynamical Control via Active Doping. *ACS Nano* **2019**, *13*, 560–572. DOI:10.1021/acsnano.8b07421.

In all of the above, A.K.O. participated in the conception of the project, conducted calculations, analyzed the data and participated in the writing of the manuscript.

TABLE OF CONTENTS

Acknowledgements . . . iii
Abstract . . . v
Published Content and Contributions . . . vi
Bibliography . . . vi
Table of Contents . . . vii
List of Illustrations . . . viii
Chapter I: Introduction . . . 1
1.1 Physical Gelation . . . 2
1.2 Dynamical and Rheological Perspectives in Associating Polymers . . . 5
1.3 (Thermo)Dynamic Phase Diagram . . . 6
1.4 Thesis Outline . . . 10
Chapter II: Dynamics of Associative Polymers: Theory and Experiment . . . 18
2.1 Introduction . . . 19
2.2 Theory . . . 21
2.3 Statistical Mechanics of Chain Binding . . . 22
2.4 Quantitative Comparison to Theory . . . 31
2.5 Evidence for Multisticker Chain Hopping . . . 35
2.6 Conclusions . . . 38
2.7 Appendix . . . 39
Chapter III: Nonlinear Dynamics and Rheology of Associating Polymer Gels 53
3.1 Introduction . . . 53
3.2 Equilibrium Properties . . . 56
3.3 Shear-Concentration Coupling . . . 59
3.4 Network Dilation and Shear-Induced Diffusion . . . 60
3.5 Conclusions . . . 62
3.6 Appendix . . . 63
Chapter IV: Swimming to Stability: Structural and Dynamical Control of a Colloidal Gel via Active Doping . . . 70
4.1 Introduction . . . 71
4.2 Active Matter for Colloidal Stability . . . 72
4.3 Microscale Origins of Dynamic Phase Behavior . . . 79
4.4 Conclusions . . . 91
4.5 Appendix . . . 93
Chapter V: Interfacial Mechanics of Active Matter . . . 101
5.1 Introduction . . . 101
5.2 Stress Generation and the Active Interface . . . 105
5.3 Conclusions . . . 110
5.4 Appendix . . . 110

LIST OF ILLUSTRATIONS

Number *Page*

1.1 (Top) A macroscopic sample of an associating polymer gel (adapted from Olsen et al. [21]) formed by a telechelic protein-based polymer and (bottom) a confocal image of a colloidal gel (adapted from Hsiao et al. [22]) formed by a colloid and polymer depletant mixture. 3

1.2 Rheological theories for telechelic associating polymers are often based on a "three-state" model wherein the chain can either be have two (bridge or loop configuration), one (dangle configuration), or none (free configuration) of its sticky ends bound to a (static) infinite elastic network. 4

1.3 (A) Schematic of a dynamic phase diagram of a generic physical gel. For system-specific versions of this phase diagram see, for example, Kumar and Douglas [30] for an associating polymer version and Lu et al. [25] for a colloidal gel version. (B) The phase separation process of a (patchy) attractive colloidal suspension, adapted from Ruzicka et al. [54]. The insets display the waiting time beginning after the sample preparation time. (C) Hypothetical dynamic free energy landscape of a coarsening attractive colloidal suspension. 8

1.4 (Left) extension of the canonical equilibrium phase diagram to a nonequilibrium dimension. The manner in which the external force is applied can have a profound influence of the system symmetries (see right, adapted from Chen et al. [68]). 9

2.1 Diffusive migration of associative polymer chains through reversible networks can occur via partial or complete disengagement of the associative segments, i.e., by "walking" or "hopping". Here we provide evidence that $D_{hop} \gg D_{walk}$ in model networks. 20

2.2 Schematic representation of telechelic chain partitioning in reversible networks. (A) Two equilibrium constants K_1 and K_2 control chain partitioning among three sequential states: free (f), dangle (d) and bound (b). The bound state consists of bridges (B) and loops (L). (B) Local network structure affects the binding equilibrium of telechelic chains. When the chain size (N) and mesh size (M) are the same, an entropic penalty for bridge formation manifests as binding asymmetry ($K_1 > K_2$). As the chains become larger than the mesh, the difference in binding strengths decreases to the mean-field limit ($K1 \approx 4K_2$). 23

2.3 Experimental binding constant ratios inferred from diffusion measurements: correspondence to theory supports chain hopping. (A) Elastin-like probes with different lengths and numbers of stickers were placed in size-matched ($N = M$) and mismatched ($N \neq M$) "n-mesh" PEnP networks. Equilibrium constants were inferred from FRAP diffusivity measurements via eq. (2.4), i.e., assuming exclusive hopping. Estimating a single K_1/K_2 ratio requires independent diffusivity measurements from three different probe types having zero (En*), one (EnP*) or two (PEnP*) stickers. (B) Representative diffusivities in a 6-mesh (80 total measurements, ≥ 4 per probe type). Approximate molecular weight exponents for each probe type were estimated from coarse power-law fits (see discussion in main text). (C) The experimental K_1/K_2 data (mean ± std. dev.) in the 6-mesh reveal binding asymmetry for telechelic chains. The data are plotted against the dimensionless probe size $r \equiv R_{probe}/R_{mesh} \sim b_k N^{1/2} M^{-1/3}$. The "loop-free" prediction from eq. (2.3) and the single-parameter fit of eq. (2.2) with $x_{min} = 0.26$ are shown; $x_{min} = l_{min}/c$ is the best-fit dimensionless integration limit for the looping configurational Ω_L (see discussion in main text). (D) Loop subtraction with $x_{min} = 0.26$ permits comparison of the K_1/K_2 data from each mesh to eq. (2.3) (shown are mean K_1/K_B ratios deduced from 298 total measurements, ≥ 4 per probe type). Error bars in panel D are omitted for clarity, but are analogous in size to those in panel C. The dotted line represents the mean-field limit $K_1/K_B = 4$. 30

2.4 Concentration dependence of the binding constant ratio in a 6-mesh network. K_1/K_2 is proportional to ϕ_j (junction density) for small ϕ_j, then falls sharply above $\phi_j \approx 0.04$ due to a decrease in junction spacing. Equation (2.2) qualitatively captures this behavior, with $x_{min} = 0.37 \pm 0.05$, $b = 0.95$ nm and $N = 72$. Error bars depict mean ± std. deviation from $n = 76$ total measurements, with ≥ 2 measurements per probe type per concentration. The mass concentrations range from $5-25\%$ (w/v), i.e., $\rho = 50-250$ mg/mL. 34

2.5 Hopping dominates the diffusion of multisticker chains in telechelic networks. (Top) Measurements of K_{eff} inferred from experimental D_S and eqs. 4 and 5 are in good agreement with model predictions for chains with $S = 2, 3$ and 5 associative domains. (Bottom) Comparison of D_S measured by FRAP and D_{hop} predicted from the thermodynamic model. All measurements were taken in 10% (w/v) 6-mesh networks using size-matched probes (i.e., the intersticker spacing N corresponds to the mesh size M). Symbols depict mean ± std. deviation from $n \geq 4$ measurements per probe type. All model predictions were made using $x_{min} = 0.26$. The prediction from Baxandall assumes $D_S \sim S^{-1}$. "No local order" assumes that all binding events have the same strength as the first association, i.e., all $K_i = K_1$. The theoretical mobility of bound chains is calculated as $D_{walk} = R_{mesh}^2/6\tau_b = 1.61 \times 10^{-5} \mu m^2 s^{-1}$. 37

2.6 Binding configurations of a chain with $S = 3$ stickers. The chain has $k \leq C(S,i)$ possible bound states for each $i \leq S$ number of bound stickers, where $C(S,i)$ is the binomial coefficient. The sum $j = S - 1$ runs over the total number of independent blocks. 42

2.7 Asymmetric binding model is invariant with cluster size "c" for fixed "$x \equiv l/c$". Shown are predictions from eq. (2.2) as a function of the reduced probe size $r \equiv R_{probe}/R_{mesh} \sim N^{1/2}M^{-1/3}$ for various choices of the cluster size "c" and the integration limit for the looping integral "l." (A) The cluster dimension was taken to be $c = 1-5$ nm, $R_{mesh} = 10$ nm, $b_k = 1$ nm and x (dimensionless) was fixed at 0.5. Equation (2.3) was used to plot the "loops off" case. The behavior of eq. (2.2) is approximately invariant under several choices of $c < R_{mesh}$. (B) For a fixed choice of cluster size of $c = 1$, the limits of the looping integral (specified by $x = l/c$) determine the behavior of eq. (2.2). For all predictions described in the main text, $c = 1.89$ nm was employed based on the molecular weight of the P domain. 46

2.8 Selection criteria for the limits of the looping integral. In order to estimate $\Omega_L/\phi_j = f(l)$ in a non-arbitrary way, estimates for the upper integration limit $l = xc$ are required (using $c = 1.89$ nm). (Top) Matching the experimental fraction of elastically effective chains to predictions from eq. (2.13) fixes this limit precisely, providing x_{rheo} for each mesh. (Bottom) Alternatively, varying l in order to minimize the residuals between experimental K_1/K_2 values and constrained fits from eq. (2.2) provides x_{min}. The integration limits obtained by either method are similar across all four meshes and are presented in Table 2.3. 47

2.9 Single-parameter "best fits" of eq. (2.2) to experimental K_1/K_2, analogous to Fig. 2.3C. Shown are experimental values of K_1/K_2 measured in each mesh (298 total measurements, ≥ 4 per probe, error bars represent mean $\pm$ std. dev.), together with single-parameter "best fits" from eq. (2.2) using $x_{min} = l_{min}/c$ obtained from residuals minimization and the universal "loop-free" prediction from eq. (2.3). $x_{min} = 0.26$ from the 6-mesh was used to construct the "master curve" in Fig. 2.3D, as well as to predict hopping for the multisticker probes in Fig. 2.5. 48

3.1 Effect of T^* on (a) the weight-averaged cluster size distribution; (b) τ, D, $\sigma_{xz,\gamma}$ and Π. The subscript R indicates properties of our Rouse system with $D_R = 6 \times 10^{-3}$ and $\Pi_R = 8.9nkT$. G_0 is the gel shear modulus at $T^* = 0.174$. 56

3.2 (a) Constitutive curves (obtained with a combination of sweep and startup protocols) for gel at $T^* = 0.174$ and for the Rouse solution. The insets display the AP velocity and density profiles at various shear rates. (b) Profiles for concentration ρ, velocity u ($U_{max} = \dot{\gamma}L_z$), bridging density n_B and cluster functionality f. The subscript eq denotes equilibrium properties. (c) Snapshot of banded flow (only stickers are shown for clarity). 58

3.3 (a) $(\Pi_{zz} - \Pi_{eq})/\Pi_{eq}$ as a function of $\dot{\gamma}$ and T^*. (b) Influence of $\dot{\gamma}$ on the cluster size distribution of the AP gel ($T^* = 0.174$). (c) Weight-averaged DRA size distribution (with the chains binned into groups of 20) excluding clusters with $Z_c < 4$. (d) Diffusivity in the gradient D_{zz} and vorticity D_{yy} directions in the regime of homogeneous flow. (e) Breakup of a single space-spanning DRA at equilibrium (left) to several smaller DRAs (indicated by different colors) during steady shear at $\dot{\gamma} = 10^{-2}$ (right). Stickers not belonging to a DRA are shown in gray. 61

3.4 Magnitude of the density heterogeneity at $k = 2\pi/L_z$ for an AP at $T^* = 0.174$ and for the Rouse solution. The subscript eq denotes equilibrium properties. 63

3.5 (a) $(\Pi_{zz} - \Pi_{eq})/nkT$ and (b) Π_{zz}/nkT as a function of $\dot{\gamma}$ for gels of various T^* and Rouse system. 64

3.6 The relative degree of chain extension in the flow (x) and gradient (z) directions for AP gel at $T^* = 0.174$ (□) and the Rouse solution (○) for $\dot{\gamma}$ in which the flow is homogeneous. 65

3.7 Trimming of the AP gel network at $T^* = 0.174$ and $\dot{\gamma} = 10^{-2}$ with the DRA analysis. 65

4.1 Physical schematic (left) of the key parameters characterizing active particle motion: persistence and swim force quantified by Pe_R and Pe_S, respectively. The sketched swimmers have the same size and Brownian diffusivity and only differ in the underlying microscopic swimming dynamics. Variation in the spatial extent of the trajectories is intended to highlight contrasts in the swim diffusivity, while increased thickness of the trajectory-lines reflects larger swim speeds/forces. Schematic (right) of the pivotal role that the swim force plays in materials with attractive interactions. The potential energy displayed is the Morse potential that is utilized in our simulations. . 73

4.2 (A) Representative snapshots of system configurations with like-shaded snapshots representing groupings between dynamically or structurally similar regions in $\mathrm{Pe}_R - \mathrm{Pe}_S$ space. Active particles are shown in red. (B) Dynamic evolution of q_1 as a function of persistence as $\mathrm{Pe}_S \rightarrow \mathrm{Pe}_S^*$. (C) Area fraction distribution (obtained by equally dividing the system area into square subareas and computing the local area fraction in each region) as a function of persistence. (D) Dominant (inverse) length scale in the system (q_1) as a function of Pe_S and Pe_R with interpolation/smoothing applied between 55 discrete points to achieve a continuous representation. 75

4.3 (A) Coarsening rate for passive and active systems measured as a function of the initial characteristic length scale L of the material and over a duration of $100\tau_B$. The passive coarsening rate was measured by simply "turning off" the activity of the swimmers in the active system. (B) Schematic of interfacial free energy of a coarsening network as a function of "coarsening events" for two possible mechanisms. (C) Nonswimming and (D) swimming component of the system pressure as a function of Pe_S (note that we have scaled out the effect of persistence in panel D). 80

4.4 (A) The probe-swimmer size ratio and swimmer persistence length dependence of the mechanical depletion force with the lines representing eq (4.4). The nonmonotonic region is magnified here, while the inset displays the complete data in its entirety. (B) Swimmer-probe contact statistics as a function of the (left) persistence (with $\mathrm{Pe}_R = 1, 0.5, 0.1, 0.05$) and (right) size ratio (symbols are the same as in panel A). (C) Representative snapshots after $100\tau_B$ of a three-dimensional system of monodisperse active particles (not shown) and polydisperse (5%) passive particles at volume fractions of $\phi_A = 0.02$ and $\phi_P = 0.20$, respectively, with $\mathrm{Pe}_S/\mathrm{Pe}_S^* = 200$ and (left) $\mathrm{Pe}_R = 10^{-2}$ and (right) $\mathrm{Pe}_R = 1$. Particles are colored by coordination number to aid in cluster visualization. 84

4.5 (Top) Rows represent the time evolution of a prepared passive disk consisting of either monodisperse or polydisperse particles with and without surrounding active particles with $\mathrm{Pe}_S/\mathrm{Pe}_S^* = 1.25$ and $\mathrm{Pe}_R = 10^{-2}$ (e.g., the activity-induced repulsion regime). (Bottom) Time evolution of a monodisperse system with identical parameters as the above disk simulations but beginning from a spatially homogeneous configuration. Active particles are shown in red. 87

4.6 Qualitative illustration of both the rapid coarsening in the activity-induced attraction regime and the transition from bicontinuous to droplet-like spinodal decomposition with increasing Pe_S for $\mathrm{Pe}_S > \mathrm{Pe}_S^*$ and $\mathrm{Pe}_R = 1$. Active particles are shown in red. The left-most column illustrates the coarsening process for a passive system. 90

4.7 Dynamic phase diagram of an active doped gel. Materials embedded with active particles in the microscopic straining regime will exhibit improved coarsening rates on length scales L that correlate with swimmer persistence l_p. The regimes of activity-induced attraction/repulsion are due to depletion-like forces and are separated by a geometrically controlled boundary that depends on β_{eff} and Pe_R. 91

5.1 (A) A spherical active "liquid" droplet with a system total of 108000 active particles (volume fraction of $\phi = 4\pi a^3 n_0/3 = 0.14$ where n_0 is the number density) with $\mathrm{Pe}_R = 0.0025$ and $\mathrm{Pe}_S = 0.01$. (B) A characteristic simulation snapshot for $\mathrm{Pe}_R = 0.0025$ and $\phi = 0.15$ with 148716 particles and an asymmetric box with dimensions $L_z = 5L_x = 5L_y$. (C) The accompanying number density, polar order and nematic field profiles along the long axis (z) of the simulation cell. The data is translated such that the dense phase is centered along the long axis. Shaded regions represent the domains in which active particles are preferentially oriented tangential to the interface ($Q_{yy} > 0$). 104

5.2 (A) A 2D schematic system of active Brownian particles near an impenetrable hard wall. For $k_s T_s / k_B T = 5$ (B) the number density, polar order and nematic fields and the (C) force flux, number density and local stress profiles. 106

5.3 (A) The directly measured interparticle stress profile and the profile predicted through the integral of the swim force density for the identical system in Fig. 5.1C. (B) The difference in the swim pressure between the liquid and gas phases for various values of Pe_R. 107

5.4 (A) The surface tension of active particles obtained through use of the true stress (○) of active particles (see (B) for a magnified view) in comparison to that obtained by using the active stress (□). 109

5.5 Region of the coexistence curve explored in this work (obtained via simulation). 111

5.6 Schematic for computing the local stress (flux of force across a plane). . . . 112

5.7 Schematic of the interfacial mechanical balance used to define the surface tension. The dashed red box represents a 2D projection of the original control volume and the dotted blue line represents the isochorically deformed volume. 115

Chapter 1

INTRODUCTION

This introductory chapter provides an overview of the basic properties of physical gels and the contexts in which they appear. We outline some of the open questions that motivated this work and provide a brief overview of the background necessary to begin to answer these questions. Subsequent chapters present theoretical arguments, computational evidence and experimental corroboration of our molecular perspective on physical networks.

This chapter includes content from our previously published articles:

Rapp*, P. B.; Omar*, A. K.; Silverman, B. R.; Wang, Z.-G.; Tirrell, D. A. Mechanisms of Diffusion in Associative Polymer Networks: Evidence for Chain Hopping. *J. Am. Chem. Soc.* **2018**, *140*, 14185–14194. DOI:10.1021/jacs.8b07908

Omar, A. K.; Wang, Z.-G. Shear-Induced Heterogeneity in Associating Polymer Gels: Role of Network Structure and Dilatancy. *Phys. Rev. Lett.* **2017**, *119*, 117801. DOI:10.1103/PhysRevLett.119.117801

Omar, A. K.; Wu, Y.; Wang, Z.-G.; Brady, J. F. Swimming to Stability: Structural and Dynamical Control via Active Doping. *ACS Nano* **2019**, *13*, 560–572. DOI:10.1021/acsnano.8b07421

1.1 Physical Gelation

There is perhaps no material in the field of soft matter that is as appreciated and recognized by the public as gels are. From commercial food and health and beauty products to natural biological gels such as mucous [1–3] and bacterial biofilms [4], gels permeate our daily life in enumerable ways, both directly and indirectly. One can appreciate that these materials can flow much like a simple liquid, but retain their shape for long times while at rest like a solid – characteristics of a classic viscoelastic material [5]. In fact, a hallmark of these materials is that, despite having solid-like properties, they are predominantly comprised of simple liquids (e.g., water). In addition to solvent, gels contain polymeric or colloidal species that are "connected" (see Fig. 1.1) in such a way that, despite the individual building blocks only ranging from nanometers to tens of microns in size, they form a macroscopic, space-spanning (percolating) network. When the building blocks (colloids or polymers) of the gel are permanently cross-linked together the network itself becomes a *macroscopic molecule*, endowing the entire material with solid-like properties [5].

Polymer gels have received considerable attention across a number of disciplines due in large part to the potential applications of these materials. In biological contexts, gels can provide structural support in aqueous environments while being minimally invasive, making them strong candidates as potential drug delivery vectors, tissue engineering scaffolds [6] and wound-healing materials [7]. Historically, the early polymer gels designed for many of these applications had, much like a rubber (which can be thought of as a sort of "dry gel"), permanent cross-links that keep the network together. The use of *physical* cross-links – cross-links formed due to weak (on the order of the thermal energy) attractive bonds (e.g., hydrogen bonding [8–11], metal-ligand coordination [10, 12–17] or hydrophobic forces [8, 18–21]) – offer a number of potential advantages. For example, many of the aforementioned applications subject gels to harsh mechanical deformations that could rupture the cross-links of the network. For a covalently cross-linked gel, this damage would be irreversible and would permanently impact the functionality of the material. However, a physical network has a thermodynamic driving force to self-heal and in principle (and, provided enough time, in practice) would recover its functionality entirely. Olsen et al. [21] demonstrated exactly this using a protein-based polymer gel (with the cross-links consisting of physical coiled-coil bundles), which was found to completely self-heal after strong shear deformations (see Fig. 1.1).

In contrast to physical polymer gels (also known as associating polymer gels), *col-*

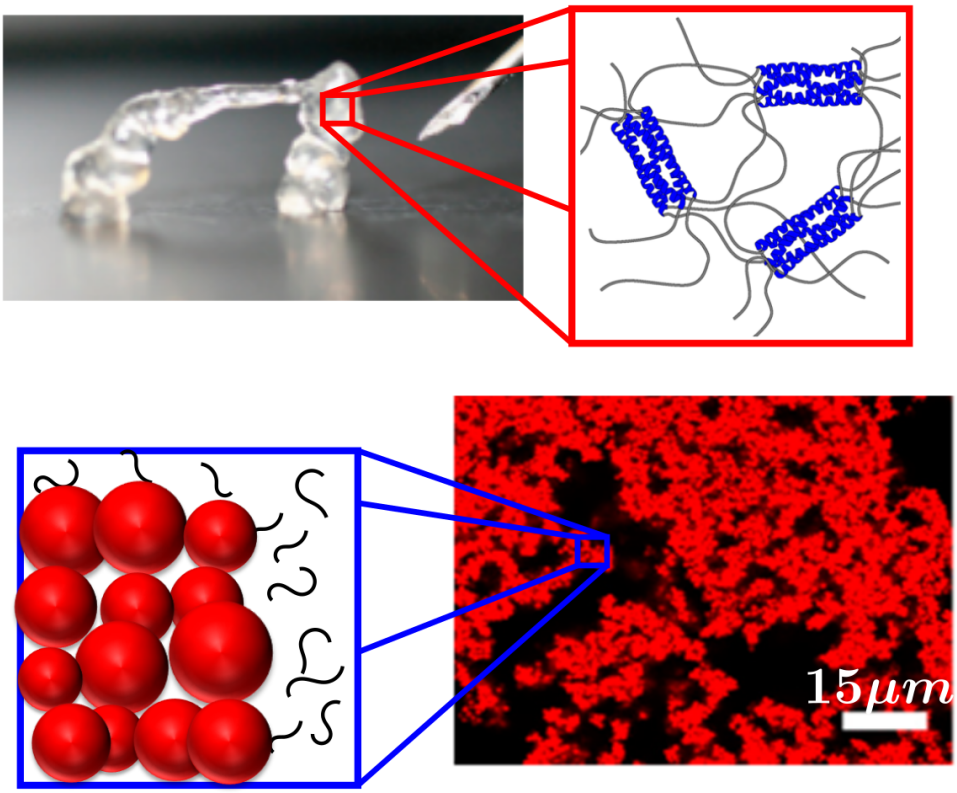

Figure 1.1: (Top) A macroscopic sample of an associating polymer gel (adapted from Olsen et al. [21]) formed by a telechelic protein-based polymer and (bottom) a confocal image of a colloidal gel (adapted from Hsiao et al. [22]) formed by a colloid and polymer depletant mixture.

loidal gels [22] – formed by attractive colloidal particles – have "weak" mechanical properties, which, along with a number of other considerations, makes them less suited for many technological applications. In fact, colloidal gels are argued to be kinetically frustrated, metastable states that are often technologically *undesirable* in comparison to the minimum free energy configuration of the colloidal material. The classical system that demonstrates this issue of kinetic frustration is perhaps also the simplest: a colloidal suspension of spheres with short-range isotropic attractive interactions induced by a polymer depletant [23, 24]. While the equilibrium phase diagram of this system predicts fluid-solid coexistence for interaction strengths as little as a few times the thermal energy k_BT, in practice the system is found to form a long-lived space-spanning network – a gel – for nearly the entire coexistence region [25].

The above considerations motivate two broad challenges that are the focus of this

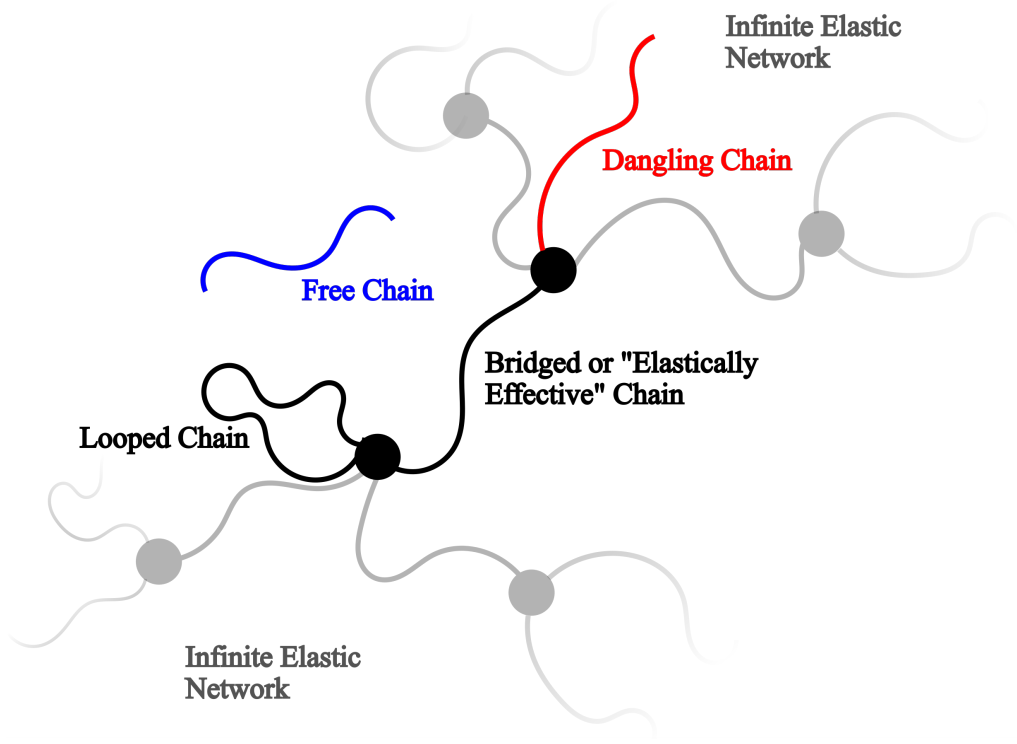

Figure 1.2: Rheological theories for telechelic associating polymers are often based on a "three-state" model wherein the chain can either be have two (bridge or loop configuration), one (dangle configuration), or none (free configuration) of its sticky ends bound to a (static) infinite elastic network.

thesis. First, despite a wealth of theoretical investigations [26–30], the physical microscopic origin of some of the more fundamental dynamical and mechanical properties of associating polymer gels remain unknown. My aim is to develop a microscopically informed, experimentally verifiable perspective on properties such as self-diffusion and the response to simple shear of an associating polymer gel. Second, while the dynamics and rheology of colloidal gels are increasingly well understood (in part because, in contrast to polymer gels, the microscopic dynamics of colloidal gels can be directly visualized in real-space), the development of general routes for the prevention of colloidal materials from being trapped in the oft-undesired gel state remains an open problem. With that in mind, my second aim is to construct a general procedure for pushing frustrated colloidal materials to their minimum free energy configuration. Below I briefly provide some additional considerations and background necessary to understand and appreciate each of these aims.

1.2 Dynamical and Rheological Perspectives in Associating Polymers

The formulation of rheological constitutive models for polymer gels has been a significant, decades-long challenge in polymer physics [31, 32]. The primary system of interest has been telechelic polymers – linear chains with each end capped with an associative or "sticky group." If one takes a single-chain perspective, a chain can exist and reversibly convert between three possible states: having none, one or both of its sticky ends in an associative state, shown schematically in Fig. 1.2. In fact, this is the physical basis for most constitutive theories of telechelic associating polymer gels which, rather than attempt to self-consistently model the network, simply presuppose the existence of a network. When using this model to, for example, describe associating polymers in shear flow, the bridged chains are assumed to affinely deform with the infinite network until one of the ends is forced to unbind from the network to relax the chain stretch. It is the elasticity of the bridged chains that dominate the predicted rheological response as free, dangle and loop configurations only contribute to the dissipative response of the solution.

The so-called transient network theories [18, 31, 33–35] described above have been shown to capture shear thinning and other common rheological responses. But there remain several potential problems with this perspective. While the assumption of an infinite elastic network is appropriate in quiescence and linear-response, an infinite elastic network can no longer exist under steady flow; the network must break up in order to flow. One may argue that, from the perspective of an individual chain, whether the network is infinite or simply much larger than the size of the chain is irrelevant, which is correct in a mean-field sense. However, mechanical properties, such as the osmotic pressure, should sensitively depend on the details of the network connectivity. In fact, these models often entirely focus on the elastic component of the stress and completely neglect the osmotic pressure of the gel, which is crucial for describing a number of rheological phenomena. Most notably, experiments and simulations of associative networks (including both associating polymer [36–38] and colloidal [39] gels) under simple shear have observed spatial inhomogeneities in both shear rate and density, suggesting some form of shear-gradient concentration coupling (SCC) [40–43] similar to that observed in unassociative polymer solutions [44, 45].

Rubinstein and Semenov [29] argued that stress relaxation is dictated by finite-sized (but extremely large near the gel point) clusters of chains that relax by both self-diffusion and internal rearrangements. Describing the mechanical response of

the network on the level of clusters of chains (as opposed to individual chains) is appealing for a number of reasons. In addition to allowing one to take a more realistic view of the network under flow, this approach is more readily extended to associating polymers with multiple sticker groups along their backbone as these chains cannot be described by the traditional three simple states (Fig. 1.2) as telechelics can.

While the above issues are, in my view, problematic for the general use of the transient network perspective in the rheological context, they are perhaps less of a problem in quiescence. In fact, it is appealing and perhaps appropriate to take a single-chain perspective in describing associating polymer self-diffusion in quiescence. Despite nearly 30 years of conceptual development [26, 46], no single mechanistic picture for the self-diffusivity of an associating polymer has found quantitative experimental validation. This stands in contrast to our more complete understanding of self-diffusion in unassociative polymer solutions, for which mechanisms such as reptation find strong experimental support [47–50].

In recent years, while it has been asserted that long-time diffusion in associating polymers is controlled by the "free" state of the chain [17, 20, 46], no systematic investigation has in fact confirmed this molecular picture. While the diffusivity of a free chain is surely significantly larger than that of any of the "bound states", the probability of a chain occupying the free state is, for most experimental systems, quite small. Recent experiments by Rapp et al. [51] have suggested that if one goes beyond the traditional transient network by incorporating some non-mean-field effects in the single-chain thermodynamics, one might predict enough free chains to describe the measured self-diffusion constant.

1.3 (Thermo)Dynamic Phase Diagram

In the case of gels with permanent (covalent) cross-links, the onset of gelation is well-described by percolation theory [5]. For physical gels, however, the gelation transition is a *dynamical transition*. Kumar and Douglas [30] used computer simulations of an associating polymer solution to show that the onset of gelation coincided with both a dramatic slowing down of the polymer dynamics in addition to a marked change in the heat capacity of the solution. The phase diagram for this system is described with the reduced temperature T^* which is the ratio of the thermal energy to the magnitude of the sticker attraction and volume fraction of polymer ϕ. Figure 1.3A shows a schematic of the findings of Kumar and Douglas, who observed the associating polymer gelation transition to occur just before an

association-driven phase separation. Moreover, they extrapolated that the point in which polymer dynamics would become vanishingly small would be within the two phase boundary. While it should be appreciated that the relative locations of these boundaries are highly system specific, the order in which they occur is likely not.

In contrast to associating polymers, gelation in colloidal gels has been argued to be an arrested phase separation with the gelation boundary being synonymous with the attractive glass transition line [25, 52]. (Some have argued that there is an independent gelation boundary that is described by rigidity percolation [53].) This seems to be corroborated for a number of colloidal systems, including the colloidal clay examined by Ruzicka et al. [54]. The initially prepared suspension is a flowing, simple liquid, with a meniscus that moves under the action of gravity as shown in Fig. 1.3B. The solution then gels (seen through the solid-like meniscus) before ultimately phase separating into dense and dilute regions after several *years*.

While these dramatically slow coarsening dynamics are surely related to the glass transition, it is instructive to consider the underlying driving force and mechanism for passive gel coarsening. The gel coarsening is driven by the need to reduce the excess (interfacial) free energy of the system in order to reach the global free energy minimum associated with bulk macroscopic phase separation $\mathcal{F}^{bulk}$. A number of researchers have found that the coarsening of the network strands of passive gels proceeds *via* single-particle diffusion wherein individual particles on the surface of the gel diffuse to energetically more favorable regions of the network [55, 56]. The underlying contributions to the dynamic free energy barrier in this process consists of both the energetic breaking of the bonds as the particle departs the surface and the entropic barrier associated with the free particle finding an energetically more favorable region. The entropic contribution to this barrier is likely to grow as the gel further coarsens and energetically more favorable regions become scarcer. The surface diffusion mechanism for coarsening can thus be viewed as a series of progressively increasing barriers with each traversed barrier slightly reducing the interfacial area of the material, shown schematically in Fig. 1.3C.

In contrast to the surface diffusion coarsening mechanism, coarsening by bulk diffusion entails the diffusion and coalescence of multiparticle domains, with each of these "coarsening events" resulting in the reduction of substantially more surface area than in the surface diffusion mechanism. However, the free energy barrier for bulk diffusion is also considerably higher as it involves the breaking of several particle bonds in order for multiparticle regions to break away from the network

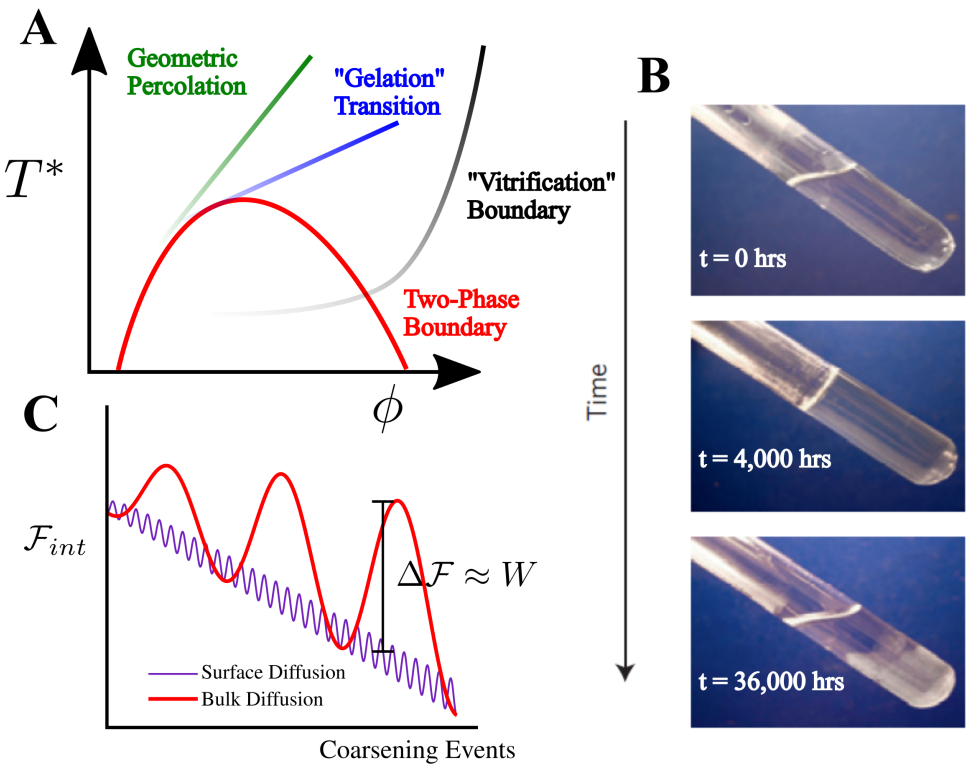

Figure 1.3: (A) Schematic of a dynamic phase diagram of a generic physical gel. For system-specific versions of this phase diagram see, for example, Kumar and Douglas [30] for an associating polymer version and Lu et al. [25] for a colloidal gel version. (B) The phase separation process of a (patchy) attractive colloidal suspension, adapted from Ruzicka et al. [54]. The insets display the waiting time beginning after the sample preparation time. (C) Hypothetical dynamic free energy landscape of a coarsening attractive colloidal suspension.

and diffuse. This primarily energetic barrier will grow as the domains grow thicker (see Fig. 1.3C) and proves too costly for a traditional passive system to overcome with thermal fluctuations alone, precluding coarsening by bulk diffusion. Passive systems with short-ranged attractive interactions cannot spontaneously generate the stress necessary to overcome the mechanical free energy barrier necessary for bulk diffusion [57].

Nonequilibrium protocols provide an opportunity to overcome the naturally occurring kinetic barriers described above. A classic approach is simple thermal annealing; temporally controlling the presence of potential energy barriers by modulating the system temperature can allow for particles to search for stable configurations before the barriers have fully set in. Recently, Swan and co-workers explored temporally varying the interaction potential (e.g., for systems in which the interac-

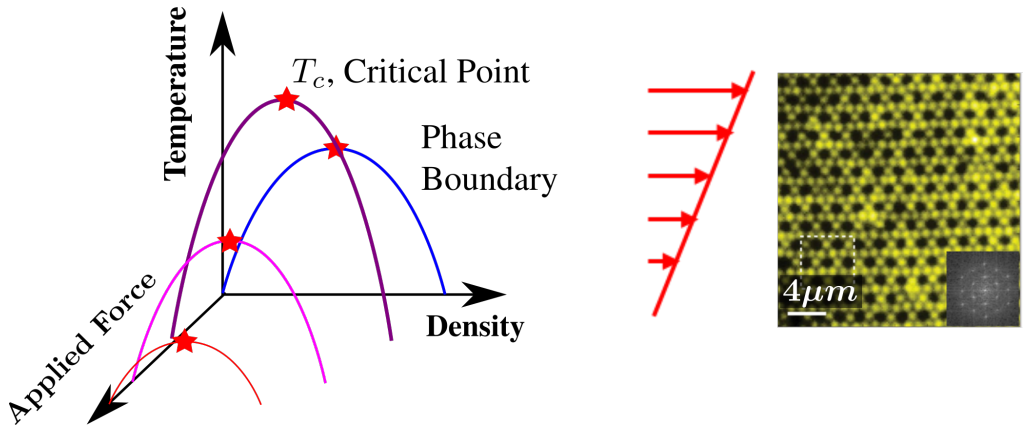

Figure 1.4: (Left) extension of the canonical equilibrium phase diagram to a nonequilibrium dimension. The manner in which the external force is applied can have a profound influence of the system symmetries (see right, adapted from Chen et al. [68]).

tion energy can be modulated with an external field) and found improved colloidal crystallization rates by periodically "toggling" the interactions off and on [58–62]. Applied shear or stress has also been examined as a means by which kinetic barriers can be reduced by allowing dense or yield-stress materials to "fluidize" or yield [63, 64]. Indeed, simulations of colloidal gels in a variety of deformation protocols have revealed an increase in the rate of gel coarsening or phase separated-like states at certain applied rates/stresses [39, 65–67]. In practice, however, while deformation-induced structures may resemble the target structure, the phase diagram is likely fundamentally altered with applied force, shown schematically in see Fig. 1.4. Indeed, at a minimum, deformation protocols naturally break rotational symmetry [68] which could be an essential feature of the target structure (see Fig. 1.4). The development of protocols that truly preserve the underlying (equilibrium) globally stable configuration while providing a viable kinetic pathway to this configuration is a difficult balance and remains an outstanding challenge in colloidal and materials science.

The above examples involve the application of *external* fields to circumvent kinetic barriers. Broadly, these protocols act to inject the necessary free energy (through the system boundary) to either traverse the existing barriers or create entirely new pathways for phase separation. However, these free energy injections need not come from an external source. The recent focus on so-called active particles [69–71] – particles that self-propel or "swim" through the conversion of chemical energy – motivates the idea of doping a material with a small fraction of such particles which

can act as *internal* sources of free energy that can locally drive a material over kinetic hurdles. A complementary mechanical viewpoint is that active particles - just as shear and other deformation protocols – can act as a source of stress by virtue of their unique "swim pressure" [72–74] which, on the colloidal scale, can be the dominant source of stress. Understanding how these active particles alter both the kinetic and "thermodynamic" landscape of the host colloidal material could enable a host of new design strategies in the field of directed colloidal assembly.

1.4 Thesis Outline

In Chapter 2 of this thesis, I present our view on the origin of self-diffusion in associative polymer gels. Scaling arguments lead us to hypothesize that the dominant contribution to diffusion comes from the single-chain motion of a "free chain" (see Fig. 1.2). By experimentally measuring the free chain diffusivity, this hypothesis can be directly tested by computing the estimated number of free chains predicted from *thermodynamic* considerations. I emphasize that the reduction of a many-body dynamical problem to a single-chain thermodynamics is quite convenient and, initially, unexpected. We provide strong evidence that hopping can dominate the effective diffusion of chains in associative networks upon recognizing that there exists a strong (in comparison to the mean-field prediction) entropic penalty for bridge formation imposed by the *local order* in the network structure. This entropic penalty reduces the probability that a chain will have multiple stickers bound to the network, thereby increasing the probability that a chain will hop. For telechelic chains this manifests itself as binding asymmetry, wherein the first association is effectively stronger than the second. We derive a simple thermodynamic model that predicts the fraction of chains that are free to hop as a function of tunable molecular and network properties. A large set of self-diffusivity measurements on a series of model associative polymers finds good agreement with this model. Surprisingly, we find that even upon having as many as five stickers along the backbone of a chain, hopping continues to be a significant contribution to the chain diffusivity.

We move from quiescent gel dynamics to associating polymer gels under strong flow in Chapter 3. Using computer simulations, our study reveals that within a broad range of applied shear rate, the gel separates into two distinct bands with substantially different shear rate and concentration. While this phenomena has been observed in experiments, the molecular mechanism that results in shear-concentration coupling remained unclear. Here, we show that associating polymer gels exhibit a significant microstructural reorganization in response to the elastic stresses due to shear.

Crucially, we find the degree of association only decreases slightly with shear, but the spatial distribution of the network *connectivity* undergoes striking changes: the initial space-spanning network is broken into multiple smaller domains whose size is controlled by the shear rate. The loose connection between these distinct domains significantly enhance the polymer mobility and *osmotic pressure* in the gradient direction. We propose that this effect – which we term "network dilation" – coupled with the inherently large compressibility (low osmotic pressure) of our gels, plays a crucial role in the observed shear-concentration coupling. Crucially, this effect cannot be captured by single-chain models and suggests new physical considerations in the development of future associative polymer rheological constitutive models.

The above results motivated us to consider the use of nonequilibrium means to force oft-undesired colloidal gels towards their stable (minimum free energy) configuration. In Chapter 4, I use computer simulation to demonstrate that nonequilibrium *internal fields* or forces – forces that are generated by driven components within a system – in the form of active particles can precisely modulate the dynamical free energy landscape of a model soft material, a colloidal gel. Embedding a small fraction of active particles within a gel is found to provide a unique pathway for the dynamically frustrated network to circumvent the kinetic barriers associated with reaching a lower free energy state than through thermal fluctuations alone. Moreover, by carefully tuning the active particle properties (the propulsive swim force and persistence length) in comparison to those of the gel, the active particles may induce depletion-like forces between the constituent particles of the gel despite there being *no geometric size asymmetry* between the particles. These resulting forces can rapidly push the system towards disparate regions of phase space. Our findings highlight the potential wide-ranging structural and kinetic control facilitated by varying the dynamical properties of a remarkably small fraction of driven particles embedded in a host material.

Finally, we conclude in Chapter 5 by demonstrating that the stress generated by active particles that was utilized to push colloidal gels to stability, is, in detail, not a true stress. Rather, it is an *equivalent stress*, much like the dynamical pressure used in the context of gravity acting on a fluid and the Maxwell stress tensor used in electrostatics. This finding has important implications in the field of active matter continuum mechanics, which we highlight in resolving the controversy of there being a *negative* surface tension between coexisting active phases despite a seemingly mechanically stable interface. Using the appropriately defined stress

tensor is found to result in a physically plausible surface tension.

References

[1] Bansil, R.; Turner, B. S. Mucin Structure, Aggregation, Physiological Functions and Biomedical Applications. *Curr. Opin. Colloid In.* **2006**, *11*, 164–170.

[2] Bansil, R.; Celli, J. P.; Hardcastle, J. M.; Turner, B. S. The Influence of Mucus Microstructure and Rheology in Helicobacter Pylori Infection. *Front. Immunol.* **2013**, *4*.

[3] Datta, S. S.; Preska Steinberg, A.; Ismagilov, R. F. Polymers in the Gut Compress the Colonic Mucus Hydrogel. *Proc. Natl. Acad. Sci. USA* **2016**, *113*, 7041–7046.

[4] Flemming, H.-C.; Wingender, J. The Biofilm Matrix. *Nat. Rev. Microbiol.* **2010**, *8*, 623.

[5] Rubinstein, M.; Colby, R. *Polymer Physics*; OUP Oxford, 2003.

[6] Wong Po Foo, C. T. S.; Lee, J. S.; Mulyasasmita, W.; Parisi-Amon, A.; Heilshorn, S. C. Two-component Protein-engineered Physical Hydrogels for Cell Encapsulation. *Proc. Natl. Acad. Sci. USA* **2009**, *106*, 22067–22072.

[7] Gaharwar, A. K.; Avery, R. K.; Assmann, A.; Paul, A.; McKinley, G. H.; Khademhosseini, A.; Olsen, B. D. Shear-thinning Nanocomposite Hydrogels for the Treatment of Hemorrhage. *ACS Nano* **2014**, *8*, 9833–9842.

[8] Guo, M.; Pitet, L. M.; Wyss, H. M.; Vos, M.; Dankers, P. Y. W.; Meijer, E. W. Tough Stimuli-responsive Supramolecular Hydrogels with Hydrogen-bonding Network Junctions. *J. Am. Chem. Soc.* **2014**, *136*, 6969–6977.

[9] Cordier, P.; Tournilhac, F.; Soulie-ziakovic, C.; Leibler, L. Self-healing and Thermoreversible Rubber from Supramolecular Assembly. *Nature* **2008**, *451*, 977–980.

[10] Zhou, Z.; Yan, X.; Cook, T. R.; Saha, M. L.; Stang, P. J. Engineering Functionalization in a Supramolecular Polymer: Hierarchical Self-organization of Triply Orthogonal Non-covalent Interactions on a Supramolecular Coordination Complex Platform. *J. Am. Chem. Soc.* **2016**, *138*, 806–809.

[11] Herbst, F.; Seiffert, S.; Binder, W. H. Dynamic Supramolecular Poly(isobutylene)s for Self-healing Materials. *Polym. Chem.* **2012**, *3*, 3084–3092.

[12] Yount, W. C.; Juwarker, H.; Craig, S. L. Orthogonal Control of Dissociation Dynamics Relative to Thermodynamics in a Main-chain Reversible Polymer. *J. Am. Chem. Soc.* **2003**, *125*, 15302–15303.

[13] Yount, W. C.; Loveless, D. M.; Craig, S. L. Small-molecule Dynamics and Mechanisms Underlying the Macroscopic Mechanical Properties of Coordinatively Cross-linked Polymer Networks. *J. Am. Chem. Soc.* **2005**, *127*, 14488–14496.

[14] Xu, D.; Craig, S. L. Scaling Laws in Supramolecular Polymer Networks. *Macromolecules* **2011**, *44*, 5465–5472.

[15] Grindy, S. C.; Learsch, R.; Mozhdehi, D.; Cheng, J.; Barrett, D. G.; Guan, Z.; Messersmith, P. B.; Holten-andersen, N. Control of Hierarchical Polymer Mechanics with Bioinspired Metal-coordination Dynamics. *Nat. Mater.* **2015**, *14*, 1210–1216.

[16] Holten-Andersen, N.; Harrington, M. J.; Birkedal, H.; Lee, B. P.; Messersmith, P. B.; Lee, K. Y. C.; Waite, J. H. PH-induced Metal-ligand Cross-links Inspired by Mussel Yield Self-healing Polymer Networks with Near-covalent Elastic Moduli. *Proc. Natl. Acad. Sci. USA* **2011**, *108*, 2651–2655.

[17] Tang, S.; Habicht, A.; Li, S.; Seiffert, S.; Olsen, B. D. Self-diffusion of Associating Star-shaped Polymers. *Macromolecules* **2016**, *49*, 5599–5608.

[18] Annable, T.; Buscall, R.; Ettelaie, R.; Whittlestone, D. The Rheology of Solutions of Associating Polymers: Comparison of Experimental Behavior with Transient Network Theory. *J. Rheol.* **1993**, *37*, 695.

[19] Petka, W. A.; Harden, J. L.; McGrath, K. P.; Wirtz, D.; Tirrell, D. A. Reversible Hydrogels from Self-assembling Artificial Proteins. *Science* **1998**, *281*, 389–392.

[20] Tang, S.; Wang, M.; Olsen, B. D. Anomalous Self-diffusion and Sticky Rouse Dynamics in Associative Protein Hydrogels. *J. Am. Chem. Soc.* **2015**, *137*, 3946–3957.

[21] Olsen, B. D.; Kornfield, J. A.; Tirrell, D. A. Yielding Behavior in Injectable Hydrogels from Telechelic Proteins. *Macromolecules* **2010**, *43*, 90949099.

[22] Hsiao, L. C.; Newman, R. S.; Glotzer, S. C.; Solomon, M. J. Role of Isostaticity and Load-bearing Microstructure in the Elasticity of Yielded Colloidal Gels. *Proc. Natl. Acad. Sci. USA* **2012**, *109*, 16029–16034.

[23] Asakura, S.; Oosawa, F. On Interaction between Two Bodies Immersed in a Solution of Macromolecules. *J. Chem. Phys.* **1954**, *22*, 1255–1256.

[24] Asakura, S.; Oosawa, F. Interaction between Particles Suspended in Solutions of Macromolecules. *J. Polym. Sci.* **1958**, *33*, 183–192.

[25] Lu, P. J.; Zaccarelli, E.; Ciulla, F.; Schofield, A. B.; Sciortino, F.; Weitz, D. A. Gelation of Particles with Short-range Attraction. *Nature* **2008**, *453*, 499.

[26] Baxandall, L. G. Dynamics of Reversibly Cross-linked Chains. *Macromolecules* **1989**, *22*, 1982–1988.

[27] Semenov, A. N.; Nyrkova, I. A.; Cates, M. E. Phase Equilibria in Solutions of Associating Telechelic Polymers - Rings vs Reversible Network. *Macromolecules* **1995**, *28*, 7879–7885.

[28] Semenov, A. N.; Rubinstein, M. Thermoreversible Gelation in Solutions of Associative Polymers. 1. Statics. *Macromolecules* **1998**, *31*, 1373–1385.

[29] Rubinstein, M.; Semenov, A. N. Thermoreversible Gelation in Solutions of Associating Polymers. 2. Linear Dynamics. *Macromolecules* **1998**, *31*, 1386–1397.

[30] Kumar, S. K.; Douglas, J. F. Gelation in Physically Associating Polymer Solutions. *Phys. Rev. Lett.* **2001**, *87*, 188301.

[31] Green, M. S.; Tobolsky, A. V. A New Approach to the Theory of Relaxing Polymeric Media. *J. Chem. Phys.* **1946**, *14*, 80–92.

[32] Ferry, J. D. *Viscoelastic Properties of Polymers*; Wiley, New York, 1980.

[33] Tanaka, F.; Edwards, S. F. Viscoelastic Properties of Physically Cross-linked Networks - Transient Network Theory. *Macromolecules* **1992**, *25*, 1516–1523.

[34] Tripathi, A.; Tam, K. C.; McKinley, G. H. Rheology and Dynamics of Associative Polymers in Shear and Extension: Theory and Experiments. *Macromolecules* **2006**, *39*, 1981–1999.

[35] Sing, M. K.; Wang, Z.-g.; McKinley, G. H.; Olsen, B. D. Chain Configuration and Rate-dependent Mechanical Properties in Transient Networks. *Soft Matter* **2015**, *11*, 2085–2096.

[36] Sprakel, J.; Spruijt, E.; Cohen Stuart, M. A.; Besseling, N. A. M.; Lettinga, M. P.; Van Der Gucht, J. Shear Banding and Rheochaos in Associative Polymer Networks. *Soft Matter* **2008**, *4*, 1696.

[37] Sprakel, J.; Spruijt, E.; Van Der Gucht, J.; Padding, J. T.; Briels, W. J. Failure-mode Transition in Transient Polymer Networks with Particle-based Simulations. *Soft Matter* **2009**, *5*, 4748.

[38] Castillo-Tejas, J.; Carro, S.; Manero, O. Shear Banding in Telechelic Associative Polymers by Molecular Dynamics. *ACS Macro Lett.* **2017**, *6*, 190–193.

[39] Colombo, J.; Del Gado, E. Stress Localization, Stiffening, and Yielding in a Model Colloidal Gel. *J. Rheol.* **2014**, *58*, 1089–1116.

[40] Dhont, J. K. G.; Briels, W. J. Gradient and Vorticity Banding. *Rheol. Acta* **2008**, *47*, 257–281.

[41] Fielding, S. M. Shear Banding in Soft Glassy Materials. *Rep. Prog. Phys.* **2014**, *77*, 102601.

[42] Nozières, P.; Quemada, D. A Possible Instability Mechanism for Plug Formation in a Sheared Suspension Flow. *Europhys. Lett.* **1986**, *2*, 129–135.

[43] Schmitt, V.; Marques, C. M.; Lequeux, F. Shear-induced Phase Separation of Complex Fluids: The Role of Flow-concentration Coupling. *Phys. Rev. E* **1995**, *52*, 4009–4015.

[44] Helfand, E.; Fredrickson, G. Large Fluctuations in Polymer Solutions under Shear. *Phys. Rev. Lett.* **1989**, *62*, 2468–2471.

[45] Wu, X.-l.; Pine, D. J.; Dixon, P. K. Enhanced Concentration Fluctuations in Polymer Solutions under Shear Flow. *Phys. Rev. Lett.* **1991**, *66*, 2408–2411.

[46] Ramirez, J.; Dursch, T. J.; Olsen, B. D. A Molecular Explanation for Anomalous Diffusion in Supramolecular Polymer Networks. *Macromolecules* **2018**, *51*, 2517–2525.

[47] Lodge, T. P.; Rotstein, N. A.; Prager, S. *Advances in Chemical Physics*; John Wiley & Sons, Ltd, 2007; pp 1–132.

[48] Lodge, T. P. Reconciliation of the Molecular Weight Dependence of Diffusion and Viscosity in Entangled Polymers. *Phys. Rev. Lett.* **1999**, *83*, 3218–3221.

[49] McLeish, T. C. B. Tube Theory of Entangled Polymer Dynamics. *Adv. Phys.* **2002**, *51*, 1379–1527.

[50] Doi, M.; Edwards, S. F. *The Theory of Polymer Dynamics*; Oxford University Press, 1986.

[51] Rapp, P. B.; Omar, A. K.; Shen, J. J.; Buck, M. E.; Wang, Z.-g.; Tirrell, D. A. Analysis and Control of Chain Mobility in Protein Hydrogels. *J. Am. Chem. Soc.* **2017**, *139*, 3796–3804.

[52] Zaccarelli, E.; Lu, P. J.; Ciulla, F.; Weitz, D. A.; Sciortino, F. Gelation As Arrested Phase Separation in Short-ranged Attractive Colloid-polymer Mixtures. *J. Phys. Condens. Matter* **2008**, *20*, 494242.

[53] Valadez-Pérez, N. E.; Liu, Y.; Eberle, A. P. R.; Wagner, N. J.; Castañeda Priego, R. Dynamical Arrest in Adhesive Hard-sphere Dispersions Driven by Rigidity Percolation. *Phys. Rev. E* **2013**, *88*, 060302.

[54] Ruzicka, B.; Zaccarelli, E.; Zulian, L.; Angelini, R.; Sztucki, M.; Moussaïd, A.; Narayanan, T.; Sciortino, F. Observation of Empty Liquids and Equilibrium Gels in a Colloidal Clay. *Nat. Mater.* **2010**, *10*, 56.

[55] Zia, R. N.; Landrum, B. J.; Russel, W. B. A Micro-mechanical Study of Coarsening and Rheology of Colloidal Gels: Cage Building, Cage Hopping, and Smoluchowski's Ratchet. *J. Rheol.* **2014**, *58*, 1121–1157.

[56] Van Doorn, J. M.; Bronkhorst, J.; Higler, R.; Van De Laar, T.; Sprakel, J. Linking Particle Dynamics to Local Connectivity in Colloidal Gels. *Phys. Rev. Lett.* **2017**, *118*, 188001.

[57] Tanaka, H.; Araki, T. Spontaneous Coarsening of a Colloidal Network Driven by Self-generated Mechanical Stress. *EPL* **2007**, *79*, 58003.

[58] Swan, J. W.; Vasquez, P. A.; Whitson, P. A.; Fincke, E. M.; Wakata, K.; Magnus, S. H.; Winne, F. D.; Barratt, M. R.; Agui, J. H.; Green, R. D.; Hall, N. R.; Bohman, D. Y.; Bunnell, C. T.; Gast, A. P.; Furst, E. M. Multi-scale Kinetics of a Field-directed Colloidal Phase Transition. *Proc. Natl. Acad. Sci. USA* **2012**, *109*, 16023–16028.

[59] Swan, J. W.; Bauer, J. L.; Liu, Y.; Furst, E. M. Directed Colloidal Self-assembly in Toggled Magnetic Fields. *Soft Matter* **2014**, *10*, 1102–1109.

[60] Risbud, S. R.; Swan, J. W. Dynamic Self-assembly of Colloids through Periodic Variation of Inter-particle Potentials. *Soft Matter* **2015**, *11*, 3232–3240.

[61] Sherman, Z. M.; Swan, J. W. Dynamic, Directed Self-assembly of Nanoparticles *via* Toggled Interactions. *ACS Nano* **2016**, *10*, 5260–5271.

[62] Sherman, Z. M.; Rosenthal, H.; Swan, J. W. Phase Separation Kinetics of Dynamically Self-assembling Nanoparticles with Toggled Interactions. *Langmuir* **2018**, *34*, 1029–1041.

[63] Liu, A. J.; Nagel, S. R. Jamming Is Not Just Cool Any More. *Nature* **1998**, *396*, 21.

[64] Trappe, V.; Prasad, V.; Cipelletti, L.; Segre, P. N.; Weitz, D. A. Jamming Phase Diagram for Attractive Particles. *Nature* **2001**, *411*, 772.

[65] Koumakis, N.; Moghimi, E.; Besseling, R.; Poon, W. C. K.; Brady, J. F.; Petekidis, G. Tuning Colloidal Gels by Shear. *Soft Matter* **2015**, *11*, 4640–4648.

[66] Landrum, b. J.; Russel, w. B.; Zia, r. N. Delayed Yield in Colloidal Gels: Creep, Flow, and Re-entrant Solid Regimes. *J. Rheol.* **2016**, *60*, 783–807.

[67] Johnson, L. C.; Landrum, B. J.; Zia, R. N. Yield of Reversible Colloidal Gels during Flow Start-up: Release from Kinetic Arrest. *Soft Matter* **2018**, *14*, 5048–5068.

[68] Chen, Q.; Bae, S. C.; Granick, S. Directed Self-assembly of a Colloidal Kagome Lattice. *Nature* **2011**, *469*, 381.

[69] Bechinger, C.; Di Leonardo, R.; Löwen, H.; Reichhardt, C.; Volpe, G.; Volpe, G. Active Particles in Complex and Crowded Environments. *Rev. Mod. Phys.* **2016**, *88*, 045006.

[70] Takatori, S. C.; Brady, J. F. Forces, Stresses and the (thermo?) Dynamics of Active Matter. *Curr. Opin. Colloid Interface Sci.* **2016**, *21*, 24–33.

[71] Mallory, S. A.; Valeriani, C.; Cacciuto, A. An Active Approach to Colloidal Self-assembly. *Annu. Rev. Phys. Chem.* **2018**, *69*, 59–79.

[72] Takatori, S. C.; Yan, W.; Brady, J. F. Swim Pressure: Stress Generation in Active Matter. *Phys. Rev. Lett.* **2014**, *113*, 028103.

[73] Fily, Y.; Henkes, S.; Marchetti, M. C. Freezing and Phase Separation of Self-propelled Disks. *Soft Matter* **2014**, *10*, 2132–2140.

[74] Solon, A. P.; Stenhammar, J.; Wittkowski, R.; Kardar, M.; Kafri, Y.; Cates, M. E.; Tailleur, J. Pressure and Phase Equilibria in Interacting Active Brownian Spheres. *Phys. Rev. Lett.* **2015**, *114*, 198301.

Chapter 2

DYNAMICS OF ASSOCIATIVE POLYMERS: THEORY AND EXPERIMENT

Networks assembled by reversible association of telechelic polymers constitute a common class of soft materials. Various mechanisms of chain migration in associative networks have been proposed, yet there remains little quantitative experimental data to discriminate among them. Proposed mechanisms for chain migration include multichain aggregate diffusion as well as single-chain mechanisms such as "walking" and "hopping", wherein diffusion is achieved by either partial ("walking") or complete ("hopping") disengagement of the associated chain segments. Here we provide evidence that hopping can dominate the effective diffusion of chains in associative networks due to a strong entropic penalty for bridge formation imposed by local network structure; chains become conformationally restricted upon association with two or more spatially separated binding sites. This restriction decreases the effective binding strength of chains with multiple associative domains, thereby increasing the probability that a chain will hop. For telechelic chains this manifests as binding asymmetry, wherein the first association is effectively stronger than the second. We derive a simple thermodynamic model that predicts the fraction of chains that are free to hop as a function of tunable molecular and network properties. A large set of self-diffusivity measurements on a series of model associative polymers finds good agreement with this model.

This chapter includes content from our previously published article:

Rapp*, P. B.; Omar*, A. K.; Silverman, B. R.; Wang, Z.-G.; Tirrell, D. A. Mechanisms of Diffusion in Associative Polymer Networks: Evidence for Chain Hopping. *J. Am. Chem. Soc.* **2018**, *140*, 14185–14194. DOI:10.1021/jacs.8b07908

2.1 Introduction

Polymer chains can associate through non-covalent interactions (e.g., by hydrogen bonding [1–4], metal-ligand coordination [3, 5–10] or hydrophobic forces [1, 11–14]) to form reversible networks. Within such networks, clusters of associative domains serve as transient junctions [15]. The dynamic nature of the junctions permits diffusive transport of chains throughout the network and facilitates spontaneous reorganization or "healing" of the network in response to mechanical damage. Reversible polymer networks have been proposed for application in tissue engineering, [16, 17] controlled drug delivery [18] and organic electronics and battery technology [19, 20]. Understanding the factors that control polymer diffusion in reversible networks is important for optimizing material performance in these settings and for elucidating the principles that govern macromolecular transport in biological systems. For example, eukaryotic cells utilize networks of non-covalent interactions to regulate protein transport into the nucleus [21, 22] and to control the localization of growth factors and cytokines in the extracellular matrix [23].

Previous experimental [5–7, 11, 13, 24–26] and theoretical [11, 15, 27–30] investigations of associative polymer networks have sought to relate their bulk physical properties (viscosity, elastic modulus, relaxation rate) to the underlying structural and dynamical configurations of the constituent chains. When the chains are not significantly interpenetrated (i.e., in the unentangled regime), network stress relaxation is typically attributed to chain disengagement from the junctions. Although this simple single-chain picture serves as the foundation for several successful rheological models [11, 30, 31], the physical basis for self-diffusion in associative networks is decidedly less clear. Despite nearly 30 years of conceptual development [27, 32], no single mechanistic picture of how the constituent chains move has found quantitative experimental validation. This stands in contrast to our more complete understanding of self-diffusion in unassociative polymer solutions, for which mechanisms such as reptation find strong experimental support [33–36].

For diffusion in the unentangled regime, two complementary mechanistic schemes have been predominantly invoked. If a chain disengages from the network completely such that it temporarily has no bound segments, it may diffuse freely over relatively large distances before rebinding (we refer to this process as "hopping", Fig. 2.1. Alternatively, center-of-mass translation of the chain may be achieved by stepwise dissociation and reassociation of individual chain segments (in a process akin to "walking"), without the chain ever becoming completely untethered

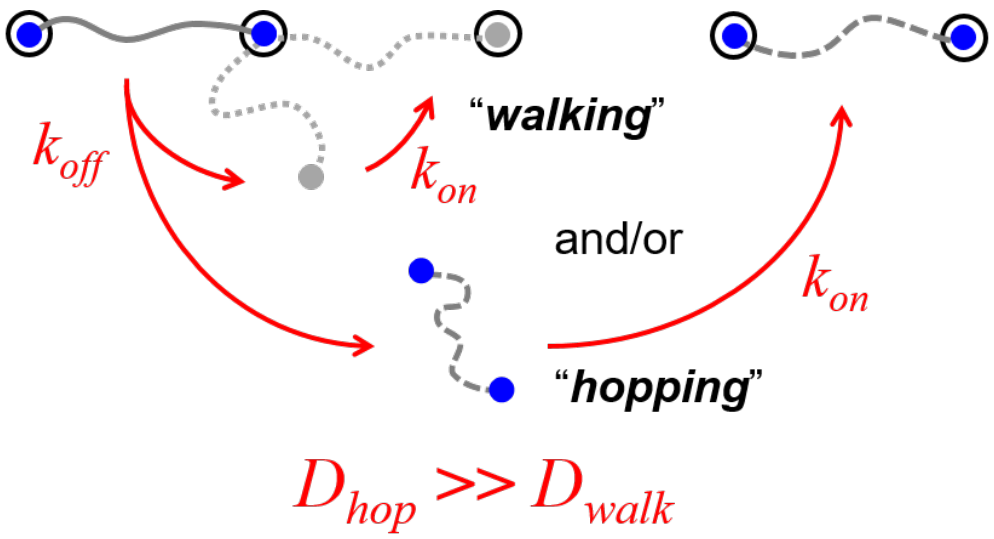

Figure 2.1: Diffusive migration of associative polymer chains through reversible networks can occur via partial or complete disengagement of the associative segments, i.e., by "walking" or "hopping". Here we provide evidence that $D_{hop} \gg D_{walk}$ in model networks.

from the network. Baxandall considered the diffusion of single multisticker chains reversibly interacting with a mean-field (structureless) network, predicting an ensemble of walking modes [27]. The walking diffusivity was proportional to the sticker dissociation rate and inversely proportional to the number of stickers (effectively Rouse-like). Rubinstein and Semenov subsequently proposed a "sticky Rouse" picture which postulated that the bound chains are carried along in large multichain clusters [15]. Recent simulations [37] indicate that such cluster diffusion may become particularly important when the network is under steady shear, but its role in quiescent-state relaxation remains unclear. Both theoretical treatments disregard hopping, i.e., the fraction of free chains is assumed to be negligible. Olsen and co-workers invoked a form of bound diffusivity along with chain hopping to rationalize anomalous "super-diffusive" behavior within associative networks, wherein the effective diffusion coefficient appears to increase with time over a finite length-scale [10, 13]. Recently they proposed transient escape from network junctions, corresponding to a transition between walking and hopping, as the molecular origin of this intriguing phenomenon [32].

The present study is motivated by our earlier observation that the sequential binding of the two ends of a telechelic polymer to a reversible network appears "asymmetric", i.e., the first association is stronger than the second, despite identical molecular properties of the terminal associative domains [25]. We now demonstrate that

marked differences between the intrinsic and effective binding strengths of associative domains on multisticker chains are a general feature of unentangled reversible networks. Whereas the intrinsic binding strength of a sticker is set by its molecular properties, the effective binding strength of the sticker is sensitive to the local structure of the network and is attenuated by the presence of other concurrently bound stickers on the same chain. The origin of this effect is a strong entropic penalty imposed on chain entry into conformationally restricted states during sequential binding events. A given chain must sacrifice rich sets of conformations in order to bind multiple junctions simultaneously. This constraint significantly amplifies the fraction of free (hopping) chains and diminishes as the ratio of the chain size to the network size increases.

We first incorporate these ideas into a simple thermodynamic model that predicts the fraction of chains that are free to hop as a function of tunable network and molecular properties. We then test our model predictions with a large set of self-diffusivity measurements obtained in telechelic associative protein hydrogels and find consistent agreement with the model. Surprisingly, hopping is the dominant mode of diffusion despite the large enthalpic penalty for dissociation. Furthermore, hopping remains a major diffusion mechanism for multisticker chains with as many as five stickers. These results provide new insight into the chain transport dynamics of an important class of polymeric materials.

2.2 Theory

Network Model

We consider associative networks in the dynamic regime where chain dissociation is much slower than the characteristic Rouse relaxation of the constituent chains (typical for most experimental associative networks). We model the network as an ensemble of multisticker chains having S total associative domains ("stickers") that are equally spaced along the chain, with stickers capping the ends of the chain. A chain can partition into $i \leq S$ bound states, where $i = 0, 1, 2...S$ represents the total number of stickers bound to the network. One can define corresponding equilibrium constants K_i (where K_i is the binding constant characterizing the transition from $i-1$ to i bound stickers) that describe how the chain distributes among these various states. For example, telechelic chains have two terminal stickers ($S = 2$) and can be partitioned into three sequential states (Fig. 2.2A). In the free state f, neither chain end is bound to the network ($i = 0$). By reversible association with the network, the chain may transition into either the dangle state d (one end bound, $i = 1$) or

the bound state b (both ends bound, $i = 2$). Two species compose the bound state of telechelic chains: bridges (B), where the chain ends are bound to two different junctions and loops (L), where both ends converge on the same junction. Conversion among these three states is controlled by two equilibrium constants $K_1 = [d]/[f]$ and $K_2 = [B]/[d] + [L]/[d] = K_B + K_L$.

Previous approaches to modeling reversible networks consider chains interacting with a mean-field background and neglect spatial correlations between junctions (i.e., they envision a structureless network) [15, 27, 32]. Overlooking local network structure in this way fails to capture an essential loss of entropy upon binding. The following theoretical considerations suggest that this entropic penalty attenuates each K_i of a multisticker chain for all but the first association, leading to an effective network binding strength that is much smaller than would be expected from the mean-field approach. For telechelic chains, this manifests as binding asymmetry, with $K_1 > K_2$ arising from conformational restrictions imposed on the bridge state. Simple thermodynamic considerations predict that this difference in binding strengths decreases as the chain size (N) becomes large relative to the characteristic mesh size (M) of the network (Fig. 2.2B). In the limit of $N \gg M$, the chains begin to perceive the network as "mean-field-like" such that $K_1 \approx 4K_2$.

2.3 Statistical Mechanics of Chain Binding

Each equilibrium constant K_i described in the preceding section may be formally defined as the ratio of the number of chain configurations with i bound stickers to the number with $i - 1$ bound stickers, weighted by the binding energy. The equilibrium constants are obtained by equating the chemical potentials of the chains in each state (i.e., $\mu_i = \mu_{i-1}$). Neglecting interchain interactions apart from junction binding, one readily finds:

$$K_i = \frac{Z_i}{Z_{i-1}} \exp(-\beta \Delta E), \tag{2.1}$$

where Z_i represents all possible configurations of a chain with i bound stickers, $\beta = 1/k_B T$ and ΔE is the energy released upon binding of one of the stickers to a network junction. We model individual chains as consisting of N statistical segments each of Kuhn length b_k. We consider probe chains with end-to-end distance $R_{probe} = b_k N^{1/2}$ within a network of characteristic mesh size (inter-junction spacing) $R_{mesh} \sim M^{1/3}$, where M is the number of statistical segments in the chains that compose the network. The latter scaling arises under the condition that as the network chains increase in size, the total concentration of polymer remains fixed

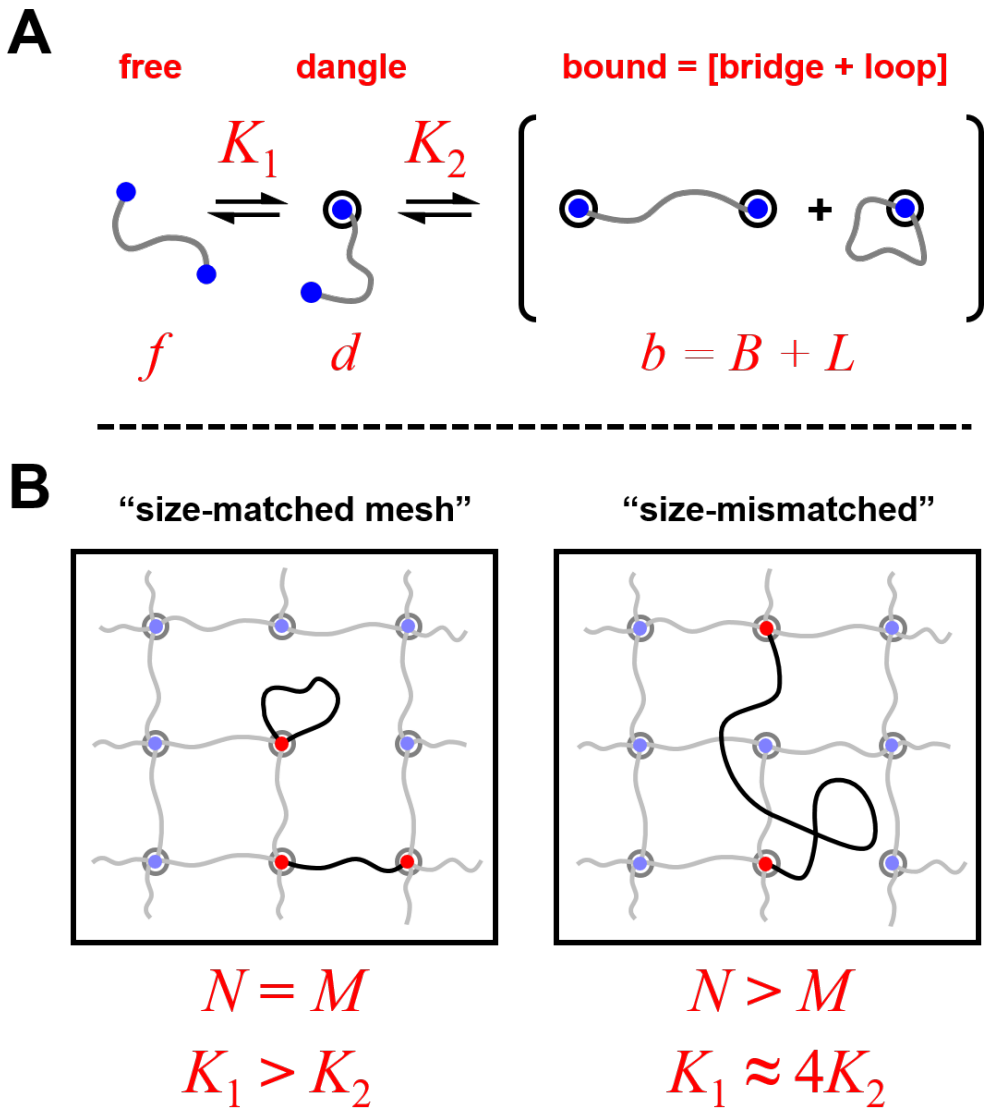

Figure 2.2: Schematic representation of telechelic chain partitioning in reversible networks. (A) Two equilibrium constants K_1 and K_2 control chain partitioning among three sequential states: free (f), dangle (d) and bound (b). The bound state consists of bridges (B) and loops (L). (B) Local network structure affects the binding equilibrium of telechelic chains. When the chain size (N) and mesh size (M) are the same, an entropic penalty for bridge formation manifests as binding asymmetry ($K_1 > K_2$). As the chains become larger than the mesh, the difference in binding strengths decreases to the mean-field limit ($K1 \approx 4K_2$).

such that the junction density linearly decreases with M. For telechelic polymers, the integral $Z_0 \sim \Omega_f(N, b_k) = \int P(\boldsymbol{R}; N, b_k) d\boldsymbol{R}$ counts the number of accessible configurations in the free (unbound, $i = 0$) state to within a constant prefactor. This prefactor is inconsequential, as it may be absorbed into a reference chemical potential [38]. $P(\boldsymbol{R})$ represents the normalized end-to-end vector probability density function of the free probe chains and as such, Z_0 is taken to be unity without loss of generality.

When one end of a telechelic chain attaches to a network junction (in a transition from free to dangle, $i = 1$), the chain energy changes by an amount ΔE. This transition entails a loss of translational entropy, as a dangling chain is restricted to a small fraction ϕ_j (proportional to the junction density) of the total system volume. However, the untethered chain end may still explore the local space around the junction. Additional losses in conformational entropy may therefore be neglected, provided the junction itself is small and the dangling chain does not "feel" the presence of other bound chains ($1 - \phi_j \approx 1$). These considerations suggest $Z_1 \approx 2\phi_j \Omega_j$, where the factor of two arises because a chain can occupy the dangle state by engaging either one of its ends (i.e., there are twice as many configurations of a telechelic chain with one sticker bound as for a "monochelic" chain with its only sticker bound [39]) and these two configurations are degenerate. From eq. (2.1), we obtain $K_1 = 2\phi_j \exp(-\beta \Delta E)$.

The chain faces a new challenge during the second binding event (transition from dangle to bridge, $i = 2$). In order to form a bridge, the untethered chain end must bind to a new junction some (vector) distance $\boldsymbol{R}$ away from the chain end that is already bound. The probability of finding this second junction depends on the local structure of the network. Whereas a dangling chain has no external constraint imposed on its end-to-end distance, bridged chain conformations in which the two chain ends do not overlap with two different junctions cannot exist. Significant conformational entropy may therefore be lost during bridge formation, provided the network junctions tend to be separated by some characteristic distance R_{mesh}. Although gels are isotropic and generally lack long-range order, local order (i.e., spatial correlation between junctions) is expected as a natural consequence of gelation: the network junctions cannot get too close to each other without placing elastic stress on neighboring chains [25].

We formalize this network-imposed entropic constraint by restricting the second end of a bridged chain to a significantly reduced volume fraction $\phi_j g(\boldsymbol{R}; R_{mesh})$. Here

$g(\boldsymbol{R}; R_{mesh})$ represents the normalized junction pair distribution function, which maps the probability of finding a second junction as a function of position along a radial axis originating from the first junction. The entropic penalty for bridge formation at distances $\boldsymbol{R}$ will be large when $g(\boldsymbol{R}) < 1$ for $|\boldsymbol{R}| < R_{mesh}$ such that junctions are locally "depleted" on the length scale of a dangling chain. The penalty becomes even larger when R_{mesh} is larger than the preferred size (equilibrium end-to-end distance) of the free or dangling chain, in which case a bridged chain is also forced to stretch. If the junction spacing is sufficiently large, it may be thermodynamically favorable for a chain to remain in the dangle state or to form a loop. Because the loop state is intramolecular, it is assumed to be independent of local network geometry, similar to the dangle state.

To incorporate these expectations into the network model, we count bound chain configurations as the sum of bridges and loops, with the bridge configurational integral Ω_B weighted by the local junction density. Thus $Z_2 = \phi_j^2\Omega_B + \phi_j\Omega_L$, where $\phi_j^2\Omega_B$ is the conformational entropy of bridged chains and the corresponding configurational integral is $\Omega_B = \int P(\boldsymbol{R})g(\boldsymbol{R})d\boldsymbol{R}$. In analogy to the dangle state, the entropy of loops is $\phi_j\Omega_L$ and we choose to let Ω_L take the same functional form as Ω_f, i.e., $\Omega_L \sim \int P(\boldsymbol{R})d\boldsymbol{R}$. However, we restrict the bounds of this conformational integral to a small distance l approximating the end-to-end distance of looped chains. This integration limit represents a renormalized cubic form of the classical Jacobson-Stockmayer factor, which quantifies the entropic cost of constraining a polymer chain to a cyclic conformation [40–42]. In our case, l can be estimated directly from rheological data (see our treatment of loops below) or treated as an adjustable parameter in order to generate constrained model "fits" to experimental data. From eq. (2.1), $K_2 = [(\phi_j\Omega_B + \Omega_L)/2\Omega_f]\exp(-\beta\Delta E)$.

The preceding theoretical considerations provide the following integral expression for the ratio of K_1 to K_2 for a telechelic polymer:

$$\frac{K_1}{K_2} = \frac{4\Omega_f}{\Omega_B + \Omega_L/\phi_j}. \tag{2.2}$$

The ratio is independent of binding energy. It is possible to neglect loops entirely by setting $\Omega_L = 0$. In this case, the above ratio becomes independent of junction density and is simply:

$$\frac{K_1}{K_2} = \frac{K_1}{K_B} = \frac{4\Omega_f}{\Omega_B} = \frac{4\int P(\boldsymbol{R})d\boldsymbol{R}}{\int P(\boldsymbol{R})g(\boldsymbol{R})d\boldsymbol{R}} \geq 4. \tag{2.3}$$

Taken together, eq. (2.2) and eq. (2.3) distill our key prediction for the reversible binding of telechelic polymers: we expect $K_1 > 4K_2$ in any network with spatially correlated junctions. Although both associative domains have the same intrinsic binding strength (e.g., the enthalpy of association is the same), the effective binding strengths of the domains differ. This discrepancy between K_1 and K_2 is a consequence of different entropic constraints that govern the two binding events. Whereas translational entropy is lost during both associations, additional conformational entropy is lost in the second association due to restrictions on end-to-end distance enforced by the spatial separation of network junctions. In effect, the network binding affinity of a chain end is reduced whenever the other chain end is already bound. This conformational entropic penalty is expected to decrease as a probe chain increases in size relative to the mesh. For an infinitely long telechelic probe in a finite mesh, the effect of local network structure should disappear completely (apart from topological constraints imposed by the network strands). In this case the untethered chain end would behave like a free chain end: it would have a global "view" of the network (it could access all open sites) such that bridge formation would not be constrained by the location of the other end. $K_1 = 4K_2$ is predicted in this mean-field limit due to the degeneracy of the dangle state. We emphasize that our model is not a self-consistent thermodynamic model for establishing the point of network formation [28, 43]. Rather, we presuppose that the conditions are such that a gel is in fact formed, in order to explore the influence of network structure on the state populations of the chains.

Connection to Diffusion Mechanisms

The above thermodynamic model predicts the relative magnitudes of K_1 and K_2 as a function of the size of a probe chain in relation to the mesh size of the network. Under the assumption that $g(\boldsymbol{R})$ is a function of R_{mesh} only, eq. (2.3) comes to depend on a single parameter, the dimensionless probe size $r \equiv R_{probe}/R_{mesh} \sim b_k N^{1/2} M^{-1/3}$. The model can thus be tested by placing increasingly large monodisperse test chains in networks of various sizes and measuring K_1 and K_2. These binding constants together specify the equilibrium fraction of free (i.e., hopping) chains as $[f] = [1 + K_1 + K_1K_2]^{-1} = [1 + K_{eff}^2]^{-1}$, where $K_{eff} = (K_1 + K_1K_2)^{1/2}$ represents the effective binding coefficient for the entire chain. Below we infer experimental K_1 and K_2 values from extensive measurements of polymer self-diffusivities made within telechelic protein hydrogels. The equilibrium constants are obtained under the assumption that hopping represents the only diffusive mode. Interpreting the data

in this way, we find that eq. (2.3) accurately describes the experimental equilibrium constant ratios. This concordance provides indirect evidence for the predominance of hopping in comparison to other diffusive modes (e.g., walking or cluster diffusion) in the networks examined.

Generalization to Chains with Multiple Stickers

The derivation of binding constants for telechelic chains may be generalized to obtain S total equilibrium constants K_i that govern the binding to the network of multisticker chains with $i \leq S$ associative domains bound to the network at any given time. The chain is first decomposed into $S - 1$ flexible "blocks" between adjacent stickers, i of which are bound. The entropy associated with each block is then calculated and Z_i is obtained as the product of the numbers of configurations available to each block. We derive the exact K_i values for the cases of $S = 3$ and $S = 5$ in the Appendix (see the "Generalized Binding Asymmetry for Multisticker Probes" section and Table 2.1). In analogy to telechelic polymers, our key prediction for multisticker chains is that the conformational restrictions enforced by junction separation influence each association, such that $K_i > K_{i+1}$ holds for all $i \leq S - 1$.

Results and Discussion

Network Design and Characterization

We designed a series of reversible telechelic networks to test the predictions of the model just described. Artificial proteins are well suited to exploring the physical properties of reversible networks: they are structurally well-defined, monodisperse and easily varied by changing their DNA coding sequences. We cloned and expressed a family of 21 P(EnP)m-type protein polymers, where P is an associative domain that forms pentameric coiled-coils (network junctions) and En is a flexible elastin-like linker. When swollen in aqueous buffer, PEnP proteins formed transparent hydrogels with classical "Maxwell-type" rheological signatures [44]. We could easily vary the mesh size and terminal modulus of each gel by changing the number of repeats of the elastin midblock ($n = 3 - 24$), without significantly perturbing the network relaxation rate (Table 2.3). The terminal network modulus of each "n-mesh" approximated the molecular weight dependence expected from rubber elasticity theory ($G' \sim M^{\nu}$), with $\nu = -1$ expected for affine networks [45] and $\nu = -0.9 \pm 0.2$ observed experimentally [44].

Measurement of Equilibrium Constants

The equilibrium constants K_1 and K_2 for telechelic polymers in each n-mesh were estimated by measuring the effective diffusivities of size-matched ($N = M$) and mismatched ($N \neq M$) fluorescently labeled test chains ("n-probes", $n = 3 - 48$) having either zero (En*), one (EnP*) or two (PEnP*) terminal coils, where * indicates that the proteins have a C-terminal cysteine for fluorophore conjugation (Fig. 2.3A). The effective diffusivities of the probes were measured by fluorescence recovery after photobleaching (FRAP) [46, 47]. In this technique, a small region of a sample labeled with a dilute fluorescent species is briefly exposed to a high-intensity laser to promote local, irreversible inactivation of the fluorophore. Subsequent recovery of fluorescence in the photo-bleached region ("bleach spot") reports on the mobility of the labeled species. The effective diffusivity D_S of a test chain carrying S associative domains is obtained by fitting the FRAP trace to a renormalized Fickian diffusion model (see Appendix) [25, 46, 47]. The diffusivity can be related to binding equilibrium constants through the equation:

$$\frac{D_0}{D_S} = 1 + K_1 + K_1K_2 + \ldots + \prod_{i=1}^{S} K_i = 1 + \sum_{j=1}^{S}\left(\prod_{i=1}^{j} K_i\right), \tag{2.4}$$

where $D_0 = D_f$ is the effective Fickian diffusivity of the test chain in the free state.

The derivation of eq. (2.4) assumes that reversible binding of the chains is fast relative to the time scale of free diffusion during the FRAP experiment, which we validated previously for PEnP gels [25]. For the experimental regime probed here, we estimate that $k^*_{on}a^2/D_0 \approx 10^2 - 10^3$ for the case when the bleach spot radius $a = 10\mu m$ and k^*_{on} is the (concentration-dependent) pseudo-first-order association rate constant. Equation (2.4) further assumes that network chains have a negligible mobility once bound, such that all chain migration occurs through the hopping mechanism, i.e., single chains must completely disengage from the network (enter the free state) in order to undergo center-of-mass translation. Therefore, if the equilibrium constants inferred from this equation are consistent with our thermodynamic model, hopping is indicated to be the dominant diffusive mode. Inversely, if the correspondence to theory is poor, other diffusive modes must be invoked. Similar logic is readily extended to multisticker chains.

To begin, we obtain D_0 by monitoring the fluorescence recovery rate of an En* test chain that cannot bind the network and is therefore "locked" in the free state. K_1 is then obtained by measuring the mobility D_1 of an EnP* probe and entering the values of D_0 and D_1 into eq. (2.4). Note that the equilibrium constant thus obtained

reflects the association strength of chains with only one sticker (EnP* probes), i.e., $K_1 = \phi_j \exp(-\beta\Delta E)$. Because the dangle state is degenerate for telechelic chains, the equilibrium constant measured for EnP* must be multiplied by two to obtain K_1 for a PEnP* probe. Finally, K_2 for telechelic chains is obtained by measuring D_2 for a PEnP* probe and supplying it into eq. (2.4), together with D_0 and K_1. At each step we allow D_0 to decrease following a default Rouse scaling $D_0 \sim N^{-1}$, to take into account the added friction of the additional P domain. Although the conformational properties of this domain in the unbound state are unknown, adjusting $D_0 \sim N^{\nu}$ using a weaker ($\nu = -0.6$) or stronger ($\nu = -2$) scaling exponent has essentially no effect on the inferred binding constant ratios, i.e., this scaling adjustment is minor. Iterating this procedure for many probe-mesh combinations provides experimental K_1/K_2 ratios as a function of N and M, which are proportional to the molecular weights of the test chain and the network, respectively.

The FRAP method, combined with the total control of chain structure characteristic of protein synthesis, allowed us to tune the properties of the network independent of the embedded fluorescent tracers and provided great flexibility in testing our model predictions. We acquired a total of 298 FRAP traces on 15 different probes in four different meshes (60 unique probe-mesh combinations) in order to explore a wide range of different probe-to-mesh ratios ($r = R_{probe}/R_{mesh}$). Since the shape and intensity of the bleach spot were found to be moderately sensitive to the structure of the probe, we acquired an additional 173 control FRAP traces on size-matched En* probes in each of the four meshes. Using a generalized Gaussian bleach spot fit-and-track algorithm, we found the measured diffusivity to be insensitive to variation in the bleach spot profile over a wide range of bleach efficiencies.

Power-law Fits to Diffusivity Data

Our model predicts that, as probe chains increase in size above the mesh size of the network, K_1/K_2 will decrease monotonically. Coarse power-law fits to the diffusivity dataset provide a qualitative test of this prediction. Polymer diffusivities typically exhibit power-law scaling with molecular weight, i.e., $D \sim N^{\alpha}$ where the molecular weight exponent α is negative (e.g., $\alpha = -1$ in the Rouse model) [48]. By measuring these exponents, we can infer additional molecular weight exponents β for each equilibrium constant $K_i \sim N^{\beta}$ from a scaling analysis of eq. (2.4). In the 6-mesh, $\alpha_0 = -1.5$, $\alpha_1 = -0.9$ and $\alpha_2 = -1.5$ for D_0, D_1 and D_2, respectively, (Fig. 2.3B). From eq. (2.4) we infer $\beta_1 = \alpha_0 - \alpha_1 = -0.6$ for K_1 as well as $\beta_2 = \alpha_1 - \alpha_2 = 0.6$ for K_2. Critically, the molecular weight exponent for K_2 is

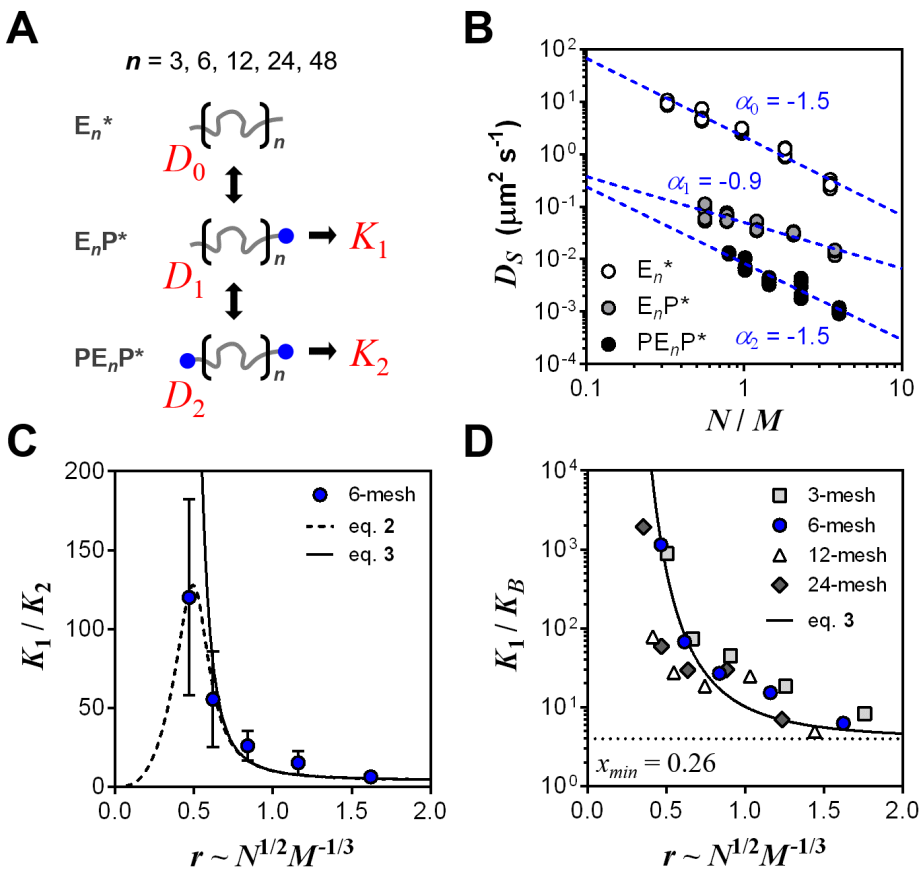

Figure 2.3: Experimental binding constant ratios inferred from diffusion measurements: correspondence to theory supports chain hopping. (A) Elastin-like probes with different lengths and numbers of stickers were placed in size-matched ($N = M$) and mismatched ($N \neq M$) "n-mesh" PEnP networks. Equilibrium constants were inferred from FRAP diffusivity measurements via eq. (2.4), i.e., assuming exclusive hopping. Estimating a single K_1/K_2 ratio requires independent diffusivity measurements from three different probe types having zero (En*), one (EnP*) or two (PEnP*) stickers. (B) Representative diffusivities in a 6-mesh (80 total measurements, ≥ 4 per probe type). Approximate molecular weight exponents for each probe type were estimated from coarse power-law fits (see discussion in main text). (C) The experimental K_1/K_2 data (mean ± std. dev.) in the 6-mesh reveal binding asymmetry for telechelic chains. The data are plotted against the dimensionless probe size $r \equiv R_{probe}/R_{mesh} \sim b_k N^{1/2} M^{-1/3}$. The "loop-free" prediction from eq. (2.3) and the single-parameter fit of eq. (2.2) with $x_{min} = 0.26$ are shown; $x_{min} = l_{min}/c$ is the best-fit dimensionless integration limit for the looping configurational Ω_L (see discussion in main text). (D) Loop subtraction with $x_{min} = 0.26$ permits comparison of the K_1/K_2 data from each mesh to eq. (2.3) (shown are mean K_1/K_B ratios deduced from 298 total measurements, ≥ 4 per probe type). Error bars in panel D are omitted for clarity, but are analogous in size to those in panel C. The dotted line represents the mean-field limit $K_1/K_B = 4$.

positive, implying increasing association strength of the second chain end as the test chain becomes longer. Moreover, the exponent corresponding to the K_1/K_2 ratio, $\beta_1 - \beta_2 = -1.2$, is strongly negative, consistent with weakening of the entropic constraint for bridge entry as the chain length grows. These results are in qualitative agreement with our model.

That the free-chain diffusivity exhibits a molecular weight exponent that is stronger than Rouse-like ($\alpha_0 = -1.5$ for D_0) may indicate crossover between different regimes (i.e., Rouse to reptation-like [49]) as the probe chains become large relative to the mesh size; its precise origin requires further investigation. We attribute the negative value of β_1 to excluded volume effects (e.g., end group association on the test chain starts to become sterically hindered by the large pervaded volume of the chain itself), which are not included in our model. Presumably such effects would hinder both associations to a similar extent, in which case they should minimally affect the experimental K_1/K_2 ratio. Note that the binding constants are not expected to have formal power-law dependencies on N, so there is no rigorous basis to expect the molecular weight exponents β to hold generally.

2.4 Quantitative Comparison to Theory

A quantitative comparison of the experimental equilibrium constant ratios to the thermodynamic model (eqs. (2.2) and (2.3)) requires estimates of the mesh size R_{mesh} and the probe size R_{probe}. Reasonable estimates for these key parameters are readily obtained (see Appendix) [50–53]. The estimated probe sizes range from 6.1 to 21.4 nm, whereas the smallest (3-mesh) and largest (24-mesh) networks have mesh sizes of 12.2 nm and 17.3 nm, respectively, (Table 2.3 and Table 2.2). Since we examine chain lengths below the thermal blob size (such that excluded volume interactions and correlations can be largely neglected), we evaluate the configurational integrals using $P(\boldsymbol{R}; N, b_k) = (3/2\pi N b_k^2)^{3/2} \exp(-3\boldsymbol{R}^2/2Nb_k^2)$ [45], the probability density function for the end-to-end distance of an ideal (Gaussian) chain. For simplicity, we approximate $g(\boldsymbol{R}; R_{mesh})$ as a Heaviside step function activated at R_{mesh}. Except Ω_L, all configurational integrals are taken over the range of possible sizes of the chain, which for a Gaussian chain is the interval $[0, \infty]$.

Figure 2.3C plots K_1/K_2 predicted by eq. (2.3) as function of the reduced (dimensionless) probe size r, together with experimental K_1/K_2 data obtained from FRAP experiments in the 6-mesh. The experimental K_1/K_2 ratio decays monotonically as the probe size increases, in good agreement with the prediction from eq. (2.3) (no

loops). This correspondence is obtained without any externally fit model parameters or data transformation, beyond obtaining reasonable estimates for chain and network dimensions. Note that the difference in binding constants is significant even when the probe chains have the same dimensions as the mesh ($K_1/K_2 \approx 20$ is observed for $r = 1$), pointing to the critical role played by local junction order as opposed to chain stretching. The data thus support a central hypothesis of the thermodynamic model: chains in the bridge state are conformationally constrained beyond the mean-field prediction and the conformational constraint reduces the effective association strength of the chains. The entropic penalty for bridge formation increases as the chains decrease in size within a network of fixed dimensions.

This finding has important implications for the dominant mechanism of chain diffusion. Reducing the effective association strength of the chains increases the fraction of free (dissociated) chains. Moreover, using eq. (2.4) to infer experimental binding constants implicitly assumes negligible translational motion in the bound state (i.e., all fluorescence recovery is attributed to the movement of free chains). The fact that this inference provides binding constant ratios consistent with eq. (2.3) supports the assumption that at equilibrium, effective diffusion in PEnP networks is dominated by hopping. For this assumption to be invalidated, an alternative diffusive mode having the same functional dependence on network structure as the equilibrium fraction of free chains would need to be identified. Other diffusive modes such as walking [27] or multichain diffusion [15] may still be important for related dynamic network phenomenon (e.g., stress relaxation).

Inclusion of Loops

Dimensional analysis of eq. (2.3) reveals that, when loops are neglected and $g(\boldsymbol{R})$ is the unit step function, K_1/K_2 is determined solely by the dimensionless probe size r. In eq. (2.2), however, loop inclusion introduces a concentration dependence via the term Ω_L/ϕ_j. Careful analysis of this concentration dependence further substantiates the thermodynamic model. The concentration may be expressed as $\phi_j = (2c/R_{mesh})^3$, where $c = 1.89$ nm represents the "cluster size" or characteristic dimension of a network junction (see Appendix for the numerical determination of this parameter). Since Ω_L is integrated over the interval $[0, l]$, it is convenient to define a second dimensionless parameter $x \equiv l/c$ and integrate over the new interval $[0, x]$. In this case the ratio Ω_L/ϕ_j $(l/c)^3$ is approximately independent of c for fixed values of x (Fig. 2.7). With this construction, eq. (2.2) depends solely on r and x and accounting for loops amounts to obtaining a reasonable estimate for the

dimensionless integration limit x.

Because Ω_L and Ω_B are theoretically related to the gel modulus (to first order, only bridged chains are elastically effective), it is possible to estimate x based on rheological data (eq. (2.13) and Fig. 2.8). This provides $x = x_{rheo} = 0.41 \pm 0.28$ across the four different meshes examined here (Table 2.3). In practice, eq. (2.2) is quite sensitive to the value of x due to the cubic nature of the volume integral (i.e., $\Omega_L/\phi_j\ x^3$). One can also obtain $x = x_{min}$ by systematically varying x in order to minimize residuals between model-constrained "fits" of eq. (2.2) to the experimental K_1/K_2 values (Figs. 2.8 and 2.9)). Figure 2.3C presents a single-parameter fit of eq. (2.2) to the 6-mesh data with $x_{min} = 0.26$ ($x_{min} = 0.32 \pm 0.09$ is obtained from collating the estimates across each of the four meshes, Table 2.3). The fit captures an observed softening of the experimental rise in K_1/K_2 at low r (relative to the "loop-free" prediction of eq. (2.3)), an effect attributable to the increased prevalence of loops. The fits are qualitatively better in the smaller (3- and 6-mesh) gels, which we attribute to decreased local order in the more open (12- and 24-mesh) gels, for which K_1/K_2 also tends to be lower (Fig. 2.9).

Although the data in each mesh were acquired at fixed mass concentrations ($\rho = 100$ mg/mL), the junction density ϕ_j is different in each mesh because of differences in midblock length. Accounting for loops provides a means to compare the measurements of K_1/K_2 from each mesh. This comparison is obtained by subtracting the concentration-dependent terms (i.e., Ω_L/ϕ_j) from the experimental K_1/K_2 ratios to obtain the "loop-free" ratio K_1/K_B. Combining eq. (2.2) and eq. (2.3) reveals that $K_1/K_B = [K_2/K_1 - \Omega_L/4\phi_j]^{-1}$. Using $x_{min} = 0.26$ to perform the subtraction leads to a satisfying collapse of the entire dataset (298 total measurements) onto the universal "loop-free" curve of eq. (2.3) (Fig. 2.3D). The K_1/K_B values obtained in this way vary over a remarkable 300-fold range, exceeding 103 for $r = 0.36$, obtained with the (smallest) 3-probe in the (largest) 24-mesh. Moreover, the data appear to approach the predicted mean-field asymptote: $K_1/K_B = 4.9 - 8.3$ is obtained from the largest probes in each mesh over the domain $r = 1.2 - 1.8$. The coherence of this large dataset with model predictions further reinforces the validity of the hopping inference.

Concentration Dependence

In order to test the concentration dependence of eq. (2.2) more directly, we acquired an additional 54 FRAP traces in size-matched ($N = M$) 6-mesh networks at 4

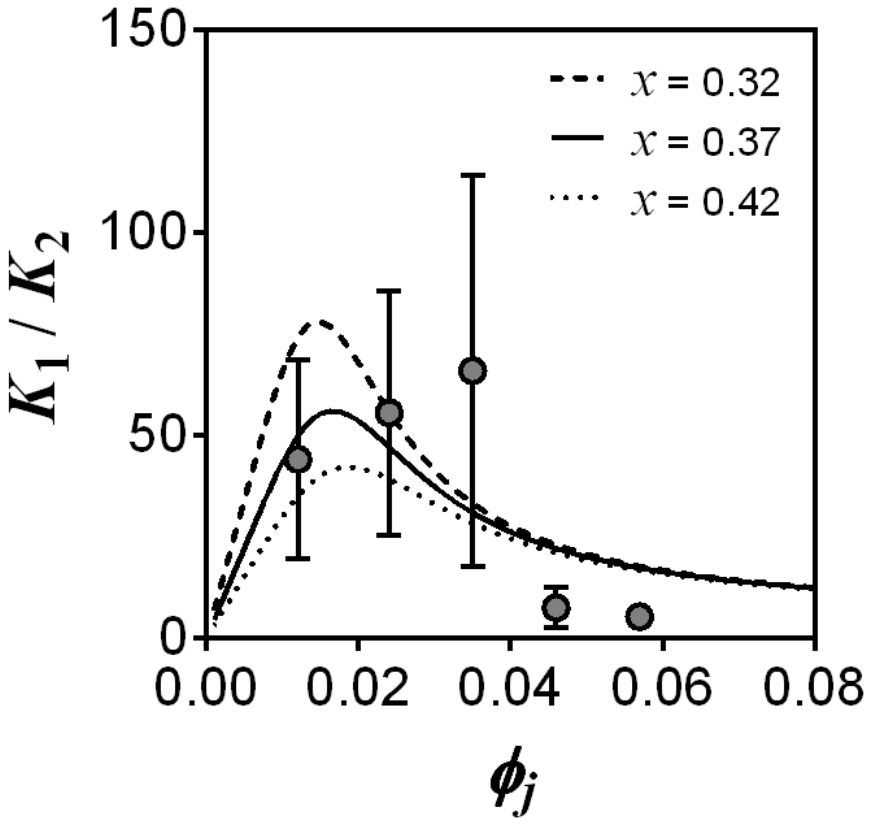

Figure 2.4: Concentration dependence of the binding constant ratio in a 6-mesh network. K_1/K_2 is proportional to ϕ_j (junction density) for small ϕ_j, then falls sharply above $\phi_j \approx 0.04$ due to a decrease in junction spacing. Equation (2.2) qualitatively captures this behavior, with $x_{min} = 0.37 \pm 0.05$, $b = 0.95$ nm and $N = 72$. Error bars depict mean ± std. deviation from $n = 76$ total measurements, with ≥ 2 measurements per probe type per concentration. The mass concentrations range from $5 - 25\%$ (w/v), i.e., $\rho = 50 - 250$ mg/mL.

additional mass concentrations, varying ρ between 50 and 250 mg/mL (equivalent to $\phi_j = 0.012 - 0.057$, all above the gelation point). The binding constants obtained from these measurements are plotted in Fig. 2.4, along with eq. (2.2) evaluated at $x_{min} = 0.37 \pm 0.05$ (optimized for the concentration dataset). Substantial formation of loops is evident experimentally at the lowest concentrations, with $K_1/K_2 \sim \phi_j$ for small ϕ_j. K_1/K_2 then falls sharply above $\phi_j = 0.035$, consistent with increased bridge formation as the junction spacing becomes smaller (with a fixed probe size). Although the experimental decrease in K_1/K_2 is sharper than eq. (2.2) predicts, the model qualitatively captures a local maximum in the data, which corresponds to a crossover between loop-dominant (low r) and bridge-dominant (high r) regimes.

Excluded volume effects not included in the model are likely to be important in the real network at higher concentrations and could shift the location of this predicted local maximum.

It is interesting to note that eq. (2.2) specifies a region at very low $\phi_j < \phi_j^* = \Omega_L/(4 - \Omega_B)$, for which $K_1 < K_2$ and the difference in binding strengths inverts. This concentration regime lies below the theoretical mean-field percolation threshold for a pentameric network, $p_c = 1/(f - 1) = 1/4$ for $f = 5$ [45]. Substituting ϕ_j^* into eq. (2.13) provides the theoretical bridge fraction at this concentration, $[B]^* = \Omega_B/4 \leq p_c$, i.e., this concentration is so low that the network no longer exists. Hence, we expect $K_1 > K_2$ for telechelic chains whenever a network is present, at least within networks assembled from pentameric crosslinking domains.

2.5 Evidence for Multisticker Chain Hopping

The presence of additional associative domains on a polymer chain increases its binding to the network. As a result, a multisticker chain with $S \geq 2$ stickers is intrinsically less likely to hop than the corresponding telechelic polymer. However, the chain will also experience additional conformational restrictions whenever two or more of its stickers form a bridge between spatially separated junctions. The entropic penalty for "full" association of a multisticker chain (i.e., all stickers in the bridge state) may thus be very high, such that binding is substantially reduced. In analogy to telechelic polymers, we can define an effective network binding coefficient K_{eff} for multisticker chains as:

$$K_{eff} = \left[\sum_{j=1}^{S} \left(\prod_{i=1}^{j} K_i \right) \right]^{1/S}, \tag{2.5}$$

such that $D_0/D_S = 1 + K_{eff}^S$ (cf. eq. (2.4). For telechelic polymers, the effect of local network structure is to reduce K_2 relative to K_1, such that $K_{eff} = (K_l + K_1 K_2)^{1/2}$ is smaller than expected. Similarly for a multisticker chain, the effective binding strength of a given sticker is attenuated by the presence of other concurrently bound stickers on the same chain such that K_{i+1} is always less than K_i, thereby reducing K_{eff} even further (relative to the case of the same polymer in an uncorrelated or mean-field network). As with telechelics, this should amplify the fraction of free chains and thus the probability that a chain will migrate by "hopping" (complete network disengagement before rebinding) (Fig. 2.1). Comparing the predicted binding strengths and diffusivities of multisticker chains with experiments thus

provides a stringent test of the effect of local network structure on equilibrium chain transport.

We synthesized multisticker probes with $S = 3$ and $S = 5$ stickers and compared their effective binding strengths in a telechelic 6-mesh network to the exact theoretical predictions for polymers of this type (see Appendix for a derivation of the key equations; representative binding configurations for a chain with $S = 3$ stickers are presented in Fig. 2.6; relative theoretical values of each K_i for $S = 5$ are presented in Table 2.1). To predict K_{eff} for multiblocks, the model requires an estimate for K_1, obtained by FRAP using the En* ($S = 0$) and EnP* ($S = 1$) probes. To correctly account for loops, we also integrate each loop configuration with $x_{min} = 0.26$ based on the minimization of residuals for telechelic chains in the 6-mesh (see the eq. (2.2) fit in Fig. 2.3C). The prediction for $S = 2$ thus contains some information from a model-constrained fit to data from the same probe type, whereas the predictions for $S = 3$ and $S = 5$ do not. We observe striking agreement between the new multisticker predictions and the experimental values of K_{eff} inferred from eqs. (2.4) and (2.5) (Fig. 2.5)

In analogy to telechelics, the fraction of free multisticker chains is readily computed as $[f] = [1+K_{eff}^{S}]^{-1}$, providing a simple way to estimate the contribution of hopping to the total diffusivity. Assuming the measured diffusivity D_S contains contributions from only hopping and walking, then $D_S = D_{hop} + D_{walk} = [f]D_0 + R_{mesh}^2/6\tau_b$. Here we have assumed that a bound chain can translate of order the mesh size within a bound time $\tau_b = \omega_c^{-1} \approx 1$ second, set by the relaxation rate of the network. Using the theoretical $[f]$ and experimental D_0, we can directly predict $D_{hop} = [f]D_0$ with the model. If this prediction is similar to D_S as measured by FRAP, we can infer that hopping is the dominant mode of chain migration.

Figure 2.5 plots D_S measured by FRAP together with the hopping prediction D_{hop} for all multistickers. The hopping prediction is essentially exact for $S = 2$ and $S = 3$. Remarkably, $D_{hop}/D_S = 0.36$ for $S = 5$, suggesting that ca. 36% of these multisticker chains migrate by hopping, whereas the remaining chains undergo translational motion through a new diffusive mechanism. The theoretical bound mobility of telechelic chains in the host network is $D_{walk} = R_{mesh}^2/6\tau_b = 1.61 \times 10^{-5}\mu m^2 s^{-1}$ (calculated for a 6-mesh). Guest chains with $S = 5$ stickers appear to approach this lower bound (Fig. 2.5B), suggesting that the new diffusive mode represents reorganization of the host network itself (i.e., "walking" of telechelic chains) around the multisticker guest. In support of this claim, we observe that

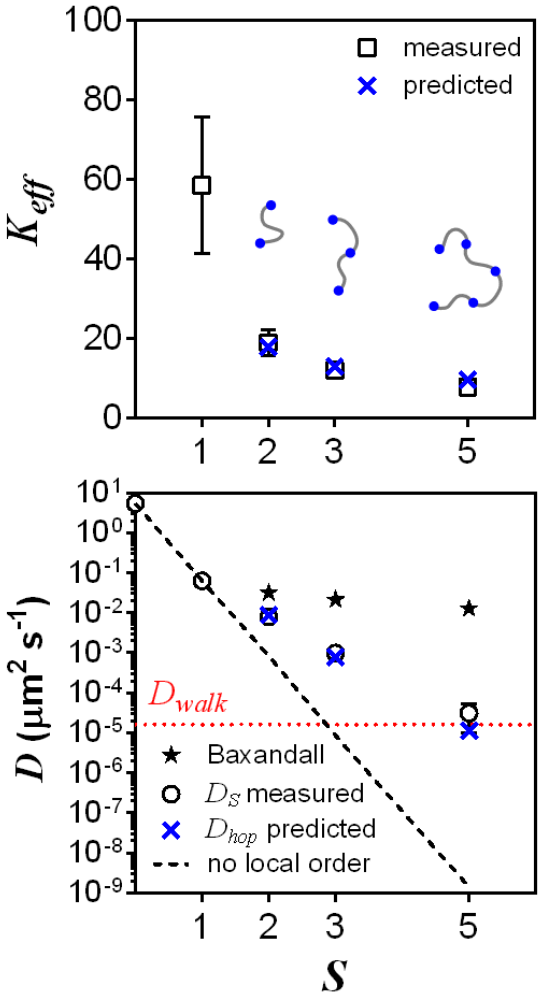

Figure 2.5: Hopping dominates the diffusion of multisticker chains in telechelic networks. (Top) Measurements of K_{eff} inferred from experimental D_S and eqs. 4 and 5 are in good agreement with model predictions for chains with $S = 2, 3$ and 5 associative domains. (Bottom) Comparison of D_S measured by FRAP and D_{hop} predicted from the thermodynamic model. All measurements were taken in 10% (w/v) 6-mesh networks using size-matched probes (i.e., the intersticker spacing N corresponds to the mesh size M). Symbols depict mean ± std. deviation from $n \geq 4$ measurements per probe type. All model predictions were made using $x_{min} = 0.26$. The prediction from Baxandall assumes $D_S \sim S^{-1}$. "No local order" assumes that all binding events have the same strength as the first association, i.e., all $K_i = K_1$. The theoretical mobility of bound chains is calculated as $D_{walk} = R_{mesh}^2/6\tau_b = 1.61 \times 10^{-5} \mu m^2 s^{-1}$.

$(D_{hop} + D_{walk})/D_S = 0.88 \approx 1$ for these guest chains. The fact that $D_S \gg D_{walk}$ holds for all but the stickiest chain is direct, model-independent evidence that walking and other diffusive modes based on bound configurations (including multichain cluster diffusion) do not contribute meaningfully to the diffusivity of any of the smaller chains.

Most notably, ignoring the influence of local network structure on effective network binding affinity leads to incorrect predictions for D_{hop} due to a drastic underestimation of the fraction of free chains. For chains with $S = 5$ stickers, for example, $[f] = [1 + (K_1)^5]^{-1} \approx 1 \times 10^{-9}$ for the case where all stickers bind with the same affinity as the first. Considering local network structure, however, provides $[f] = [1+(K_{eff})^5]^{-1} \approx 1\times10^{-5}$, i.e., the number of free chains increases by a factor of 104. This result highlights the profound extent to which entropic constraints can influence the dynamics of single chains in reversible networks. Our new dataset also provides a quantitative test of an original mean-field prediction from Baxandall, which also neglects the local structure of the network [27]. His prediction that multisticker self-diffusion should be Rouse-like, with $D_S\ S - 1$, appears too weak. It is possible that this prediction could still hold in the regime of total binding (no free chains). Such a regime is perhaps experimentally accessible for $S \gg 5$.

2.6 Conclusions

Several distinct mechanisms of chain diffusion in unentangled associative polymer networks have been proposed over the past three decades. Here we present evidence that hopping (diffusion of "free" chains that are transiently disengaged from the network), can be the dominant mode of chain transport in such systems, even in networks in which the intrinsic association strength is high. We propose a simple thermodynamic origin for this behavior: an entropic penalty that reduces the effective strength for all subsequent binding events once the first "sticker" is bound. This effect amplifies the fraction of free chains and promotes hopping, even for chains with many stickers. Predictions of the thermodynamic model explain the observed dependences of the effective diffusion coefficient on chain length (including mismatches in the lengths of network and probe chains), network junction density and number of stickers in networks formed from monodisperse artificial proteins. We believe the behavior described here to be characteristic of associative macromolecular networks of many different kinds.

2.7 Appendix

Estimation of Key n-mesh Parameters

The characteristic dimensions of differently sized meshes were estimated from protein concentration, simple geometric arguments and molecular weight data. First, the number density of junctions n_j (number of crosslinking sites per unit volume) was calculated as

$$n_j = \frac{2}{5}\left(\frac{\rho}{M}\right) N_A, \tag{2.6}$$

where ρ is the protein mass concentration in g/L, M is the molecular weight of the mesh and N_A is Avogadro's number. The factor of $2/5$ arises from the fact that each protein chain carries two coiled-coil forming domains and five of these are expected to self-assemble into a single junction, based on the crystal structure of the P domain. From eq. (2.6), the characteristic mesh size R_{mesh} was estimated by approximating the average distance between junctions as twice the radius of a sphere with the volume equal to the mean volume per junction:

$$R_{mesh} = 2\left(\frac{3}{4\pi n_j}\right)^{1/3}. \tag{2.7}$$

Values of R_{mesh} obtained from eq. (2.7) are reported in Table 2.3. To estimate ϕ_j, the fractional volume accessible to dangling chains, we use

$$\phi_j = \left(\frac{\bar{v}_p}{\frac{1000}{\rho_j} + \bar{v}_p}\right) \approx \bar{v}_p \frac{\rho_j}{1000}, \tag{2.8}$$

where $\bar{v}_p = 0.7230 mL/g$ is the partial specific volume of the protein estimated from elastin sequence data and the mean volume of individual amino acid residues [54]. Here ρ_j is the junction mass concentration in units of g/L, which is related to the total protein mass concentration ρ by $2M_P/M_{PEP}$, the ratio of the molecular weight of the P domain to that of the whole proteinP

$$\rho_j = \rho\left(\frac{2M_p}{M_{PEP}}\right). \tag{2.9}$$

where the factor of 2 arises because each chain carries two P domains capable of forming junctions. By definition, $\phi_j = n_j v_j$ where $v_j = 4\pi c^3/3$ is the local volume accessible to junction-bound chains. Here we have chosen to approximate the accessible volume using the "cluster size" c, which represents the characteristic size of a junction (this approximation is reasonable for junctions that are similar in size to the chains themselves). Since eq. (2.6) and eq. (2.8) provide n_j and ϕ_j respectively, we can obtain a rough estimate for c, the average size of a cluster,

	$K_i / \phi_j \exp(-\beta\Delta E_B)$	K_i / K_{i-1}
$i=1$	5	-
$i=2$	$\frac{\Omega_b(4N)+2\Omega_b(3N)\Omega_f+3\Omega_b(2N)\Omega_f{}^2+4\Omega_b\Omega_f{}^3}{5\Omega_f{}^4}$	0.100
$i=3$	$\frac{3\Omega_b{}^2\Omega_f{}^2+4\Omega_b(2N)\Omega_b\Omega_f+2\Omega_b(3N)\Omega_b+\Omega_b(2N)^2}{\Omega_b(4N)+2\Omega_b(3N)\Omega_f+3\Omega_b(2N)\Omega_f{}^2+4\Omega_b\Omega_f{}^3}$	0.157
$i=4$	$\frac{2\Omega_b{}^3\Omega_f+3\Omega_b(2N)\Omega_b{}^2}{3\Omega_b{}^2\Omega_f{}^2+4\Omega_b(2N)\Omega_b\Omega_f+2\Omega_b(3N)\Omega_b+\Omega_b(2N)^2}$	0.206
$i=5$	$\frac{\Omega_b{}^5}{2\Omega_b{}^3\Omega_f+3\Omega_b(2N)\Omega_b{}^2}$	0.014

Table 2.1: Exact equilibrium constants for a multisticker probe with $S = 5$ stickers. Each K_i is normalized by the factor $\phi_j \exp(-\beta\Delta E_B)$ and the numerical data for each K_i/K_{i-1} were calculated using coarse-grained data on the 6-mesh network, i.e., $b_k = 0.95$ nm, $N = 72$ and $R_{mesh} = 13.2$ nm. Ω_b and Ω_f take the same form as for telechelics (i.e., $\Omega_b = \Omega_B + \Omega_l/\phi_j$). Unless otherwise noted, $\Omega_b = \Omega(N)$ where N is the length of an equivalent freely joined chain between neighboring stickers.

from the mass concentration and molecular weight of the polymer. At 100 g/L (10% w/v) we obtain $c = 1.89$ nm in reasonable agreement with structural data on the P domain ($c = 2.31$ nm is suggested by the X-ray crystal structure of the pentameric assembly) [55]. We made a quantitative comparison between eq. (2.2) and the concentration data in Fig. 2.4 by specifying ϕ_j in terms of $c = 1.89$ nm and the mesh size R_{mesh}:

$$\phi_j = \left(\frac{2c}{R_{mesh}}\right)^3 . \tag{2.10}$$

Generalized Binding Asymmetry for Multisticker Probes

The approach described in the main text to derive K_1 and K_2 is easily generalized to determine multiple equilibrium constants K_i for a chain having S associative domains, $i \leq S$ of which are bound to the network. The objective is to compute Z_i, the sum of all chain configurations with i bound stickers, subject to the constraint of chain connectivity. For a chain with S total stickers, the number of ways N_b in which $i \leq S$ stickers may become bound is the binomial coefficient $N_b = C(s,i)$.

We can then express $Z_i = \sum_{k=1}^{N_b} Q_k$, where Q_k is the sum of all configurations available to a chain in the k^{th} configuration of the i^{th} bound state (see Fig. 2.6 for a visualization of each "k-state" for a multisticker chain having $S = 3$). The chain can be thought to consist of $S - 1$ flexible "blocks" between adjacent stickers. The total number of configurations Q_k available to the whole chain in the k^{th} bound state can be decomposed into the product of the configurations available to each $S - 1$ block, such that $Q_k \sim \prod_{j=1}^{S-1} \Omega_{k,j}$. In analogy to telechelic chains, $\Omega_{k,j}$ is calculated as either Ω_f or $\Omega_b = \Omega_B + \Omega_L/\phi_j$, depending on whether the block under consideration is flanked by two (Ω_b) or fewer than two (Ω_f) bound stickers.

Consider the case of a chain with $S = 3$ evenly spaced stickers along its backbone, with $j = 2$ blocks of molecular weight N and Kuhn length b_k (Fig. 2.6). For $i = 0$, there is only $N_b = 1$ state (the free state with all stickers unbound) and $Z_0 = Q_0 = \Omega_f^2$. When one sticker binds ($i = 1$) there are possible configurations ("k-states") and binding restricts the chain to a volume fraction ϕ_j. Assuming that none of the blocks loses substantial conformational entropy during this single sticking event provides $Z_1 = \sum_{k=1}^{3} Q_k = \sum_{k=1}^{3} \phi_j \Omega_{k,1} \Omega_{k,2} \approx 3\phi_j \Omega_f^2$. Then from eq. (2.1), $K_1 = Z_1/Z_0 \exp(-\beta\Delta E) = 3\phi_j \exp(-\beta\Delta E)$ for a 3-sticker chain. Note that this is $3/2$ the value of a 2-sticker (telechelic) chain, which arises as a direct consequence of the extra sticker.

Similar to telechelics, states with $i = 2$ bound blocks must pay the entropic cost associated with simultaneously locating two spatially correlated ("well-separated") junctions, or else form loops. The entropy for a chain with two adjacent bound stickers and one terminal dangling end (see $k = 2$ and $k = 3$ in Fig. 2.6) is $Q_2 = Q_3 = \phi_j^2 \Omega_f \Omega_b$. For the state with one unbound sticker in the middle ($k = 1$), the conformations of each block are coupled. We can apply the self-similarity property of Gaussian chains to write $Q_1 = \phi_j^2 \Omega_b(2N)$, i.e., the chain is effectively telechelic with a block length of $2N$. Summing over all k-states we obtain $Z_2 = \phi_j^2(2Q_2 + Q_1)$ and $K_2 = Z_2/Z_1 \exp(-\beta\Delta E) = \phi_j \exp(-\beta\Delta E)[2\Omega_f\Omega_b + \Omega_b(2N)]/3\Omega_f^2$. When all three stickers are bound ($i = 3$), there is again only one possible state. In this case $Z_3 = \phi_j^3 \Omega_b^2$ and the equilibrium constant is $K_3 = \phi_j \exp(-\beta\Delta E)\Omega_b^2/[2\Omega_f\Omega_b + \Omega_b(2N)]$. Analogous combinatorial considerations provide expressions for K_i for chains with even more stickers. The results for the case of $S = 5$ are presented in Table 2.1.

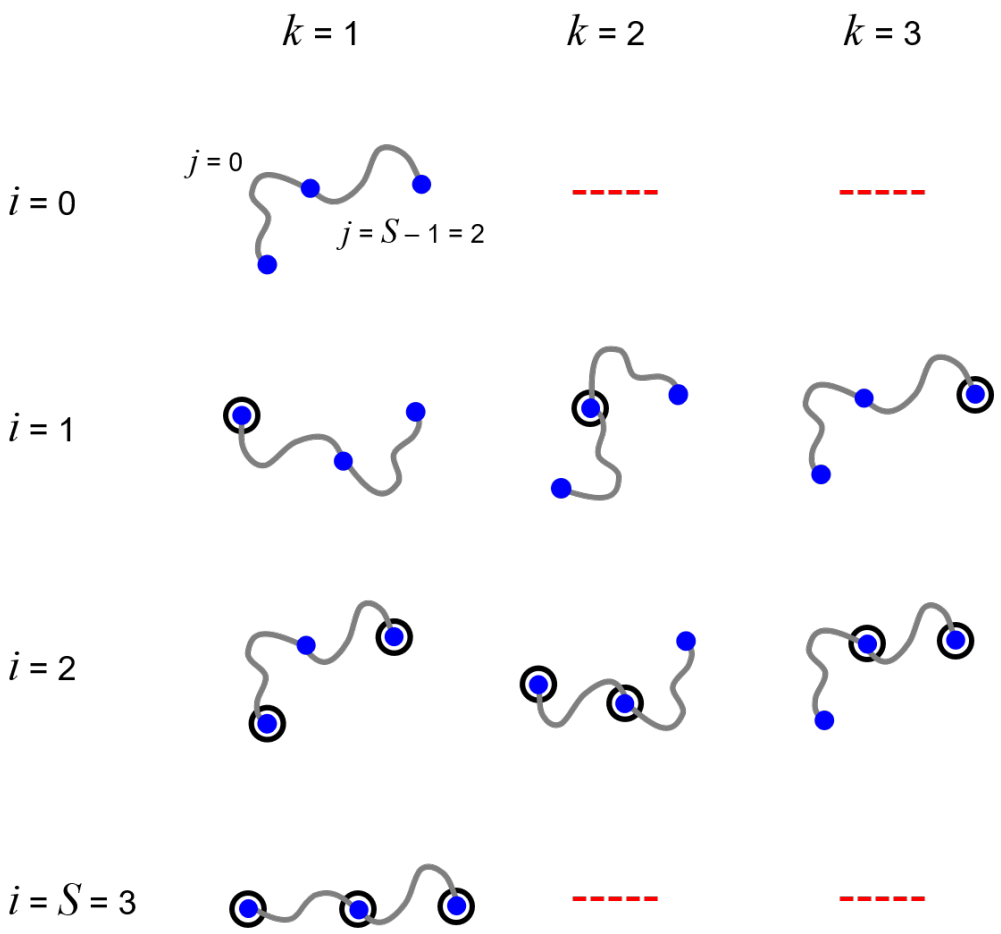

Figure 2.6: Binding configurations of a chain with $S = 3$ stickers. The chain has $k \leq C(S,i)$ possible bound states for each $i \leq S$ number of bound stickers, where $C(S,i)$ is the binomial coefficient. The sum $j = S - 1$ runs over the total number of independent blocks.

Selection of Limits on the Looping Integral

Because the model (eq. (2.2)) predicts K_1 and K_2 in terms of the fraction of bridged $[B]$ and looped $[L]$ chains, it is possible to compare the theoretical fraction of bridged chains to the fraction of elastically effective chains $G'_\infty/G_{phantom}$ estimated from rheology by phantom network theory (Table 2.3 and Fig. 2.8). For a given choice of the cluster dimension c, this constraint fixes the limits of the looping

integral l. Recall the definitions of each equilibrium constant and that $Z_0 = \Omega_f = 1$:

$$K_1 = \frac{[d]}{[f]} = 2\phi_j \exp(-\beta\Delta E),$$

$$K_L = \frac{[L]}{[d]} = \frac{\Omega_L}{2\Omega_f} \exp(-\beta\Delta E) = K_1\Omega_L/4\phi_j/4\phi_j, \tag{2.11}$$

$$K_B = \frac{[B]}{[d]} = \frac{\phi_j\Omega_B}{2\Omega_f} \exp(-\beta\Delta E) = K_1\Omega_B/4.$$

If we require the normalization $[f] + [d] + [B] + [L] = 1$, then $[B] = G_\infty^{'}/G_{phantom}$ is exact and we can solve for $[B]$ in terms of known equilibrium constants

$$[B] = \left[1 + \frac{1}{\Omega_B}\left(\frac{\Omega_L}{\phi_j} + \frac{4}{K_1} + \frac{4}{K_1^2}\right)\right]^{-1}. \tag{2.12}$$

Assuming $K_1 >> 1$, the above expression simplifies to:

$$[B] = \left[1 + \frac{\Omega_L}{\Omega_B\phi_j}\right]^{-1} = f(l) = G_\infty^{'}/G_{phantom}. \tag{2.13}$$

Eq. (2.13) may be used to estimate l (or equivalently, $x = l/c$) provided the mesh size R_{mesh} is known and the polymer is properly coarse-grained as an equivalent, freely-jointed chain (i.e., N and b_k are also known). Representative plots of $G_\infty^{'}/G_{phantom}$ versus l are shown in Fig. 2.8 and the $x_{rheo} - l_{rheo}/c$ values obtained using this scheme are presented in Table 2.3.

Coarse-Graining of Probes as Equivalent Freely-Jointed Chains

Central to the comparison of experimental data with eq. (2.2) is an estimate for the probe size in terms of model parameters b_k and N, the Kuhn length and number of monomers for an equivalent freely jointed chain. These parameters are in turn set by the Flory characteristic ratio C_∞ , an empirical coefficient that relates the "true" chain size to that of an equivalent freely-jointed chain. The relations $R_{probe} = (C_\infty n_p)^{1/2} l_p = b_k N^{1/2}$ and $R_{max} = n_p l_p$ hold for an ideal polypeptide chain, where n_p is the number of peptide residues between neighboring associative domains and $l_p = 0.38$ nm is the linear $C_\alpha - C_\alpha$ distance of an amino acid residue [50]. $C_\infty = 2.51$ was selected based on previous calculations of conformational energy maps for elastin pentapeptides [51]. $C_\infty = 2 - 3$ is typical for denatured glycine-rich proteins in a θ-solvent [50, 52]. Moreover, measurements of the second virial coefficient for

	MW_{eff} (Da)	n_p	R_{probe} (nm)	R_{max} (nm)	b_k (nm)	N	M_0 (Da)
3-probe	8,121	104	6.1	39.5	0.95	41	196
6-probe	14,245	181	8.1	68.8	0.95	72	198
12-probe	26,493	335	11.0	127.3	0.95	133	199
24-probe	50,990	643	15.3	244.3	0.95	256	199
48-probe	99,982	1259	21.4	478.4	0.95	502	199

Table 2.2: Coarse graining of probe size based on the Flory characteristic ratio. The following parameters were used to obtain a quantitative comparison of the experimental dataset to the asymmetric binding model. The value n_p reflects the number of peptide bonds between each P domain on PEnP-type probes. The molecular weight of this inter-sticker region ("MW_{eff}") is also shown. To obtain b_k and N for each probe, $l_p = 0.38$ nm was used as the linear $C_\alpha - C_\alpha$ distance of an amino acid residue and C_∞ was taken as the Flory characteristic ratio. M_0 represents the effective molar mass of a single Kuhn monomer.

	3-mesh	6-mesh	12-mesh	24-mesh
M (Da)	22,632	28,756	41,004	65,501
R_{mesh} (nm)	12.2	13.2	14.8	17.3
$G'_\infty/G_{phantom}$	0.59	0.74	0.82	0.67
x_{rheo} (nm)	0.15	0.28	0.42	0.80
x_{min} (nm)	0.24	0.26	0.43	0.35

Table 2.3: Experimental parameters and exponent data for each mesh. M represents the molar mass of each n-mesh (including P domains). The mesh size was calculated as $R_{mesh} = 2(3/4\pi n_j)^{1/3}$. The fraction of elastically effective chains, $G'_\infty/G_{phantom}$, is the average value measured from rheology ($n \geq 2$ independent measurements) with $G_{phantom} = \rho RT(1 - 2/f)/M$, where $f = 5$ for a pentameric network junction. $x_{rheo} = l_{rheo}/c$ was determined using eq. (2.13). Each $x_{min} = l_{min}/c$ was determined from minimizing the residuals between model-constrained fits of eq. (2.3) to experimental values in each mesh (Figures S11 and S12).

model elastins suggest a θ-temperature between 40 and 45°C [53]. The thermal blob size is estimated to be $\xi_T \cong l_p C_\infty^2 \nu^{-1} \approx 45$ nm, where the dimensionless excluded volume parameter $\nu = 2A_2 M_m^2 / l_p^3 N_a v$ (here $M_m \approx 79$ g/mol is the molar mass of the monomer of size l_p) is estimated using the second virial coefficient provided by Hassouneh et al [53]. Our chains, which have sizes ranging from 6 – 21 nm, do not consist of even one thermal blob (see Table 2.2), justifying our treatment of them as ideal. Finally, the length of a Kuhn monomer is calculated as $b_k = C_\infty n_p l_p^2 / R_{max}$ and the equivalent freely jointed chain is composed of $N = R_{max}^2 / C_\infty n_p l_p^2$ such monomers, each with an effective molar mass of M_0 [45]. Parameters calculated in this manner are presented below in Table 2.2.

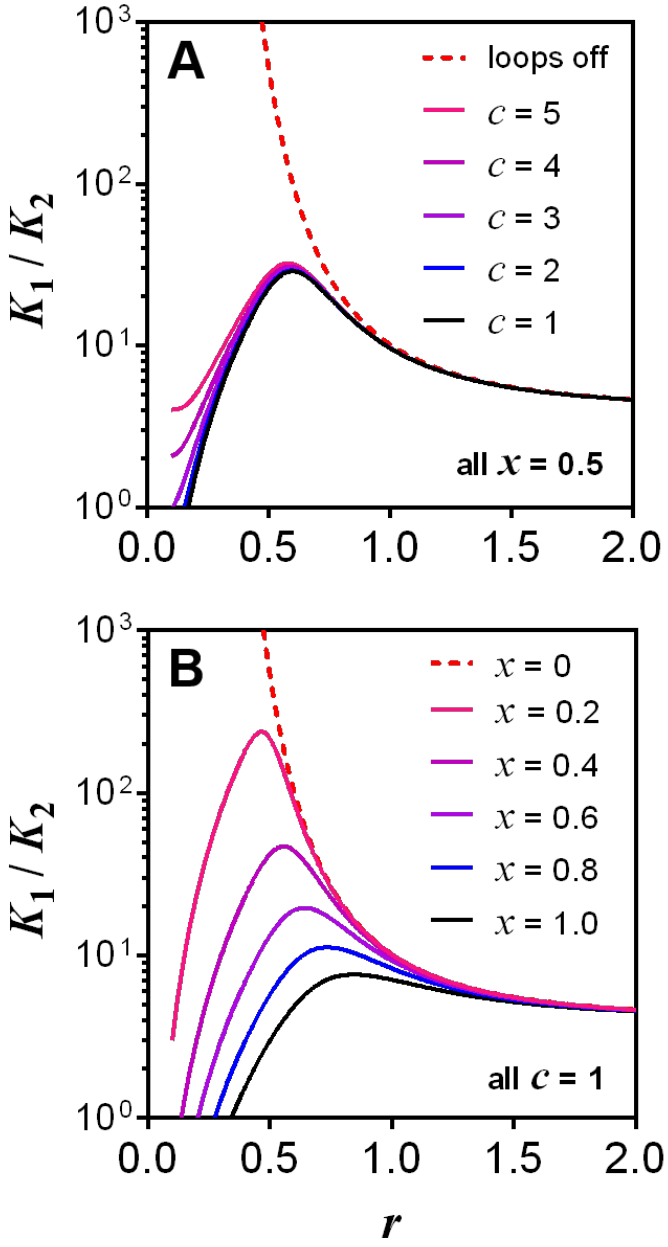

Figure 2.7: Asymmetric binding model is invariant with cluster size "c" for fixed "$x \equiv l/c$". Shown are predictions from eq. (2.2) as a function of the reduced probe size $r \equiv R_{probe}/R_{mesh} \sim N^{1/2}M^{-1/3}$ for various choices of the cluster size "c" and the integration limit for the looping integral "l." (A) The cluster dimension was taken to be $c = 1 - 5$ nm, $R_{mesh} = 10$ nm, $b_k = 1$ nm and x (dimensionless) was fixed at 0.5. Equation (2.3) was used to plot the "loops off" case. The behavior of eq. (2.2) is approximately invariant under several choices of $c < R_{mesh}$. (B) For a fixed choice of cluster size of $c = 1$, the limits of the looping integral (specified by $x = l/c$) determine the behavior of eq. (2.2). For all predictions described in the main text, $c = 1.89$ nm was employed based on the molecular weight of the P domain.

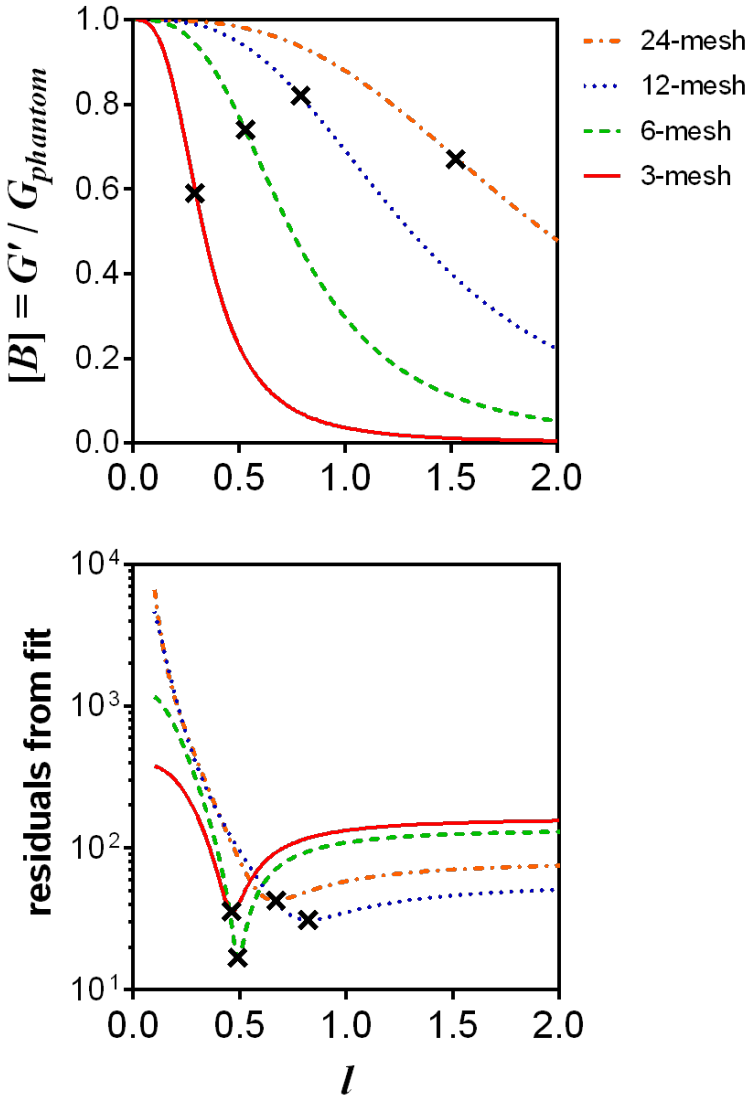

Figure 2.8: Selection criteria for the limits of the looping integral. In order to estimate $\Omega_L/\phi_j = f(l)$ in a non-arbitrary way, estimates for the upper integration limit $l = xc$ are required (using $c = 1.89$ nm). (Top) Matching the experimental fraction of elastically effective chains to predictions from eq. (2.13) fixes this limit precisely, providing x_{rheo} for each mesh. (Bottom) Alternatively, varying l in order to minimize the residuals between experimental K_1/K_2 values and constrained fits from eq. (2.2) provides x_{min}. The integration limits obtained by either method are similar across all four meshes and are presented in Table 2.3.

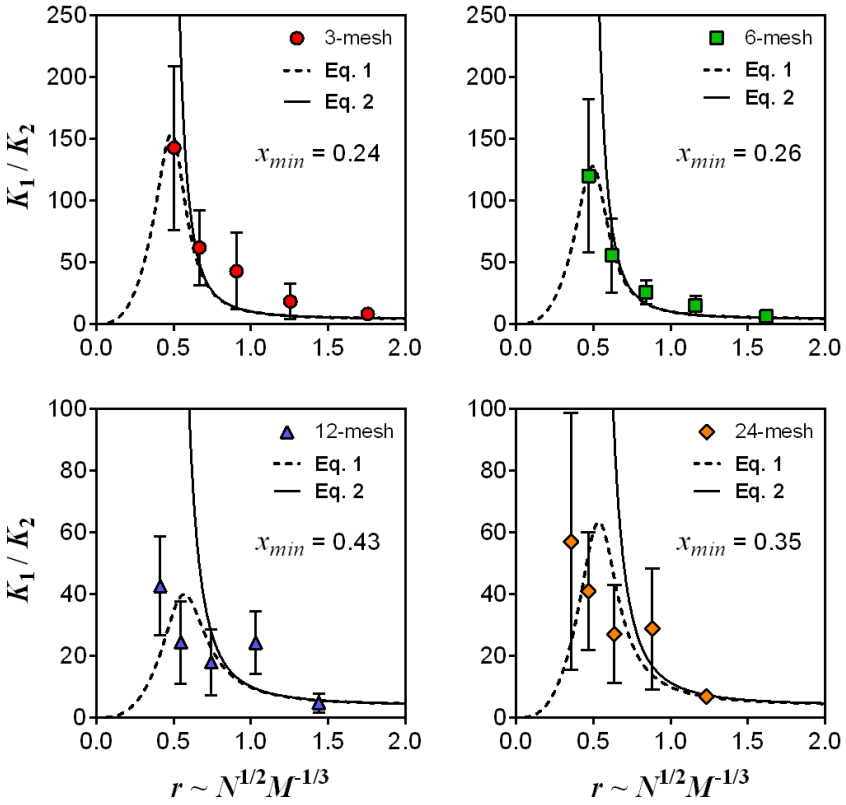

Figure 2.9: Single-parameter "best fits" of eq. (2.2) to experimental K_1/K_2, analogous to Fig. 2.3C. Shown are experimental values of K_1/K_2 measured in each mesh (298 total measurements, $\geq$ 4 per probe, error bars represent mean $\pm$ std. dev.), together with single-parameter "best fits" from eq. (2.2) using $x_{min} = l_{min}/c$ obtained from residuals minimization and the universal "loop-free" prediction from eq. (2.3). $x_{min} = 0.26$ from the 6-mesh was used to construct the "master curve" in Fig. 2.3D, as well as to predict hopping for the multisticker probes in Fig. 2.5.

References

[1] Guo, M.; Pitet, L. M.; Wyss, H. M.; Vos, M.; Dankers, P. Y. W.; Meijer, E. W. Tough Stimuli-responsive Supramolecular Hydrogels with Hydrogen-bonding Network Junctions. *J. Am. Chem. Soc.* **2014**, *136*, 6969–6977.

[2] Cordier, P.; Tournilhac, F.; Soulie-ziakovic, C.; Leibler, L. Self-healing and Thermoreversible Rubber from Supramolecular Assembly. *Nature* **2008**, *451*, 977–980.

[3] Zhou, Z.; Yan, X.; Cook, T. R.; Saha, M. L.; Stang, P. J. Engineering Functionalization in a Supramolecular Polymer: Hierarchical Self-organization of

Triply Orthogonal Non-covalent Interactions on a Supramolecular Coordination Complex Platform. *J. Am. Chem. Soc.* **2016**, *138*, 806–809.

[4] Herbst, F.; Seiffert, S.; Binder, W. H. Dynamic Supramolecular Poly(isobutylene)s for Self-healing Materials. *Polym. Chem.* **2012**, *3*, 3084–3092.

[5] Yount, W. C.; Juwarker, H.; Craig, S. L. Orthogonal Control of Dissociation Dynamics Relative to Thermodynamics in a Main-chain Reversible Polymer. *J. Am. Chem. Soc.* **2003**, *125*, 15302–15303.

[6] Yount, W. C.; Loveless, D. M.; Craig, S. L. Small-molecule Dynamics and Mechanisms Underlying the Macroscopic Mechanical Properties of Coordinatively Cross-linked Polymer Networks. *J. Am. Chem. Soc.* **2005**, *127*, 14488–14496.

[7] Xu, D.; Craig, S. L. Scaling Laws in Supramolecular Polymer Networks. *Macromolecules* **2011**, *44*, 5465–5472.

[8] Grindy, S. C.; Learsch, R.; Mozhdehi, D.; Cheng, J.; Barrett, D. G.; Guan, Z.; Messersmith, P. B.; Holten-andersen, N. Control of Hierarchical Polymer Mechanics with Bioinspired Metal-coordination Dynamics. *Nat. Mater.* **2015**, *14*, 1210–1216.

[9] Holten-Andersen, N.; Harrington, M. J.; Birkedal, H.; Lee, B. P.; Messersmith, P. B.; Lee, K. Y. C.; Waite, J. H. PH-induced Metal-ligand Cross-links Inspired by Mussel Yield Self-healing Polymer Networks with Near-covalent Elastic Moduli. *Proc. Natl. Acad. Sci. USA* **2011**, *108*, 2651–2655.

[10] Tang, S.; Habicht, A.; Li, S.; Seiffert, S.; Olsen, B. D. Self-diffusion of Associating Star-shaped Polymers. *Macromolecules* **2016**, *49*, 5599–5608.

[11] Annable, T.; Buscall, R.; Ettelaie, R.; Whittlestone, D. The Rheology of Solutions of Associating Polymers: Comparison of Experimental Behavior with Transient Network Theory. *J. Rheol.* **1993**, *37*, 695.

[12] Petka, W. A.; Harden, J. L.; McGrath, K. P.; Wirtz, D.; Tirrell, D. A. Reversible Hydrogels from Self-assembling Artificial Proteins. *Science* **1998**, *281*, 389–392.

[13] Tang, S.; Wang, M.; Olsen, B. D. Anomalous Self-diffusion and Sticky Rouse Dynamics in Associative Protein Hydrogels. *J. Am. Chem. Soc.* **2015**, *137*, 3946–3957.

[14] Olsen, B. D.; Kornfield, J. A.; Tirrell, D. A. Yielding Behavior in Injectable Hydrogels from Telechelic Proteins. *Macromolecules* **2010**, *43*, 90949099.

[15] Rubinstein, M.; Semenov, A. N. Thermoreversible Gelation in Solutions of Associating Polymers. 2. Linear Dynamics. *Macromolecules* **1998**, *31*, 1386–1397.

[16] Lutolf, M. P.; Hubbell, J. A. Synthetic Biomaterials As Instructive Extracellular Microenvironments for Morphogenesis in Tissue Engineering. *Nat. Biotechnol.* **2005**, *23*, 47–55.

[17] McKinnon, D. D.; Domaille, D. W.; Cha, J. N.; Anseth, K. S. Biophysically Defined and Cytocompatible Covalently Adaptable Networks As Viscoelastic 3d Cell Culture Systems. *Adv. Mater.* **2014**, *26*, 865–872.

[18] Li, J.; Li, X.; Ni, X.; Wang, X.; Li, H.; Leong, K. W. Self-assembled Supramolecular Hydrogels Formed by Biodegradable Peo-phb-peo Triblock Copolymers and Alpha-cyclodextrin for Controlled Drug Delivery. *Biomaterials* **2006**, *27*, 4132–4140.

[19] Wang, C.; Wu, H.; Chen, Z.; McDowell, M. T.; Cui, Y.; Bao, Z. Self-healing Chemistry Enables the Stable Operation of Silicon Microparticle Anodes for High-energy Lithium-ion Batteries. *Nat. Chem.* **2013**, *5*, 1042–1048.

[20] Tee, B. C. . K.; Wang, C.; Allen, R.; Bao, Z. An Electrically and Mechanically Self-healing Composite with Pressure- and Flexion-sensitive Properties for Electronic Skin Applications. *Nat. Nanotechnol.* **2012**, *7*, 825–832.

[21] Timney, B. L.; Raveh, B.; Mironska, R.; Trivedi, J. M.; Kim, S. J.; Russel, D.; Wente, S. R.; Sali, A.; Rout, M. P. Simple Rules for Passive Diffusion through the Nuclear Pore Complex. *J. Cell Biol.* **2016**, *215*, 57–76.

[22] Kim, M.; Chen, W. G.; Kang, J. W.; Glassman, M. J.; Ribbeck, K.; Olsen, B. D. Artificially Engineered Protein Hydrogels Adapted from the Nucleoporin Nsp1 for Selective Biomolecular Transport. *Adv. Mater.* **2015**, *27*, 4207–4212.

[23] Martino, M. M.; Briquez, P. S.; Guc, E.; Tortelli, F.; Kilarski, W. W.; Metzger, S.; Rice, J. J.; Kuhn, G. A.; Muller, R.; Swartz, M. A.; Hubbell, J. A. Growth Factors Engineered for Super-affinity to the Extracellular Matrix Enhance Tissue Healing. *Science* **2014**, *343*, 885–888.

[24] Chen, Q.; Tudryn, G. J.; Colby, R. H. Ionomer Dynamics and the Sticky Rouse Model. *J. Rheol.* **2013**, *57*, 1441–1462.

[25] Rapp, P. B.; Omar, A. K.; Shen, J. J.; Buck, M. E.; Wang, Z.-g.; Tirrell, D. A. Analysis and Control of Chain Mobility in Protein Hydrogels. *J. Am. Chem. Soc.* **2017**, *139*, 3796–3804.

[26] Shen, W.; Kornfield, J. A.; Tirrell, D. A. Dynamic Properties of Artificial Protein Hydrogels Assembled through Aggregation of Leucine Zipper Peptide Domains. *Macromolecules* **2007**, *40*, 689–692.

[27] Baxandall, L. G. Dynamics of Reversibly Cross-linked Chains. *Macromolecules* **1989**, *22*, 1982–1988.

[28] Semenov, A. N.; Rubinstein, M. Thermoreversible Gelation in Solutions of Associative Polymers. 1. Statics. *Macromolecules* **1998**, *31*, 1373–1385.

[29] Green, M. S.; Tobolsky, A. V. A New Approach to the Theory of Relaxing Polymeric Media. *J. Chem. Phys.* **1946**, *14*, 80–92.

[30] Tanaka, F.; Edwards, S. F. Viscoelastic Properties of Physically Cross-linked Networks - Transient Network Theory. *Macromolecules* **1992**, *25*, 1516–1523.

[31] Tripathi, A.; Tam, K. C.; McKinley, G. H. Rheology and Dynamics of Associative Polymers in Shear and Extension: Theory and Experiments. *Macromolecules* **2006**, *39*, 1981–1999.

[32] Ramirez, J.; Dursch, T. J.; Olsen, B. D. A Molecular Explanation for Anomalous Diffusion in Supramolecular Polymer Networks. *Macromolecules* **2018**, *51*, 2517–2525.

[33] Lodge, T. P.; Rotstein, N. A.; Prager, S. *Advances in Chemical Physics*; John Wiley & Sons, Ltd, 2007; pp 1–132.

[34] Lodge, T. P. Reconciliation of the Molecular Weight Dependence of Diffusion and Viscosity in Entangled Polymers. *Phys. Rev. Lett.* **1999**, *83*, 3218–3221.

[35] McLeish, T. C. B. Tube Theory of Entangled Polymer Dynamics. *Adv. Phys.* **2002**, *51*, 1379–1527.

[36] Doi, M.; Edwards, S. F. *The Theory of Polymer Dynamics*; Oxford University Press, 1986.

[37] Omar, A. K.; Wang, Z.-g. Shear-induced Heterogeneity in Associating Polymer Gels: Role of Network Structure and Dilatancy. *Phys. Rev. Lett.* **2017**, *119*, 117801.

[38] Hill, T. L. *An Introduction to Statistical Thermodynamics*; Dover Publications, 1986.

[39] Wei, M.-h.; Li, B.; David, R. L. A.; Jones, S. C.; Sarohia, V.; Schmitigal, J. A.; Kornfield, J. A. Megasupramolecules for Safer, Cleaner Fuel by End Association of Long Telechelic Polymers. *Science* **2015**, *350*, 72–75.

[40] Levene, S. D.; Giovan, S. M.; Hanke, A.; Shoura, M. J. The Thermodynamics of DNA Loop Formation, from J to Z. *Biochem. Soc. Trans.* **2013**, *41*, 513–518.

[41] Jacobson, H.; Stockmayer, W. H. Intramolecular Reaction in Polycondensations .1. the Theory of Linear Systems. *J. Chem. Phys.* **1950**, *18*, 1600–1606.

[42] Wang, M.; Brady, J. F. Microstructures and Mechanics in the Colloidal Film Drying Process. *Soft Matter* **2017**, *13*, 8156–8170.

[43] Semenov, A. N.; Nyrkova, I. A.; Cates, M. E. Phase Equilibria in Solutions of Associating Telechelic Polymers - Rings vs Reversible Network. *Macromolecules* **1995**, *28*, 7879–7885.

[44] Rapp, P. B.; Omar, A. K.; Silverman, B. R.; Wang, Z.-G.; Tirrell, D. A. Mechanisms of Diffusion in Associative Polymer Networks: Evidence for Chain Hopping. *J. Am. Chem. Soc.* **2018**, *140*, 14185–14194.

[45] Rubinstein, M.; Colby, R. *Polymer Physics*; OUP Oxford, 2003.

[46] Sprague, B. L.; Pego, R. L.; Stavreva, D. A.; McNally, J. G. Analysis of Binding Reactions by Fluorescence Recovery After Photobleaching. *Biophys. J.* **2004**, *86*, 3473–3495.

[47] Soumpasis, D. M. Theoretical-analysis of Fluorescence Photobleaching Recovery Experiments. *Biophys. J.* **1983**, *41*, 95–97.

[48] Rouse, P. E. A Theory of the Linear Viscoelastic Properties of Dilute Solutions of Coiling Polymers. *J. Chem. Phys.* **1953**, *21*, 1272–1280.

[49] de Gennes, P. G. Reptation of a Polymer Chain in Presence of Fixed Obstacles. *J. Chem. Phys.* **1971**, *55*, 572.

[50] Miller, W. G.; Goebel, C. V. Dimensions of Protein Random Coils. *Biochemistry (Mosc.)* **1968**, *7*, 3925.

[51] Debolt, L. C.; Mark, J. E. Theoretical-study of the Thermoelastic Properties of Elastin Model Chains. *Polymer* **1987**, *28*, 416–422.

[52] Mandelkern, L.; Mattice, W. L. Development of Ordered Structures in Sequential Copolypeptides Containing L-Proline and γ-Hydroxy-L-proline. *10*, 1926–1933.

[53] Hassouneh, W.; Zhulina, E. B.; Chilkoti, A.; Rubinstein, M. Elastin-like Polypeptide Diblock Copolymers Self-assemble into Weak Micelles. *Macromolecules* **2015**, *48*, 4183–4195.

[54] Harpaz, Y.; Gerstein, M.; Chothia, C. Volume Changes on Protein Folding. *Structure* **1994**, *2*, 641–649.

[55] Malashkevich, V. N.; Kammerer, R. A.; Efimov, V. P.; Schulthess, T.; Engel, J. The Crystal Structure of a Five-Stranded Coiled Coil in COMP: A Prototype Ion Channel? *Science* **1996**, *274*, 761–765.

Chapter 3

NONLINEAR DYNAMICS AND RHEOLOGY OF ASSOCIATING POLYMER GELS

We study associating polymer gels under steady shear using Brownian dynamics simulation to explore the interplay between the network structure, dynamics and rheology. For a wide range of flow rates, we observe the formation of shear bands with a pronounced difference in shear rate, concentration and structure. A striking increase in the polymer pressure in the gradient direction with shear, along with the inherently large compressibility of the gels, is shown to be a crucial factor in destabilizing homogeneous flow through shear-gradient concentration coupling (SCC). We find that shear has only a modest influence on the degree of association, but induces marked spatial heterogeneity in the network connectivity. We attribute the increase in the polymer pressure (and polymer mobility) to this structural reorganization.

This chapter includes content from our previously published article:

Omar, A. K.; Wang, Z.-G. Shear-Induced Heterogeneity in Associating Polymer Gels: Role of Network Structure and Dilatancy. *Phys. Rev. Lett.* **2017**, *119*, 117801. DOI:10.1103/PhysRevLett.119.117801

3.1 Introduction

Associating polymers (APs) in dilute solution can aggregate into multichain clusters when the "sticker" (the physically associating moiety) attraction energy exceeds the thermal energy kT. Near the overlap concentration, sticker clusters can be bridged by polymer strands and form an interconnected volume spanning network – a physical gel [1–3]. Such gels are found in both natural and synthetic systems and display a striking array of rheological behavior, including strain stiffening [4], negative normal stresses [5], shear thickening [6, 7], shear thinning [8] and shear banding [9–15].

Despite the ubiquity and versatility of physical gels, a fundamental understanding of the interplay between their microstructure, dynamics and rheological properties remains a challenging and open problem. For instance, while experiments and simulations of associative networks (including both AP [13–15] and colloidal [16] gels) under simple shear have observed spatial inhomogeneities in both shear rate and density, suggesting some form of shear-gradient concentration coupling (SCC) [17–

20], the microscopic mechanism for the instability is unclear. Mean-field based models [21–23] of AP rheology have largely focused on chain elasticity and have not accounted for density inhomogeneity (e.g., chain migration) which would require a constitutive relation describing the solute pressure (the driving force for chain migration) as a function of shear-rate and concentration. To date, no such relation has been explored for physical gels - largely due to the experimental difficulty in measuring the pressure of a single species in solution under shear [24]. Furthermore, the observation of SCC in both AP and colloidal gels suggests that the common physics between the gels - such as network connectivity and transient particle localization - may play a key role in driving the instability.

In this work, we report results from Brownian dynamics simulations of an AP gel under steady shear in the nonlinear, shear-thinning, regime. The polymers we study have multiple associating sticker groups along the backbone, a prevalent building block of natural and synthetic gels. Our study reveals that within a broad range of applied shear rate, the gel separates into two distinct bands with substantially different shear rate and concentration. However, the applicability of existing SCC mechanisms to AP gels is unclear. While Reynolds "dilatancy", or the tendency for increased particle pressure with shear, has been proposed as a driving force for shear-induced particle migration [24, 25] and shear banding [26] in *repulsive* systems such as colloidal suspensions and glasses, the effect is marginal for dilute conditions [27]. Shear-induced turbidity in polymer [28] and wormlike micellar surfactant [29, 30] solutions can be the result of a coupling of elastic stress with concentration and shear [31, 32]. However, this coupling is typically more pronounced in high molecular weight, well-entangled solutions [33].

Here, we show that AP gels exhibit a significant microstructural reorganization in response to the elastic stresses due to shear. Crucially, we find the degree of association only decreases slightly with shear, but the spatial distribution of the network *connectivity* undergoes striking changes – the initial space-spanning network is broken into multiple smaller domains whose size is controlled by the shear rate. The loose connection between theses distinct domains significantly enhance the polymer mobility and pressure in the gradient direction. We propose that this "network "dilation", coupled with the inherently large compressibility (low osmotic pressure) of our gels, plays a crucial role in the observed SCC.

Our simulation system consists of 300 chains of $N = 100$ beads with 10 evenly spaced stickers along the backbone. We use a standard Kremer-Grest model to

describe the chains [34]. The interaction between the non-sticker groups and between a sticker and non-sticker is modeled by the WCA potential [35] with diameter $\sigma_{LJ} = 1$, energy $\epsilon_{LJ} = 1$, thus setting the units of length and energy, respectively. The Lennard-Jones time $\tau_{LJ} = \sqrt{m\sigma_{LJ}^2/\epsilon_{LJ}} = 1$ sets the time scale. The interaction between the stickers is a shifted LJ potential truncated at $r_c = 2.5$ with a well depth of ϵ_{ss}. The chain connectivity is described with a FENE potential using the canonical parameters (spring constant $k = 30$ and fully stretched bond length $R_0 = 1.5$). We set a Cartesian coordinate such that x, z and y refer to the flow, gradient and vorticity directions, respectively. We use a system box size of $V = L_x L_y L_z$ with $L_x = 10.3R_g$ and $L_y = L_z = 8.8R_g$ where $R_g \approx 6.8$ is the equilibrium radius of gyration of chains without sticker associations (hereafter referred to as Rouse chains). We impose periodic boundary conditions in the flow and vorticity directions and the Lees-Edwards boundary condition in the gradient direction [36]. The bead number density is $\bar{\rho} = 0.12$, ensuring that the solution is semidilute ($\bar{\rho} \approx 1.6\rho^*$ where ρ^* is the overlap concentration of the Rouse system).

To study larger system sizes, we ignore hydrodynamic interactions and use Langevin dynamics to evolve our system:

$$m\boldsymbol{r} = \boldsymbol{f_p} + \boldsymbol{f_b} - \zeta\left(\boldsymbol{r} - \boldsymbol{r}\cdot\boldsymbol{\nabla v}_s\right), \tag{3.1}$$

where $\boldsymbol{r}$ and $\boldsymbol{f_p}$ are, respectively, the particle position and interparticle force and the particle mass m is set at unity. The Brownian force $\boldsymbol{f_b}$ is taken to be a white noise with a mean of 0 and a variance of $2kT\zeta$ where ζ is the damping coefficient. We choose $kT = 1$ and defined a reduced temperature $T^* = 1/\epsilon_{ss}$ to characterize the strength of the association. The drag is with respect to the local solvent velocity with $\boldsymbol{\nabla v}_s = (0,0,0;0,0,0;\dot{\gamma},0,0)$, where $\dot{\gamma}$ is the applied shear rate. In reality, the solvent velocity field will evolve as momentum is exchanged with the solute. The solvent stress (or flow profile) is coupled to the shear stress of the solute through the hydrodynamic drag. As such, our simulations likely provide a conservative estimate for the SCC effects as the assumed solvent drag in the Langevin equation of motion (Eq. (3.1)) acts as a homogenizing force on the polymer flow profile. Simulations are performed using LAMMPS [37].

We equilibrate our samples following the protocol described in the Appendix. The quiescent-state data are collected over a period of $190\tau_R$ (where $\tau_R \approx 1565$ is the Rouse time obtained from the diffusion data of the unassociating chains [38]). Even at the lowest T^*, chains diffuse their own size multiple times. We shear the system

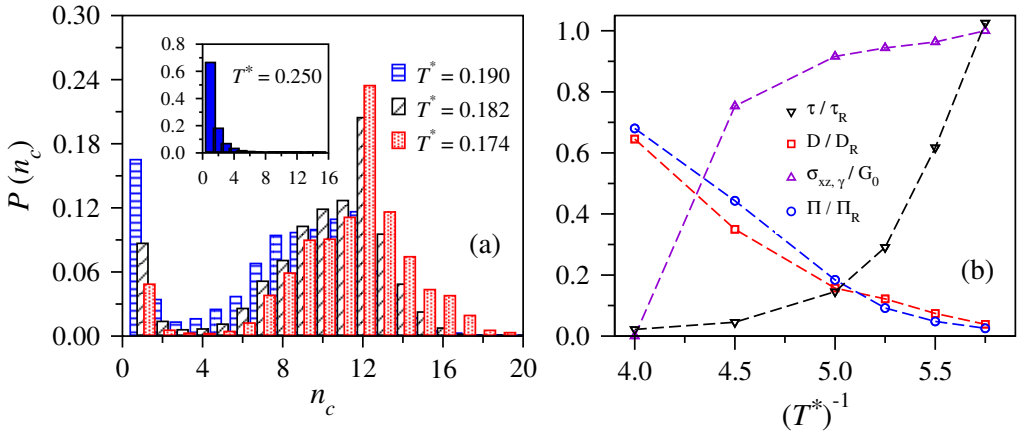

Figure 3.1: Effect of T^* on (a) the weight-averaged cluster size distribution; (b) τ, D, $\sigma_{xz,\gamma}$ and Π. The subscript R indicates properties of our Rouse system with $D_R = 6 \times 10^{-3}$ and $\Pi_R = 8.9nkT$. G_0 is the gel shear modulus at $T^* = 0.174$.

by using two protocols: startup shear at a constant rate for a duration of at least $250\tau_R$ and sweep with several intermediate rates for a duration of $50\tau_R$ per rate. We collect data after an initial transience; the data are averaged over at least four independent samples.

3.2 Equilibrium Properties

To characterize the structure of the gel, we define clusters (groups of two or more associating stickers) based on a connectivity matrix algorithm [39, 40]. Stickers within a cutoff distance of 1.5 (capturing the attractive portion of the LJ potential-well) are deemed associating and grouped into the same cluster. We then compute structural properties such as the network bridge (a polymer strand connecting two clusters) density n_B, the cluster functionality f (the number of bridges per cluster) and the cluster coordination number Z_c (the number of other clusters a cluster is connected to).

We first briefly survey some key quiescent-state properties. At $T^* = 0.25$, there is little sticker aggregation; the majority of stickers remain unpaired (see inset of Fig. 3.1(a)). Upon increasing the association strength to $T^* = 0.20$, the probability distribution of the cluster sizes $P(n_c)$ becomes bimodal, with a second peak emerging at larger cluster sizes. As the average cluster size increases with increasing sticker attraction, the sticker association lifetime τ (the time a sticker spends in a cluster) increases super-exponentially (roughly as $\tau \propto \exp(\langle n_c \rangle / T^*)$), in agreement with the results of Kumar and Douglas [3]. As a result, the chains localize, as seen

through the drop in the long-time self-diffusivity D, shown in Fig. 3.1(b). This "clustering transition" [3] (at $T^* = 0.22 \pm 0.02$) results in the typical rheological properties associated with the gel state. Concurrently, we find dramatic changes in the stress-strain behavior during startup shear: at a rate of $\dot{\gamma} = 10^{-4}$ ($\dot{\gamma}\tau_R < 1$), we find an initial elastic response for the APs ($\sigma_{xz,\gamma} \equiv d\sigma_{xz}/d\gamma|_{\gamma=0} \equiv$ shear modulus and σ_{xz} is the shear stress component of the stress tensor $\boldsymbol{\sigma}$) only for T^*s below this transition.

The clustering of the AP chains results in a reduction of the osmotic pressure, $\Pi = -\text{tr}\boldsymbol{\sigma}/3$, (and hence, osmotic modulus $\partial\Pi/\partial\bar{\rho}$) of the system. AP gels are inherently more compressible than their unassociating counterpart (which are also relatively compressible for $\bar{\rho} \sim \rho^*$). Thus, a salient feature of our AP gels is that while they become *stiffer* with increasing degrees of association in the sense that their shear modulus increases, they also become *softer* in that they are more compressible. This is a natural consequence of the proximity of the sol-gel transition boundary to the spinodal boundary [1, 2].

Steady Shear

We now turn to the steady-state behavior under shear. Starting with an AP system in the gel state, we have examined the steady-state properties for a series of shear rates, in the range of $\dot{\gamma} = 10^{-4} - 10^{-2}$. All shear rates explored are in the nonlinear shear-thinning regime with the Péclet number $\text{Pe} \equiv \dot{\gamma}R_g^2/D > 1$. Even at the lowest shear rate, we observe the formation of shear bands for all T^*s in the gel state. At $T^* = 0.174$, bands are observed up to a shear rate of $\dot{\gamma}^* = 10^{-3}$. Interestingly, the formation of the bands is accompanied by significant concentration differences; see Fig. 3.2(b), where a 3-fold difference in concentration is shown for $T^* = 0.174$ and $\dot{\gamma} = 10^{-4}$. At this rate, the concentrated band is nearly unsheared (with an effective shear rate an order of magnitude smaller than that of the dilute phase) - a direct consequence of both the strong concentration dependence of the viscosity [8, 41] and the shear stress being near the phenomenological yield stress of the band [42, 43]. The significant difference in both density and shear between the bands results in a substantial spatial variation in the network structure (shown through n_B and f).

Upon increasing the rate from $\dot{\gamma} = 10^{-4}$ to $\dot{\gamma} = 5 \times 10^{-4}$, we observe that: (i) the width of the bands remains relatively constant; (ii) the shear stress increases ($\sigma_{xz} - \sigma_Y \propto \dot{\gamma}^{0.75}$ where σ_Y is the material yield stress); (iii) the two bands have exchanged mass so their densities are closer (see Fig. 3.4 for a more quantitative

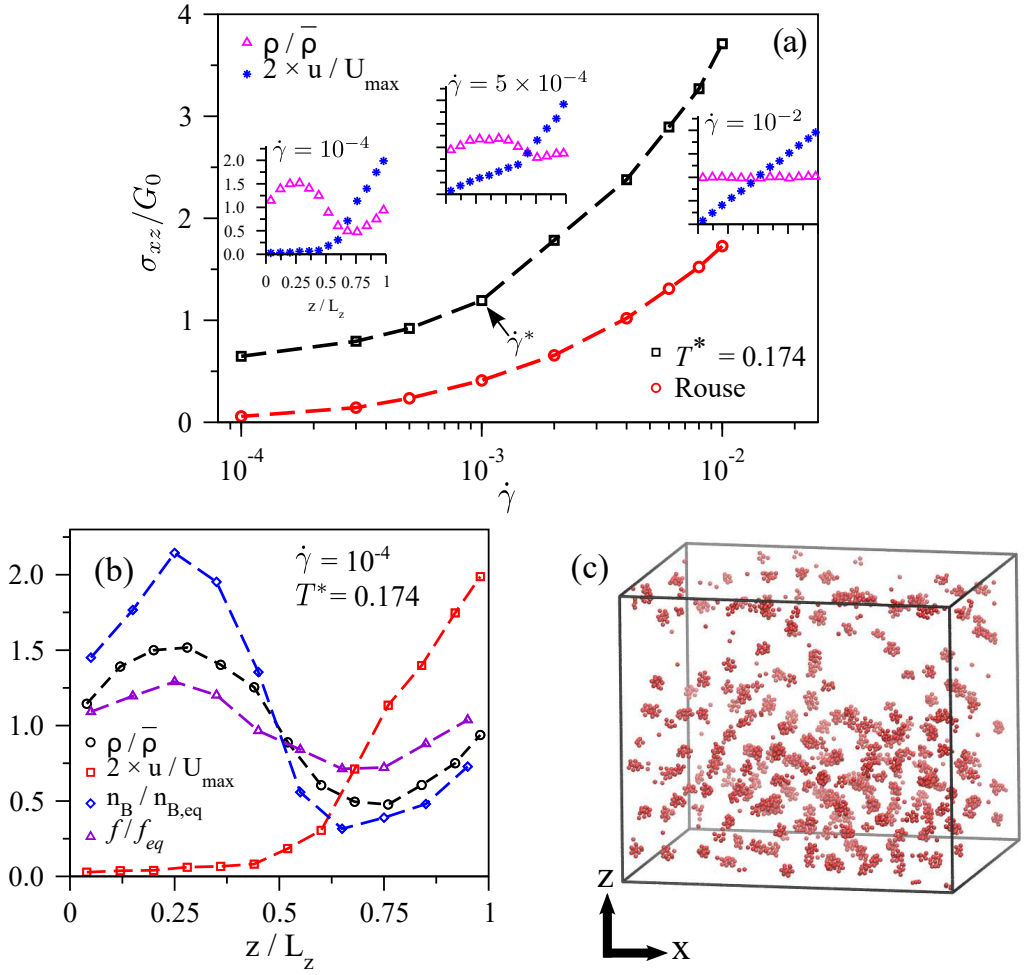

Figure 3.2: (a) Constitutive curves (obtained with a combination of sweep and startup protocols) for gel at $T^* = 0.174$ and for the Rouse solution. The insets display the AP velocity and density profiles at various shear rates. (b) Profiles for concentration ρ, velocity u ($U_{max} = \dot\gamma L_z$), bridging density n_B and cluster functionality f. The subscript eq denotes equilibrium properties. (c) Snapshot of banded flow (only stickers are shown for clarity).

measure through the structure factor); and (iv) both bands are appreciably flowing. These observations are in contrast to the constitutive-instability ($d\sigma_{xz}/d\dot{\gamma} < 0$) mechanism [17] (that has been invoked to explain the recent finding of shear bands in attractive, dense athermal (non-Brownian) particles [44]) wherein the stress and shear rates of the bands remain constant and the width of the bands increases linearly with increasing shear [17, 29]. Rather, these observations are consistent with a flow instability triggered by a strong coupling between shear and concentration [20].

3.3 Shear-Concentration Coupling

Few materials have been shown to exhibit SCC-instabilities in practice [26, 30, 42]. Phenomenologically, previous work derived the following criterion for unstable flow, by linearization of the coupled Navier-Stokes and diffusion equations with respect to density and velocity fluctuations [20, 26, 45]:

$$F(\bar{\rho}, \dot{\gamma}) \equiv \frac{\Pi_{zz,\dot{\gamma}}\sigma_{xz,\bar{\rho}}}{\Pi_{zz,\bar{\rho}}\sigma_{xz,\dot{\gamma}}} > 1, \tag{3.2}$$

where Π_{zz} is the particle pressure in the gradient direction (assuming normal stress differences to be negligible, others (see [25, 26]) have presented eq. (3.2) in terms of the isotropic particle pressure Π rather than the normal pressure in the gradient direction Π_{zz}) and the second subscript denotes a partial derivative with respect to that variable, e.g., $\Pi_{zz,\dot{\gamma}} \equiv \partial\Pi_{zz}/\partial\dot{\gamma}$. The terms $\Pi_{zz,\dot{\gamma}}$ and $\sigma_{xz,\bar{\rho}}$ cause particle migration towards regions of lower shear rate and increased shear in regions of low concentration, respectively. A local increase in particle concentration thus reduces the shear rate, promoting further particle migration. The remaining terms in eq. (3.2) counteract this effect by promoting diffusive spreading of both particles ($\Pi_{zz,\bar{\rho}}$) and momentum ($\sigma_{xz,\dot{\gamma}}$).

While shear thinning and the concentration dependence of the shear stress (reflected, respectively, in $\sigma_{xz,\dot{\gamma}}$ and $\sigma_{xz,\bar{\rho}}$ in eq. (3.2)) have been previously studied [8, 41] and drive the observed large gradient in shear-rate, the influence of shear on the solute pressure Π_{zz} in gels remains unexplored, in part due to the experimental difficulty in measuring this quantity [24]. In Fig. 3.3(a), we show the normalized deviatoric pressure $(\Pi_{zz} - \Pi_{eq})/\Pi_{eq}$ as a function of $\dot{\gamma}$ for AP gels. (For all $\dot{\gamma}$, Π_{zz} is still less than the equilibrium osmotic pressure of our Rouse system (see Fig. 3.5). In increasing the shear rate from $\dot{\gamma} = 10^{-4}$ to $\dot{\gamma} = 10^{-3}$, Π_{zz} exhibits an increase of nearly $2nkT$ for an AP gel at $T^* = 0.174$ in comparison to $0.22nkT$ for a Rouse solution. For our Rouse chains there is only weak SCC, insufficient to result in unstable flow for the examined shear rates. At the lower shear rates, $\Pi_{zz} \sim \Pi_{eq}$ for

the AP gels and thus the gels are nearly as compressible as in the quiescent state. This region of shear rates where the gels are highly compressible, coupled with a strong variation in Π_{zz} with $\dot{\gamma}$, is precisely where we observe a significant, sustained concentration (and shear rate) difference.

The large increase in Π_{zz} with shear in our AP gels contrasts with the known dilation [46] response of comparably dilute systems. Simulations of colloidal hard spheres at volume fractions of 10% show a pressure increase of only nkT over four decades of applied shear rate [27]. For polymer solutions, the reduction in the chain dimension in the gradient direction with shear increases Π_{zz} due to the chain elasticity. For the $\dot{\gamma}$ examined, we find no significant compression of the AP chain conformation in the gradient direction; the degree of compression is even less than our Rouse system (see Fig. 3.6), which only results in modest increases in Π_{zz} with $\dot{\gamma}$. Therefore, while a contributing factor, the coupling of chain elasticity to shear does not appear to be the source of the observed SCC.

3.4 Network Dilation and Shear-Induced Diffusion

What, then, is the origin of the observed dilation? To explore this question, we focus on the structural evolution of the gel at shear rates for which the flow is homogeneous ($\dot{\gamma} > \dot{\gamma}^*$). Crucially, in this regime the density is homogeneous, allowing us to delineate the role of shear alone on the structural properties of the gel. Examination of the sticker cluster size distribution $P(n_c)$ shows a shift towards smaller aggregation with increasing $\dot{\gamma}$ (Fig. 3.3(b)). From our quiescent-state analysis (cf. Fig. 3.1) we indeed found the pressure to increase with decreasing degree of association. However, while $P(n_c)$ appears more sensitive to T^* than $\dot{\gamma}$, raising T^* from 0.174 to 0.190 only increases the pressure by $\approx 0.6nkT$ (see Fig. 3.1(b)), an order of magnitude less than the pressure increases under shear. The failure to explain the significant increase in Π_{zz} with shear by introducing an effective gel temperature, suggests that the gel undergoes significant structural changes unaccounted for by shifts in $P(n_c)$.

Under steady shear, one would intuitively expect that large aggregates of connected clusters extending in the gradient direction will be subject to large elastic stresses, giving way to structural breakup. To quantify these large-scale aggregates, we extend our sticker connectivity methodology to explore the connectivity of the clusters themselves into supramolecular aggregates. Clusters that are connected by at least one polymer strand are deemed to belong to the same aggregate.

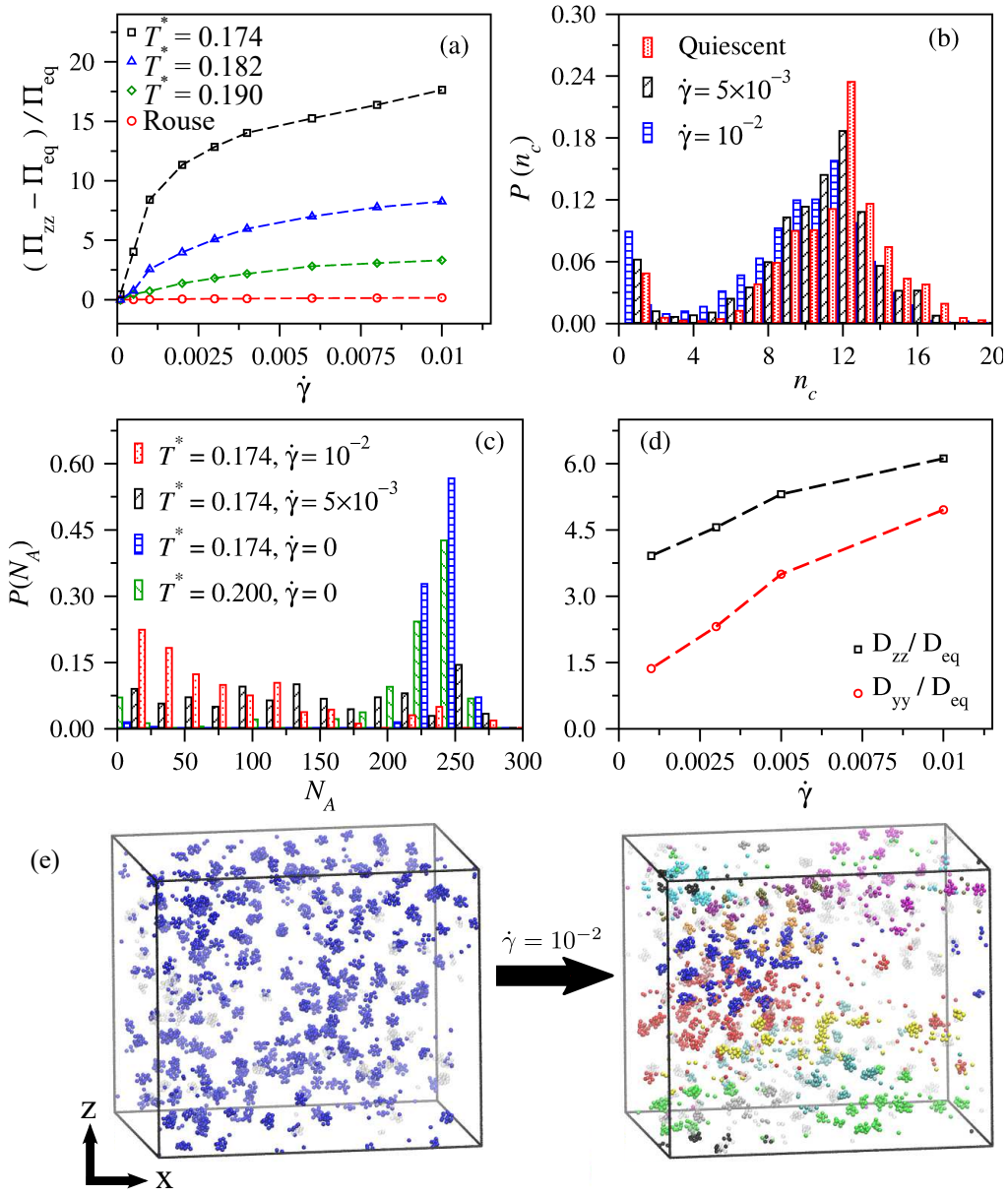

Figure 3.3: (a) $(\Pi_{zz} - \Pi_{eq})/\Pi_{eq}$ as a function of $\dot{\gamma}$ and T^*. (b) Influence of $\dot{\gamma}$ on the cluster size distribution of the AP gel ($T^* = 0.174$). (c) Weight-averaged DRA size distribution (with the chains binned into groups of 20) excluding clusters with $Z_c < 4$. (d) Diffusivity in the gradient D_{zz} and vorticity D_{yy} directions in the regime of homogeneous flow. (e) Breakup of a single space-spanning DRA at equilibrium (left) to several smaller DRAs (indicated by different colors) during steady shear at $\dot{\gamma} = 10^{-2}$ (right). Stickers not belonging to a DRA are shown in gray.

In quiescence, all of the gels explored have a single supramolecular aggregate that contains nearly all of the chains. Interestingly, even at the largest $\dot{\gamma}$, a gel at any given moment remains a space-spanning network (Fig. 3.7). However, some of the connections within the network are weak and undergo rapid breaking and reforming. The weakly connected regions are typically bound together by low coordination (Z_c) clusters. We therefore define a dynamically robust aggregate (DRA) to consist of clusters with $Z_c \geq 4$ (4 being the median of Z_c at equilibrium). The size distribution of the DRAs exhibit a striking qualitative change with shear as shown in Fig. 3.3(c). At or near equilibrium (i.e., in the linear-response regime) with Pe $\lesssim 1$, a system-spanning aggregate containing nearly all of the chains dominates the distribution, a feature that is general to APs in the gel state (the blue and green bars). Under high shear (the red and black bars) with $\dot{\gamma} > \dot{\gamma}^*$ and Pe $\gg 1$, the distribution becomes significantly broader, shifting towards smaller aggregate sizes with increasing $\dot{\gamma}$ (see Fig. 3.3(e) for a snapshot of the network structure under shear). The transition between these disparate distributions is precisely the flow regime (Pe > 1 and $\dot{\gamma} < \dot{\gamma}^*$) where we observe the SCC-instability and the significant dilatancy.

We emphasize that the difference between these distributions (e.g., see the red and green bars) is not simply a result of reduced coordination under shear, as the average coordination of the $T^* = 0.174$ gel at $\dot{\gamma} = 10^{-2}$ ($\langle Z_c \rangle = 3.4$) is larger than that of the $T^* = 0.200$ gel at rest ($\langle Z_c \rangle = 3.2$). Rather, this indicates that shear induces spatial *heterogeneity* in the network connectivity. This shear-induced heterogeneity in the network structure enhances the chain diffusivity in the gradient (and vorticity) direction (see Fig. 3.3(d)). This enhanced mobility in the gradient direction, in turn, causes Π_{zz} to increase with $\dot{\gamma}$. The strong increase of Π_{zz} with $\dot{\gamma}$ at the lower shear rates, coupled with the inherently low osmotic modulus, can destabilize homogeneous flow via an SCC-instability (see eq. (3.2)), generating shear bands with significant dynamic and structural differences . At the low shear end of the unstable region ($\dot{\gamma} \ll \dot{\gamma}^*$ and Pe > 1), the low shear stress coupled with significant growth in density heterogeneity can result in the yield stress of the high-density band approaching the system shear stress, further sharpening the differences in shear (and hence density) between the bands.

3.5 Conclusions

In probing the mechanism of SCC in AP gels we highlight the crucial role of the mesoscale network connectivity – rather than such global measures as the degree of association – in the observed unique rheological behavior. We hope this work

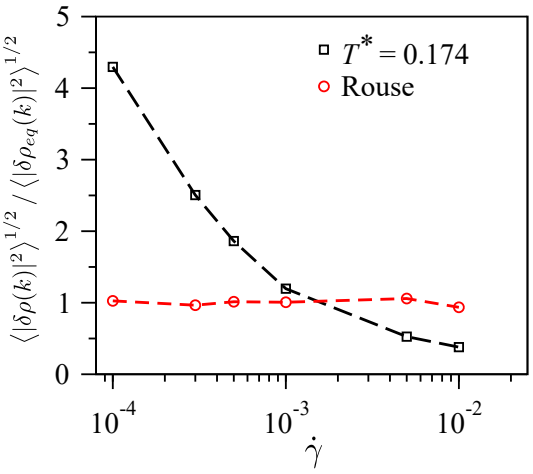

Figure 3.4: Magnitude of the density heterogeneity at $k = 2\pi/L_z$ for an AP at $T^* = 0.174$ and for the Rouse solution. The subscript eq denotes equilibrium properties.

can inform the development of constitutive laws for the full AP stress tensor to allow for a more complete description of AP rheology. Network topology should play a similarly important role in determining the mechanical (beyond elasticity) and dynamical properties of AP solutions and gels at equilibrium. We leave the theoretical elucidation of this role to future work.

3.6 Appendix

Equilibration. To reach the equilibrium state, for each ϵ_{ss} the sample is annealed at a reduced temperature $T^* = 1$ for a duration of $12\tau_R$, followed by quenching to $T^* = 1/\epsilon_{ss}$ over a period of $20\tau_R$. We then further equilibrate each sample for $95\tau_R$. The quiescent-state data (e.g., the osmotic pressure, diffusivity and structural properties) are collected over a period of $190\tau_R$.

Methods. We compute stress using the well-known Irving-Kirkwood expression $\boldsymbol{\sigma} = -\rho\left\langle \boldsymbol{r}'\boldsymbol{r}'\right\rangle - \rho\left\langle \boldsymbol{r}\boldsymbol{f}_p\right\rangle$ where $\langle\cdots\rangle$ denotes an average over all beads and $\boldsymbol{r}' = \boldsymbol{r} - \boldsymbol{r}\cdot\boldsymbol{\nabla}\boldsymbol{v}_s$ represents velocity fluctuations (recall $m = 1$; the first term in the stress tensor simply results in $-\rho kT$). The particle (or osmotic) pressure is $\Pi = -\mathrm{tr}\boldsymbol{\sigma}/3$. The long-time self-diffusivity is measured from the chain center-of-mass mean-square-displacement $D = \lim_{t\to\infty}\frac{1}{6}D\left\langle(\Delta\boldsymbol{r}_{cm})^2\right\rangle/dt$. In presenting spatial profiles (see Fig. 2 in the main text), we shift the particles from each sample such that the concentrated band is at the bottom of the simulation box.

Structure Factor. To compute the magnitude of the density heterogeneity, we bin the simulation box in the gradient direction into 10 layers ($i = 1, 2, \ldots, 10$) of equal

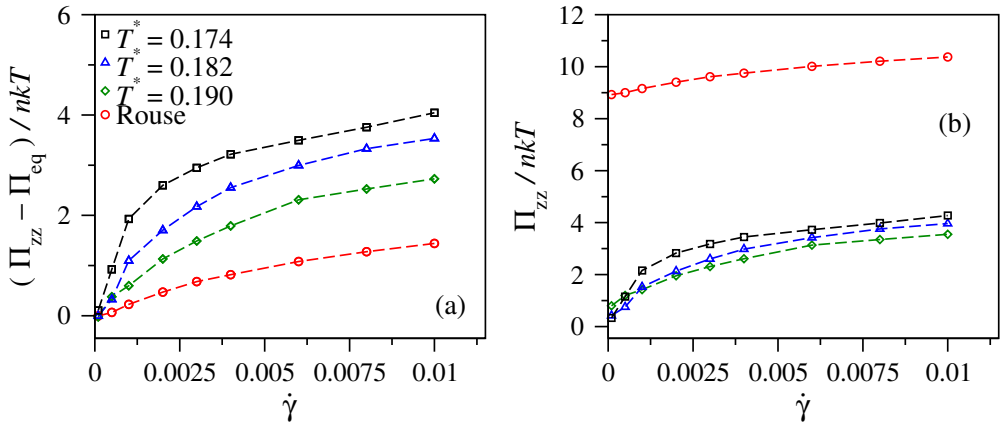

Figure 3.5: (a) $(\Pi_{zz} - \Pi_{eq})/nkT$ and (b) Π_{zz}/nkT as a function of $\dot{\gamma}$ for gels of various T^* and Rouse system.

thickness and compute $\delta\rho(z_j) = \rho(z_j) - \bar{\rho}$. We then take a discrete spatial Fourier transform $\delta\rho(k) = \frac{1}{10}\sum_{j=1}^{10}\delta\rho(z_j)e^{ikz_j}$, reporting the ensemble (time and sample) averaged $\left\langle|\delta\rho(k)|^2\right\rangle = \langle\delta\rho(k)\delta\rho(-k)\rangle$. We use the density profiles obtained over the last $60\tau_R$ of shear (where little transience is observed) in computing $\delta\rho(z_j)$. The resulting coarse-grained structure factors (for both the Rouse solution and AP at $T^* = 0.174$) as a function of shear are shown in Fig. 3.4.

In our system, as we approach the unstable region (from higher shear rates) we find significant increases in the long wavelength ($k = 2\pi/L_z$) value of the structure factor: the magnitude of the density heterogeneity is greatly enhanced (relative to equilibrium) for $\dot{\gamma} < \dot{\gamma}^*$ and is suppressed for $\dot{\gamma} > \dot{\gamma}^*$.

Pressure. In the main text (see Fig. 3(a)), we show the deviatoric polymer pressure as a function of T^* and $\dot{\gamma}$ normalized by the equilibrium osmotic pressure Π_{eq} at the given T^*, in order to highlight the variation with respect to the quiescent-state value. Here, we normalize the deviatoric pressure by nkT to show the actual value in the pressure variation with shear. We also provide the actual values of the pressure itself in Fig. 3.5(b). As noted in the main text, at low $\dot{\gamma}$, the degree of dilation for AP gels can be significantly larger than for a Rouse solution, with APs at lower T^* exhibiting the largest pressure increases. While only the initial rapid variations in Π_{zz} with $\dot{\gamma}$ are relevant in the context of SCC (see main text), we note that Π_{zz} for all AP gels at a given $\dot{\gamma}$ are quite comparable.

Chain Conformation. To characterize the role of chain elasticity in stress generation we compute the radius of gyration $R_g^2 = \frac{1}{N}\sum_{i=1}^{N}(\boldsymbol{r}_i - \boldsymbol{r}_{cm})^2$ for each chain and report

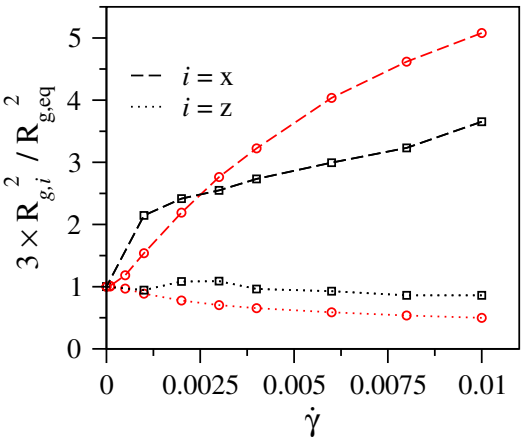

Figure 3.6: The relative degree of chain extension in the flow (x) and gradient (z) directions for AP gel at $T^* = 0.174$ (□) and the Rouse solution (○) for $\dot{\gamma}$ in which the flow is homogeneous.

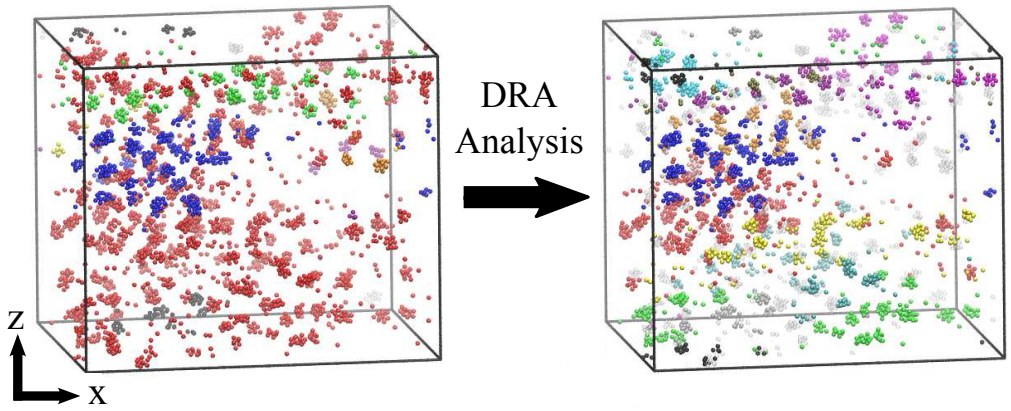

Figure 3.7: Trimming of the AP gel network at $T^* = 0.174$ and $\dot{\gamma} = 10^{-2}$ with the DRA analysis.

the average over all chains as a function of $\dot{\gamma}$ (for homogeneous flow) in Fig. 3.6. As noted in the main text, R_g for the AP chains in the z direction is less compressed than the corresponding Rouse system for all the $\dot{\gamma}$ explored. We note that at moderate shear rates the AP chains actually expand slightly, a direct consequence of the reduction of intramolecular association. While AP gels have a larger stress than the Rouse solution for all $\dot{\gamma}$, the relative AP chain extension in the x direction can be less than that of the Rouse solution. This observation suggests interesting behavior in the force-extension curve of APs.

Connectivity. Figure 3.7 contrasts the aggregates defined without and with applying the connectivity criteria (DRA) used in the main text. Even at the largest shear rates

of $\dot{\gamma} = 10^{-2}$, including low-coordination clusters in defining aggregates results in a majority of the chains being included within a single space-spanning structure. Upon defining the DRAs, the space-spanning aggregate is broken up into several smaller aggregates.

References

[1] Semenov, A. N.; Rubinstein, M. Thermoreversible Gelation in Solutions of Associative Polymers. 1. Statics. *Macromolecules* **1998**, *31*, 1373–1385.

[2] Kumar, S. K.; Panagiotopoulos, A. Z. Thermodynamics of Reversibly Associating Polymer Solutions. *Phys. Rev. Lett.* **1999**, *82*, 5060–5063.

[3] Kumar, S. K.; Douglas, J. F. Gelation in Physically Associating Polymer Solutions. *Phys. Rev. Lett.* **2001**, *87*, 188301.

[4] Storm, C.; Pastore, J. J.; Mackintosh, F. C.; Lubensky, T. C.; Janmey, P. A. Nonlinear Elasticity in Biological Gels. *Nature* **2005**, *435*, 191–194.

[5] Janmey, P. A.; McCormick, M. E.; Rammensee, S.; Leight, J. L.; Georges, P. C.; Mackintosh, F. C. Negative Normal Stress in Semiflexible Biopolymer Gels. *Nat. Mater.* **2006**, *6*, 48–51.

[6] Suzuki, S.; Uneyama, T.; Inoue, T.; Watanabe, H. Nonlinear Rheology of Telechelic Associative Polymer Networks: Shear Thickening and Thinning Behavior of Hydrophobically Modified Ethoxylated Urethane (HEUR) in Aqueous Solution. *Macromolecules* **2012**, *45*, 888–898.

[7] Ianniruberto, G.; Marrucci, G. New Interpretation of Shear Thickening in Telechelic Associating Polymers. *Macromolecules* **2015**, *48*, 5439–5449.

[8] Annable, T.; Buscall, R.; Ettelaie, R.; Whittlestone, D. The Rheology of Solutions of Associating Polymers: Comparison of Experimental Behavior with Transient Network Theory. *J. Rheol.* **1993**, *37*, 695.

[9] Billen, J.; Wilson, M.; Baljon, A. R. Shear Banding in Simulated Telechelic Polymers. *Chem. Phys.* **2015**, *446*, 7–12.

[10] Erk, K. A.; Shull, K. R. Rate-dependent Stiffening and Strain Localization in Physically Associating Solutions. *Macromolecules* **2011**, *44*, 932–939.

[11] Erk, K. A.; Martin, J. D.; Hu, Y. T.; Shull, K. R. Extreme Strain Localization and Sliding Friction in Physically Associating Polymer Gels. *Langmuir* **2012**, *28*, 4472–4478.

[12] Thornell, T. L.; Helfrecht, B. A.; Mullen, S. A.; Bawiskar, A.; Erk, K. A. Fracture-healing Kinetics of Thermoreversible Physical Gels Quantified by Shear Rheophysical Experiments. *ACS Macro Lett.* **2014**, *3*, 1069–1073.

[13] Sprakel, J.; Spruijt, E.; Cohen Stuart, M. A.; Besseling, N. A. M.; Lettinga, M. P.; Van Der Gucht, J. Shear Banding and Rheochaos in Associative Polymer Networks. *Soft Matter* **2008**, *4*, 1696.

[14] Sprakel, J.; Spruijt, E.; Van Der Gucht, J.; Padding, J. T.; Briels, W. J. Failure-mode Transition in Transient Polymer Networks with Particle-based Simulations. *Soft Matter* **2009**, *5*, 4748.

[15] Castillo-Tejas, J.; Carro, S.; Manero, O. Shear Banding in Telechelic Associative Polymers by Molecular Dynamics. *ACS Macro Lett.* **2017**, *6*, 190–193.

[16] Colombo, J.; Del Gado, E. Stress Localization, Stiffening, and Yielding in a Model Colloidal Gel. *J. Rheol.* **2014**, *58*, 1089–1116.

[17] Dhont, J. K. G.; Briels, W. J. Gradient and Vorticity Banding. *Rheol. Acta* **2008**, *47*, 257–281.

[18] Fielding, S. M. Shear Banding in Soft Glassy Materials. *Rep. Prog. Phys.* **2014**, *77*, 102601.

[19] Nozières, P.; Quemada, D. A Possible Instability Mechanism for Plug Formation in a Sheared Suspension Flow. *Europhys. Lett.* **1986**, *2*, 129–135.

[20] Schmitt, V.; Marques, C. M.; Lequeux, F. Shear-induced Phase Separation of Complex Fluids: The Role of Flow-concentration Coupling. *Phys. Rev. E* **1995**, *52*, 4009–4015.

[21] Tanaka, F.; Edwards, S. F. Viscoelastic Properties of Physically Cross-linked Networks - Transient Network Theory. *Macromolecules* **1992**, *25*, 1516–1523.

[22] Tripathi, A.; Tam, K. C.; McKinley, G. H. Rheology and Dynamics of Associative Polymers in Shear and Extension: Theory and Experiments. *Macromolecules* **2006**, *39*, 1981–1999.

[23] Sing, M. K.; Wang, Z.-g.; McKinley, G. H.; Olsen, B. D. Chain Configuration and Rate-dependent Mechanical Properties in Transient Networks. *Soft Matter* **2015**, *11*, 2085–2096.

[24] Deboeuf, A.; Gauthier, G.; Martin, J.; Yurkovetsky, Y.; Morris, J. F. Particle Pressure in a Sheared Suspension: A Bridge from Osmosis to Granular Dilatancy. *Phys. Rev. Lett.* **2009**, *102*.

[25] Nott, P. R.; Brady, J. F. Pressure-driven Flow of Suspensions: Simulation and Theory. *J. Fluid Mech.* **1994**, *275*, 157.

[26] Besseling, R.; Isa, L.; Ballesta, P.; Petekidis, G.; Cates, M. E.; Poon, W. C. K. Shear Banding and Flow-concentration Coupling in Colloidal Glasses. *Phys. Rev. Lett.* **2010**, *105*.

[27] Yurkovetsky, Y.; Morris, J. F. Particle Pressure in Sheared Brownian Suspensions. *J. Rheol.* **2008**, *52*, 141.

[28] Cromer, M.; Villet, M. C.; Fredrickson, G. H.; Leal, L. G. Shear Banding in Polymer Solutions. *Phys. Fluids* **2013**, *25*, 051703.

[29] Fielding, S.; Olmsted, P. Flow Phase Diagrams for Concentration-coupled Shear Banding. *Euro. Phys. J. E* **2003**, *11*, 65–83.

[30] Helgeson, M. E.; Porcar, L.; Lopez-Barron, C.; Wagner, N. J. Direct Observation of Flow-concentration Coupling in a Shear-banding Fluid. *Phys. Rev. Lett.* **2010**, *105*.

[31] Helfand, E.; Fredrickson, G. Large Fluctuations in Polymer Solutions under Shear. *Phys. Rev. Lett.* **1989**, *62*, 2468–2471.

[32] Wu, X.-l.; Pine, D. J.; Dixon, P. K. Enhanced Concentration Fluctuations in Polymer Solutions under Shear Flow. *Phys. Rev. Lett.* **1991**, *66*, 2408–2411.

[33] Milner, S. T. Hydrodynamics of Semidilute Polymer Solutions. *Phys. Rev. Lett.* **1991**, *66*, 1477–1480.

[34] Kremer, K.; Grest, G. S. Dynamics of Entangled Linear Polymer Melts: A Molecular-dynamics Simulation. *J. Chem. Phys.* **1990**, *92*, 5057.

[35] Weeks, J. D.; Chandler, D.; Andersen, H. C. Role of Repulsive Forces in Determining the Equilibrium Structure of Simple Liquids. *J. Chem. Phys.* **1971**, *54*, 5237–5247.

[36] Lees, A. W.; Edwards, S. F. The Computer Study of Transport Processes under Extreme Conditions. *J. Phys. C* **1972**, *5*, 1921–1928.

[37] Plimpton, S. Fast Parallel Algorithms for Short-range Molecular Dynamics. *J. Comput. Phys.* **1995**, *117*, 1–19.

[38] Doi, M.; Edwards, S. F. *The Theory of Polymer Dynamics*; Oxford University Press, 1986.

[39] Sevick, E. M.; Monson, P. A.; Ottino, J. M. Monte Carlo Calculations of Cluster Statistics in Continuum Models of Composite Morphology. *J. Chem. Phys.* **1988**, *88*, 1198–1206.

[40] Surve, M.; Pryamitsyn, V.; Ganesan, V. Universality in Structure and Elasticity of Polymer-nanoparticle Gels. *Phys. Rev. Lett.* **2006**, *96*.

[41] Rubinstein, M.; Semenov, A. N. Thermoreversible Gelation in Solutions of Associating Polymers. 2. Linear Dynamics. *Macromolecules* **1998**, *31*, 1386–1397.

[42] Jin, H.; Kang, K.; Ahn, K. H.; Dhont, J. K. G. Flow Instability Due to Coupling of Shear-gradients with Concentration: Non-uniform Flow of (hard-sphere) Glasses. *Soft Matter* **2014**, *10*, 9470–9485.

[43] Møller, P. C. F.; Rodts, S.; Michels, M. A. J.; Bonn, D. Shear Banding and Yield Stress in Soft Glassy Materials. *Phys. Rev. E* **2008**, *77*, 041507.

[44] Irani, E.; Chaudhuri, P.; Heussinger, C. Impact of Attractive Interactions on the Rheology of Dense Athermal Particles. *Phys. Rev. Lett.* **2014**, *112*.

[45] Cromer, M.; Fredrickson, G. H.; Leal, L. G. A Study of Shear Banding in Polymer Solutions. *Phys. Fluids* **2014**, *26*, 063101.

[46] Ferry, J. D. *Viscoelastic Properties of Polymers*; Wiley, New York, 1980.

Chapter 4

SWIMMING TO STABILITY: STRUCTURAL AND DYNAMICAL CONTROL OF A COLLOIDAL GEL VIA ACTIVE DOPING

External fields can decidedly alter the free energy landscape of soft materials and can be exploited as a powerful tool for the assembly of targeted nanostructures and colloidal materials. Here, we use computer simulations to demonstrate that nonequilibrium *internal fields* or forces – forces that are generated by driven components within a system – in the form of active particles can precisely modulate the dynamical free energy landscape of a model soft material, a colloidal gel. Embedding a small fraction of active particles within a gel can provide a unique pathway for the dynamically frustrated network to circumvent the kinetic barriers associated with reaching a lower free energy state through thermal fluctuations alone. Moreover, by carefully tuning the active particle properties (the propulsive swim force and persistence length) in comparison to those of the gel, the active particles may induce depletion-like forces between the constituent particles of the gel despite there being *no geometric size asymmetry* between the particles. These resulting forces can rapidly push the system toward disparate regions of phase space. Intriguingly, the state of the material can be altered by tuning macroscopic transport properties such as the solvent viscosity. Our findings highlight the potential wide-ranging structural and kinetic control facilitated by varying the dynamical properties of a remarkably small fraction of driven particles embedded in a host material.

This chapter includes content from our previously published article:

Omar, A. K.; Wu, Y.; Wang, Z.-G.; Brady, J. F. Swimming to Stability: Structural and Dynamical Control via Active Doping. *ACS Nano* **2019**, *13*, 560–572. DOI:10.1021/acsnano.8b07421

4.1 Introduction

Advances in materials chemistry have opened new and exciting vistas for designing colloidal and nanoparticle building blocks, resulting in materials endowed with unique structures and accompanying properties [1–4]. Particle shape [5, 6] and surface chemistry (e.g., decorating the particle surface with sticky "patches" [7, 8] of organic or biological molecules [9–11]) allow for exquisite control of the directionality of particle interactions, unlocking a multitude of structures with wide-ranging symmetries. The attractive particle interactions that are often used to stabilize these structures may also introduce a free energy landscape replete with barriers associated with particle rearrangement which can significantly delay or even preclude reaching the globally stable configuration. Indeed, the traditional pathways for homogeneous suspensions of particles to phase separate into dilute and dense phases, including spinodal decomposition and nucleation, can be exceedingly long and in practice can be the limiting factor in the experimental observation of ordered colloidal and nanoparticle-based materials [12, 13].

The classical system that demonstrates this issue of kinetic frustration is perhaps also the simplest: a colloidal suspension of spheres with short-range isotropic attractive interactions. While the equilibrium phase diagram of this system predicts fluid-solid coexistence for interaction strengths as little as a few times the thermal energy k_BT, in practice the system is found to form a long-lived space-spanning network, a gel, for nearly the entire coexistence region [14]. This gel state is argued to be a result of the glassy dynamics of the solid phase which hinders the diffusion and coalescence of the bicontinuous dense strands formed during spinodal decomposition [14]. Even upon reducing the isotropic attraction to discrete sticky sites, it can take years for a colloidal system to complete the phase separation process [15].

Nonequilibrium protocols provide an opportunity to overcome the naturally occurring kinetic barriers. A classic approach is simple thermal annealing; temporally controlling the presence of potential energy barriers by modulating the system temperature can allow for particles to search for stable configurations before the barriers have fully set in. Recently, Swan and co-workers explored temporally varying the interaction potential (e.g., for systems in which the interaction energy can be modulated with an external field) and found improved colloidal crystallization rates by periodically "toggling" the interactions off and on [16–20]. Applied shear or stress has also been examined as a means by which to reduce kinetic barriers by allowing dense or yield-stress materials to "fluidize" or yield [21, 22]. Indeed,

simulations of colloidal gels in a variety of deformation protocols have revealed an increase in the rate of gel coarsening or phase separated-like states at certain applied rates/stresses [23–26]. In practice, however, while deformation-induced structures may resemble the target structure, deformation protocols naturally break rotational symmetry which could be an essential feature of the target structure. Indeed, the development of protocols that truly preserve the underlying (equilibrium) globally stable configuration while providing a viable kinetic pathway to this configuration is a difficult balance and remains an outstanding challenge in colloidal and materials science.

The above examples involve the application of *external* fields to circumvent kinetic barriers. Broadly, these protocols act to inject the necessary free energy (through the system boundary) to either traverse the existing barriers or create entirely new pathways for phase separation. However, these free energy injections need not come from an external source. The recent focus on so-called active particles [27–29] – particles that self-propel or "swim" through the conversion of chemical energy – motivates the idea of doping a material with a small fraction of such particles which can act as *internal* sources of free energy that can locally drive a material over kinetic hurdles. A complementary mechanical viewpoint is that active particles - just as shear and other deformation protocols – can act as a source of stress by virtue of their unique "swim pressure" [30–32] which, on the colloidal scale, can be the dominant source of stress.

4.2 Active Matter for Colloidal Stability

The use of active particles in material design has previously been explored; however most of these studies have focused on suspensions in which *all* particles are active [33–36]. To date, a few studies have sought to characterize the influence of a small fraction of active particles on the dynamical and structural landscape of the host material [37]. These studies have revealed intriguing results: simulations [38] have shown that embedding a hard-sphere glass with active particles can improve crystallization rates while experiments on slightly more dilute hard-sphere systems demonstrated that active particles improve the coalescence of large passive grains. Other studies that have explored mixtures of active and "passive" particles [39, 40] have largely focused on regimes in which passive particles perturb the underlying properties/behavior of the active particles (such as motility-induced phase separation or MIPS [41]), the inverse problem to the active doping idea explored here.

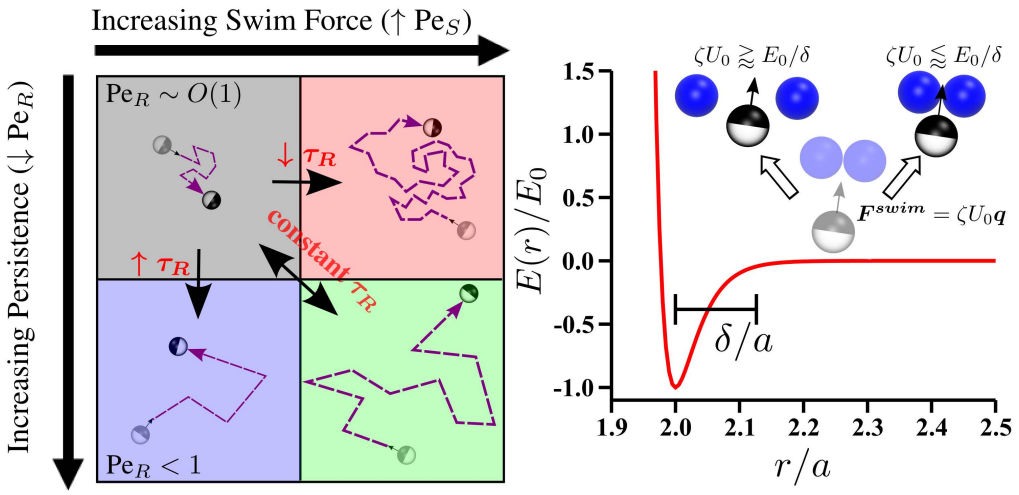

Figure 4.1: Physical schematic (left) of the key parameters characterizing active particle motion: persistence and swim force quantified by Pe_R and Pe_S, respectively. The sketched swimmers have the same size and Brownian diffusivity and only differ in the underlying microscopic swimming dynamics. Variation in the spatial extent of the trajectories is intended to highlight contrasts in the swim diffusivity, while increased thickness of the trajectory-lines reflects larger swim speeds/forces. Schematic (right) of the pivotal role that the swim force plays in materials with attractive interactions. The potential energy displayed is the Morse potential that is utilized in our simulations.

A primary appeal in the use of active dopants is the extraordinary range of swimmers (and properties) that can be exploited. These active particles can be living microscopic organisms such as bacteria or synthetic microswimmers such as catalytic Janus particles. While the mechanism for swimming can be highly variable among swimmers, there are two salient characteristics inherent to all active particles that have proven sufficient in capturing a broad range of properties: (i) the propulsive swim force $\boldsymbol{F}^{\boldsymbol{swim}}$ of magnitude ζU_0 and direction $\boldsymbol{q}$, which is the force required to overcome the hydrodynamic resistance to swimming at a speed U_0 with a drag coefficient of ζ and (ii) the characteristic reorientation time τ_R for an active particle to change its swimming direction $\boldsymbol{q}$. The reorientation dynamics of active particles give rise to a persistence length $l_p = U_0\tau_R$ – the characteristic distance that a particle travels before reorienting – and, at long times, a swim diffusivity given by $D^{swim} \sim l_p^2/\tau_R = U_0^2\tau_R$ [42].

The strength of advective swimming relative to Brownian diffusion for a particle of size a is given by the swim Péclet number $\mathrm{Pe}_S = \zeta U_0 a/k_BT$, which can be equivalently thought of as the ratio of the swim force to the characteristic thermal force $\mathrm{Pe}_S = F^{swim}/F^{thermal} = \zeta U_0/(k_BT/a)$. We can also define a Péclet number

based on the swim diffusivity as $\mathrm{Pe}_R = U_0 a / U_0^2 \tau_R = a/l_p$.(We use the conventional definition of the Péclet number as advection over diffusion in defining Pe_R, but others may use the inverse of this quantity.) This reorientation Péclet number provides a nondimensional measure of the persistence length of the swimmers' motion. Figure 4.1 provides a physical illustration of the influence of Pe_S and Pe_R on the microscopic swimming dynamics. We emphasize that active particles with identical long-time properties, such as the swim diffusivity, can have vastly different microscopic dynamics.

Our goal in this work is to use computer simulation to establish generic "design rules" for the use of active dopants to catalyze material assembly, that is, to establish how the dynamic properties of active dopants ($\mathrm{Pe}_S, \mathrm{Pe}_R$) in relation to the properties of the "host" material alter the dynamic free energy landscape of the material. To this end, we choose the simplest colloidal system that displays kinetic frustration as our host material: a suspension of polydisperse sticky particles. For this system, the globally stable configuration is macroscopic phase separation (within the two phase boundary) with coexistence between a dilute gas of particles and a dense (glassy) liquid. However, as previously discussed, macroscopic phase separation is kinetically prohibitive and in practice, a slowly coarsening gel is observed in both experiment and simulation [14, 43]. The clarity in the underlying free energy landscape of this material is precisely what allows us to readily identify the alterations made by active dopants.

The remainder of this chapter is organized as follows. First, we use simulation to explore activity space ($\mathrm{Pe}_S, \mathrm{Pe}_R$) and phenomenologically describe the influence of the swimmers. We find remarkably distinct regions in activity space wherein active particles enhance both phase separation kinetics and mediate effective interactions between the passive particles that can be either repulsive or attractive. This regime in which activity modifies the underlying globally stable configuration is clearly separated from a regime in which active particles only provide a length-scale-dependent kinetic enhancement to the coarsening dynamics. We then explore the origins of these regimes and conclude with a discussion on the implication of our results for the use of active dopants for material assembly.

Results and Discussion

Model System. We consider a system consisting of passive particles of average radius a with a polydispersity of 5% and monodisperse active particles of radius

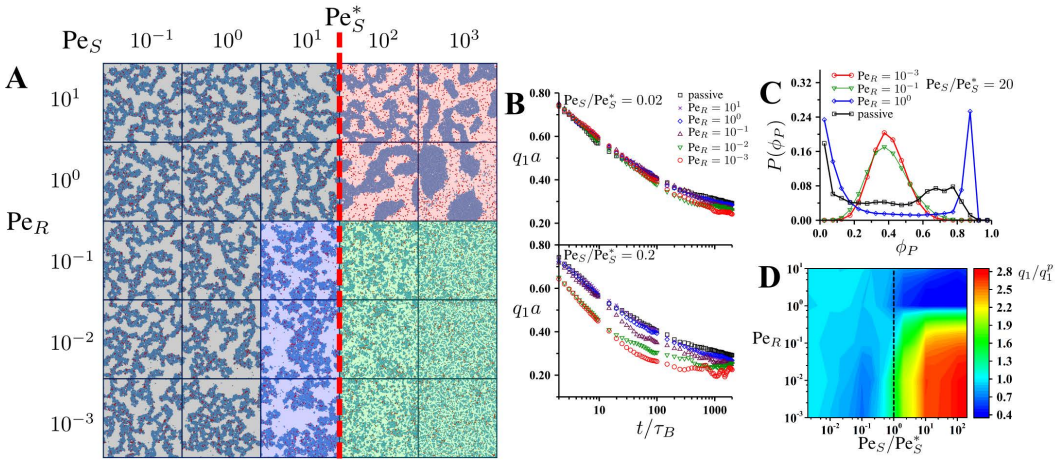

Figure 4.2: (A) Representative snapshots of system configurations with like-shaded snapshots representing groupings between dynamically or structurally similar regions in $\mathrm{Pe}_R - \mathrm{Pe}_S$ space. Active particles are shown in red. (B) Dynamic evolution of q_1 as a function of persistence as $\mathrm{Pe}_S \rightarrow \mathrm{Pe}_S^*$. (C) Area fraction distribution (obtained by equally dividing the system area into square subareas and computing the local area fraction in each region) as a function of persistence. (D) Dominant (inverse) length scale in the system (q_1) as a function of Pe_S and Pe_R with interpolation/smoothing applied between 55 discrete points to achieve a continuous representation.

a. We primarily focus on two-dimensional systems but selectively perform three dimensional simulations to highlight the generality of our results. The passive particles occupy an area fraction of $\phi_P = 0.4$ while the active area fraction is set to one-tenth of that of the passive particles $\phi_A = 0.04$. All particles undergo translational Brownian diffusion characterized by a self-diffusion time $\tau_B = a^2\zeta/k_BT$. Further, all particles (including the swimmers) interact with the short-ranged attractive potential shown in Fig. 4.1 where the well depth is set to $E_0 = 6k_BT$ and the interaction range is $\delta \approx 0.12a$. Note that the active particle interactions need not be the same as those of the passive particles; they are, in principle, entirely independent if the interactions are generated by surface chemistries but will be identical if interactions are due to entropic or geometric effects, such as depletion induced by polymers. Simulations are initialized with random configurations and, unless otherwise noted, are run for a duration of $2000\tau_B$ with the total number of particles ranging from 3300 to 33000 (see the Appendix for details).

As our primary aim is to elucidate the role of activity, we hold all parameters (E_0, δ, ϕ_P, ϕ_A) fixed while we systematically and independently vary the swimmer persistence length Pe_R and swim force Pe_S. Before preceding to our simulation results it is important to further contextualize the known role and origins of Pe_R

and Pe_S. Many of the unique active behaviors, such as MIPS [41, 44] and particle accumulation on curved surfaces [45] (to name a few), are entirely characterized by the swimmer persistence length Pe_R [46, 47]. In these cases, the propulsive swim force (Pe_S) can simply be scaled out of the problem. However, when doping a material with active particles we must consider the inherent force scale of the target material. Consider a pair of particles interacting with an attractive potential with a well depth of E_0 and a range of a δ. This potential has a natural attractive force scale $F^a \sim E_0/\delta$ that will compete with the swim force of the active particles. When the swim force is smaller than this characteristic attractive force, an active particle will be unable to disrupt the associated particle pair. In contrast, larger swim forces allow swimmers to pull apart interacting particles (see Fig. 4.1). We denote this critical Pe_S at which the swim force is comparable to the attractive force as $\mathrm{Pe}_S^* = F^{swim*}/F^{thermal}$ with $F^{swim*} = F^a$. The ratio of the swim force to the characteristic attractive force is provided by $\mathrm{Pe}_S/\mathrm{Pe}_S^* = F^{swim}/F^a$, an essential parameter in this study. ($\mathrm{Pe}_S/\mathrm{Pe}_S^* = F^{swim}/F^a$ can be thought of as the analog to the Mason number – the ratio of shear forces to attractive forces – in conventional bulk rheology.)

The simple physical consequence described above results in Pe_S playing a pivotal role in active doping and motivates a careful consideration of the experimentally accessible range of swim forces. Living organisms generate a swim force through cyclic, time-irreversible deformations that induce a straining field in the surrounding fluid and propels the organism [48]. As the organism uses the fluid to propel, the strength of the swim force is linear in the solvent viscosity so long as the swimmer can continue to generate the same straining field in the fluid and maintain a constant swim speed U_0. In practice, the mode of swimming is likely not entirely decoupled from the surrounding fluid viscosity, as living organisms can alter their target swim speeds in response to increased dissipation. However, to a first approximation, Pe_S can be varied simply by altering the viscosity of the solvent and can therefore be taken as an arbitrarily tunable parameter.

The flexibility of Pe_S stands in contrast to the persistence length of biological swimmers which will be dictated primarily by the reorientation mechanism of the organism and in this sense can be viewed as an intrinsic material property of the swimmer. Note that this is not the case for synthetic catalytic Janus particles as their swim speed and, thus, their swim force and persistence can be modulated with the concentration of reactant solute and is reduced with increasing solvent

viscosity [49, 50]. These considerations motivate exploration of a wide range of activity space by *independently* varying Pe_R and Pe_S to encompass the extraordinary diverse swimming behavior currently accessible to experiment. This is in contrast to most studies of active matter which assume a thermal reorientation mechanism (true for Janus particles) which couples Pe_R and Pe_S (e.g., $\mathrm{Pe}_R = 3/(4\mathrm{Pe}_S)$ in three dimensions) and are thus restricted to a diagonal line in activity space. For a summary of experimentally achievable swim speeds, we refer the reader to the recent review by Bechinger et al. [27] which highlights the extraordinary range of Pe_S and Pe_R available in experiments.

Structural and Dynamical Control. Figure 4.2A illustrates the structural control afforded by active doping. To accentuate the dynamic contrast between regions in activity space, representative snapshots are shown for structures achieved after simulation durations of $2000\tau_B$ and $200\tau_B$ for $\mathrm{Pe}_S \leq \mathrm{Pe}_S^*$ and $\mathrm{Pe}_S > \mathrm{Pe}_S^*$, respectively.

For weak swimming $\mathrm{Pe}_S \ll \mathrm{Pe}_S^* \approx 50$, the active particles are unable to perturb the passive structures; the initially homogeneous suspension of particles undergoes bicontinuous spinodal decomposition and appears as a coarsening colloidal gel. The coarsening dynamics of the network can be quantified by computing the time evolution of the characteristic largest length scale in the system, which we take as the inverse of the first moment (with respect to the wavevector) of the static structure factor, $q_1(t)$. The weak swimming regime results in coarsening dynamics that are nearly identical to those of a system in which the activity of the swimmers is removed (see Fig. 4.2B). Interestingly, while the active particles in this regime are essentially inert with respect to their kinetic influence, we observe a slight dependence of $q_1(t)$ on the persistence length of the swimmers – with increasing persistence (decreasing Pe_R) resulting in slightly faster coarsening. This trend holds true but is significantly amplified as we increase the propulsive force towards the critical value $\mathrm{Pe}_S \to \mathrm{Pe}_S^*$. In this limit, the coarsening dynamics are greatly accelerated with increasing persistence length (Fig. 4.2B) as activity helps drive the coalescence of the gel strands, seen visually in Fig. 4.2A.

That an active particle is unable to break an individual particle bond yet can assist in the coalescence of network strands (consisting of hundreds of bonds) is surprising (and initially somewhat perplexing) and deserves further examination. However, before doing so, we continue with our exploration of $\mathrm{Pe}_S - \mathrm{Pe}_R$ space by now moving to swim forces beyond the critical value Pe_S^*. One can visually appreciate that the swimmers are no longer bound to other particles as they can generate the

necessary "escape force" to freely swim. Now, armed with the ability to disrupt the fundamental interaction in the system, the active particles have the capacity to alter the underlying globally stable configuration of the material.

When the persistence length of the active particles is on the order of their size $\mathrm{Pe}_R \sim O(1)$, the active particles rapidly coarsen the network (the snapshots in Fig. 4.2A represent structures after only $100\tau_B$ of coarsening), approaching complete phase separation on a time scale that is several orders of magnitude faster than a passive system. Moreover, in comparison to the network strands of a passive gel which have an average particle area fraction of $\phi_P \approx 0.8$, the passive regions in this regime are significantly compressed ($\phi_P \approx 0.9$) under the weight of the (osmotic) swim pressure of the exterior active particles as shown in the local area fraction distribution displayed in Fig. 4.2C. This strongly suggests that the swimmers introduce an additional driving force for phase separation, beyond the latent attraction experienced by all particles. (Consistent with this idea, upon simulating particles without any intrinsic attraction (e.g., purely repulsive interactions), we continue to observe (data not shown) phase separation in this regime, which must be entirely driven by the swimmers.)

Upon increasing the persistence we observe a striking inversion of the previous behavior as the active particles now entirely homogenize or "mix" the system, resulting in the previously bimodal distribution of ϕ_P (representative of a phase separated system) becoming normally distributed about the bulk passive area fraction $\phi_P = 0.4$ (Fig. 4.2C). Importantly, if a MIPS-like mechanism were the origin of the phase separation, increasing the persistence $\mathrm{Pe}_R \ll 1$ would deepen the phase separation rather than reverse it [39–41, 46]. Our doping concentration is sufficiently dilute that our observations are truly a reflection of active particles perturbing the host material.

It is appealing to interpret the $\mathrm{Pe}_S > \mathrm{Pe}_S^*$ regimes as the result of *effective interactions* between the passive particles mediated by the swimmers with the large persistence "mixing" regime resulting from *swimmer-induced repulsion* and the strongly phase separated regime due to a *swimmer-induced attraction*. While this is highly reminiscent of a depletion-like effect there is a significant caveat: here, our depletant (the active particles) is the *same geometric size* as the passive particles, a fascinating point that we will revisit later.

The boundaries between the four regimes discussed above can be appreciated by plotting q_1 of the terminal simulation structure as a function of Pe_S and Pe_R, shown

in Fig. 4.2D. Again, to highlight the dynamic contrast, we plot the q_1 achieved after a duration of $2000\tau_B$ and $200\tau_B$ (which is often sufficient to reach steady-state for $\mathrm{Pe}_S \gg \mathrm{Pe}_S^*$) for $\mathrm{Pe}_S \leq \mathrm{Pe}_S^*$ and $\mathrm{Pe}_S > \mathrm{Pe}_S^*$, respectively. We normalize these q_1 values by that of the purely passive system (activity turned off) after a duration of $2000\tau_B$, which we denote as q_1^p. While this plot is the result of 55 discrete combinations of Pe_S and Pe_R, the smooth contour assists in the delineation of the four regimes.

4.3 Microscale Origins of Dynamic Phase Behavior

The boundary between the high and low persistence behavior for $\mathrm{Pe}_S < \mathrm{Pe}_S^*$ is purely dynamical, while swim forces beyond Pe_S^* dramatically alter both the dynamics and the globally stable configuration. This clear distinction between regimes that offer kinetic control and those that alter both the kinetics and structure is appealing. The task remains both to understand the physics within these regimes and the nature of the boundaries between them. With the phenomenology established, we now proceed to a systematic exploration on the microscopic mechanisms underpinning each regime of our dynamic phase diagram (summarized in Fig. 4.7) before concluding with a higher-level summary and discussion.

Kinetic Control with $Pe_S < Pe_S^*$. We begin by exploring the kinetic pathway provided by active particles with large persistence and $\mathrm{Pe}_S < \mathrm{Pe}_S^*$. The hastening of the gel-coarsening dynamics for these relatively weak activities is consistent with the recent experiments of Szakasits *et al.* which suggests that active particles may enhance the *bulk diffusion* of colloidal gel strands [51]. In these experiments, a small fraction of active Janus particles were found to increase (by up to a factor of 3) the mean-square displacement (in the subdiffusive regime) of the passive particles comprising the gel despite the activity of the particles being insufficient to break an individual colloidal bond. They rationalized this finding by arguing that the active particles create a long-ranged elastic straining field within the network that displaces the gel strands. That we observe such a significant dependence of the coarsening rate on Pe_R *suggests* a finite-ranged straining field in the material with a range that correlates with the swimmer persistence length. We postulate that this swimmer-generated strain in the network strands promotes their eventual breakup and coalescence *via* bulk diffusion and is responsible for the observed enhancement of the coarsening dynamics.

If the swimmers can truly be viewed as microscopic straining agents that promote bulk diffusion, then their influence on the coarsening dynamics should wane as the

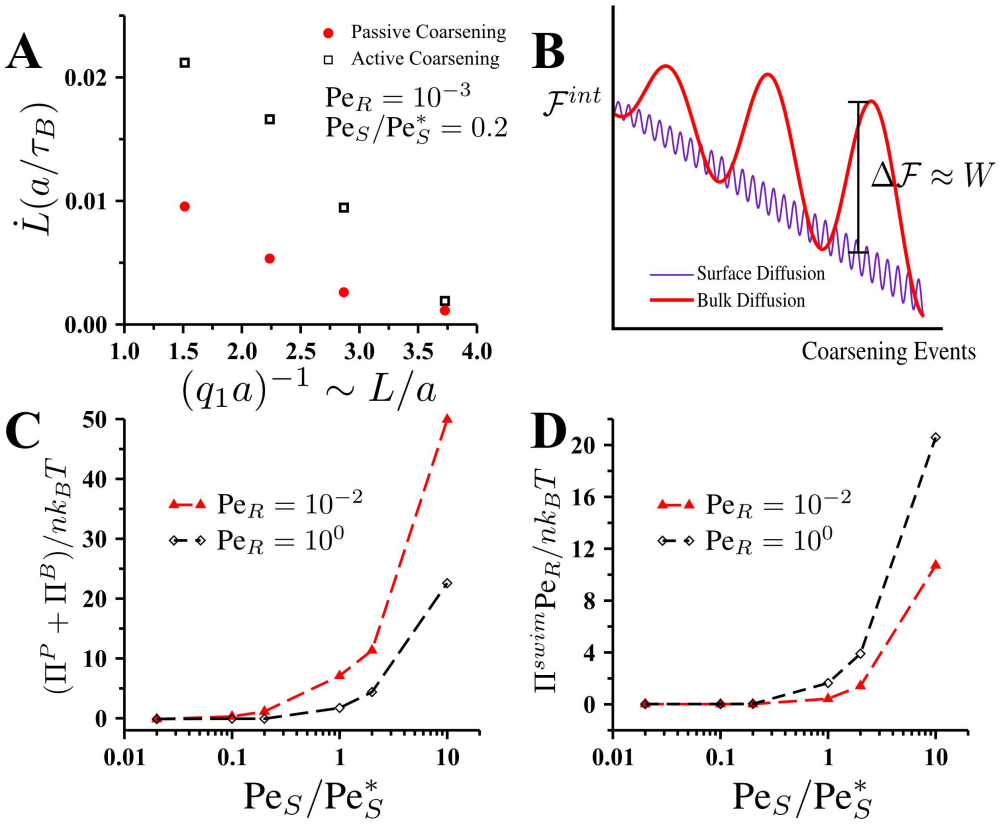

Figure 4.3: (A) Coarsening rate for passive and active systems measured as a function of the initial characteristic length scale L of the material and over a duration of $100\tau_B$. The passive coarsening rate was measured by simply "turning off" the activity of the swimmers in the active system. (B) Schematic of interfacial free energy of a coarsening network as a function of "coarsening events" for two possible mechanisms. (C) Nonswimming and (D) swimming component of the system pressure as a function of Pe_S (note that we have scaled out the effect of persistence in panel D).

gel strands thicken. This physical picture is borne out in Fig. 4.3A wherein we compare the structural evolution of the active and nonactive system beginning from the same configuration characterized by a length scale of $L \sim q_1^{-1}$. With increasing L the active and passive structural coarsening rates begin to converge. The more rapid decay of the active system coarsening rate (in comparison to the passive system) with increasing strand thickness further (albeit implicitly) corroborates our hypothesis that active particles promote bulk diffusion, which more strongly depends on bulk material properties than surface diffusion.

To further understand activity-assisted coarsening, it is instructive to consider the underlying driving force and mechanism for passive gel coarsening. The gel coarsening is driven by the need to reduce the excess (interfacial) free energy of the system

in order to reach the global free energy minimum associated with bulk macroscopic phase separation $\mathcal{F}^{bulk}$. A number of researchers have found that the coarsening of the network strands of passive gels proceeds *via* single-particle diffusion wherein individual particles on the surface of the gel diffuse to energetically more favorable regions of the network [52, 53]. The underlying contributions to the dynamic free energy barrier in this process consists of both the energetic breaking of the bonds as the particle departs the surface and the entropic barrier associated with the free particle finding an energetically more favorable region. The entropic contribution to this barrier is likely to grow as the gel further coarsens and energetically more favorable regions become scarcer. The surface diffusion mechanism for coarsening can thus be viewed as a series of progressively increasing barriers with each traversed barrier slightly reducing the interfacial area of the material, shown schematically in Fig. 4.3B.

In contrast to the surface diffusion coarsening mechanism, coarsening by bulk diffusion entails the diffusion and coalescence of multiparticle domains, with each of these "coarsening events" resulting in the reduction of substantially more surface area than in the surface diffusion mechanism. However, the free energy barrier for bulk diffusion is also considerably higher as it involves the breaking of several particle bonds in order for multiparticle regions to break away from the network and diffuse. This primarily energetic barrier will grow as the domains grow thicker (see Fig. 4.3) and proves too costly for a traditional passive system to overcome with thermal fluctuations alone, precluding coarsening by bulk diffusion. Passive systems with short-ranged attractive interactions cannot spontaneously generate the stress necessary to overcome the mechanical free energy barrier necessary for bulk diffusion [54].

With active dopants, the active particles act as a nonthermal injection of the *mechanical work* necessary to overcome the energetic barriers associated with bulk diffusion in the form stress or pressure – e.g.,"PV" work. We can characterize the mechanical influence of the active particles by computing the total pressure Π^T of the system

$$\Pi^T = \Pi^B + \Pi^P + \Pi^{swim}, \tag{4.1}$$

where Π^B is the Brownian "ideal gas" pressure nk_BT (where n is the number density), Π^P is the pressure arising from interparticle interactions and Π^{swim} is the swim pressure [30], the pressure associated with the random walk motion of the active particles. While the swim pressure is small for $\mathrm{Pe}_S < \mathrm{Pe}_S^*$ (as the active

particles are precluded from freely swimming), active particles are found to make a substantial indirect contribution to the system pressure reflected in the Pe_R and Pe_S dependence of Π^P (Fig. 4.3C). When the swim force is negligible, the overall pressure of the coarsening gel $\Pi^T \approx \Pi^B + \Pi^P$ is very small and, in fact, slightly negative as recently reported [55]. (The physical origin of this negative pressure is that the interfacial area A^{int} and, hence, interfacial free energy of the gel scales with the system size ($\mathcal{F}^{int} \approx \gamma A^{int} \sim V$ where the interfacial tension is positive $\gamma > 0$) and provides a substantial negative contribution ($\Pi^{int} = -\partial \mathcal{F}^{int}/\partial V < 0$) to the total osmotic pressure.)

As the swim force is increased to its critical value $\mathrm{Pe}_S \to \mathrm{Pe}_S^*$ the pressure begins to rise sharply, inverting in sign and reaching a value on the order of 10 times nk_BT at $\mathrm{Pe}_S \approx \mathrm{Pe}_S^*$. More persistent particles are found to result in large pressures. Note that when active particles can swim freely the "ideal" swim pressure is larger for increasing persistence

$$\Pi^{swim}(\phi_A \to 0) = n_A \zeta U_0^2 \tau_R/2 \sim n_A k_B T \mathrm{Pe}_S/\mathrm{Pe}_R, \tag{4.2}$$

where n_A is the number density of active particles. That the persistence plays such an essential role in generating stress despite the particles being embedded within the material (and unable to freely swim and generate a swim pressure, as shown in Fig. 4.3D) further corroborates our assertion that persistence plays a pivotal role in generating the straining field necessary to promote bulk diffusion. It is important to note that despite the large stresses generated when $\mathrm{Pe}_S < \mathrm{Pe}_S^*$, this eventually proves insufficient to overcome the free energy barrier associated with the breakup of increasingly thick gel strands. From this viewpoint, the active particles in this regime can enhance the rate of structure formation up to a particular microscopic length scale.

Activity-Mediated Interactions with $Pe_S > Pe_S^*$. We now turn our attention to the $\mathrm{Pe}_S > \mathrm{Pe}_S^*$ region of our dynamic phase diagram. It is interesting to note that for all values of Pe_R in this region there are no signs of the active particles "feeling" any attraction. That is, when $\mathrm{Pe}_S > \mathrm{Pe}_S^*$ we observe no systems with statistically significant configurations in which the active particles are clustered in a low-energy state. This physical situation is consistent with the basic intuition offered by many of the phenomenological theories [46, 56–59] for active matter "thermodynamics": active particles have an apparent temperature that is amplified by their intrinsic activity resulting in the leading order "ideal swimmer" chemical potential (defined by invoking

micromechanical or Gibbs-Duhem-like relations using the swim pressure [46, 59]) of $\mu^{swim} \sim \zeta U_0^2 \tau_R \ln(\phi_A)$. Thus, despite the vastly different microscopic dynamics of active and passive particles, swimmers can in some cases still be described by an effective temperature given by $\sim \zeta U_0^2 \tau_R$. Caution must be exercised when applying this perspective. For example, while this suggests that active particles with $\zeta U_0^2 \tau_R > E_0$ will behave as hot particles that are unaffected by the weak attraction, swimmers with $\mathrm{Pe}_S < \mathrm{Pe}_S^*$ are unable to generate enough force to escape particle attractions and, as a result, are not spatially distributed in the manner that the effective temperature perspective would suggest. However, as the critical escape swim force is reached, the now *accessible* translational entropy drives the "release" of active particles from attractive bonds.

The freely swimming particles with $\mathrm{Pe}_S > \mathrm{Pe}_S^*$ entirely reshape the globally stable configuration of the material, pushing the system to disparate regions of phase space: complete homogenization at larger persistence lengths ($\mathrm{Pe}_R \ll 1$) or strong phase separation with persistence lengths on the order of the body size of the swimmer. These behaviors motivate the perspective that the active particles are mediating effective (e.g., depletion) interactions between the passive particles. Numerous studies have sought to describe activity-mediated interactions between passive particles [60–65] with most of these studies fixing two passive objects in an active bath and measuring the force required to keep the objects fixed, the original perspective taken by Asakura and Oosawa (AO) in describing the origins of traditional passive depletion [66, 67]. However, the role of the size ratio of the depletant and passive body – which is decisive in traditional thermal depletion [68] – remains largely unexplored. The original AO picture is that *smaller* particles (the depletants) will create an entropic attractive force between *larger* particles in an effort to increase the space available to the smaller particles and lower the system free energy. However, our active particles are of the *same geometric size* as our passive particles. In the context of the previously discussed "effective" translational entropy, the swimmer-induced attraction at larger Pe_R can be thought of as depletion attraction driven by an *activity asymmetry* with no geometric size difference required.

The concept of an activity asymmetry driven depletion interaction merits further systematic examination and will invariably require relaxing many of the underlying assumptions in the traditional AO picture. For example, when the ratio of the depletant size (radius a) to the passive body size (radius R) (see schematic in Fig. 4.4A) exceeds a value of $a/R > 0.15$, the depletion interaction is known

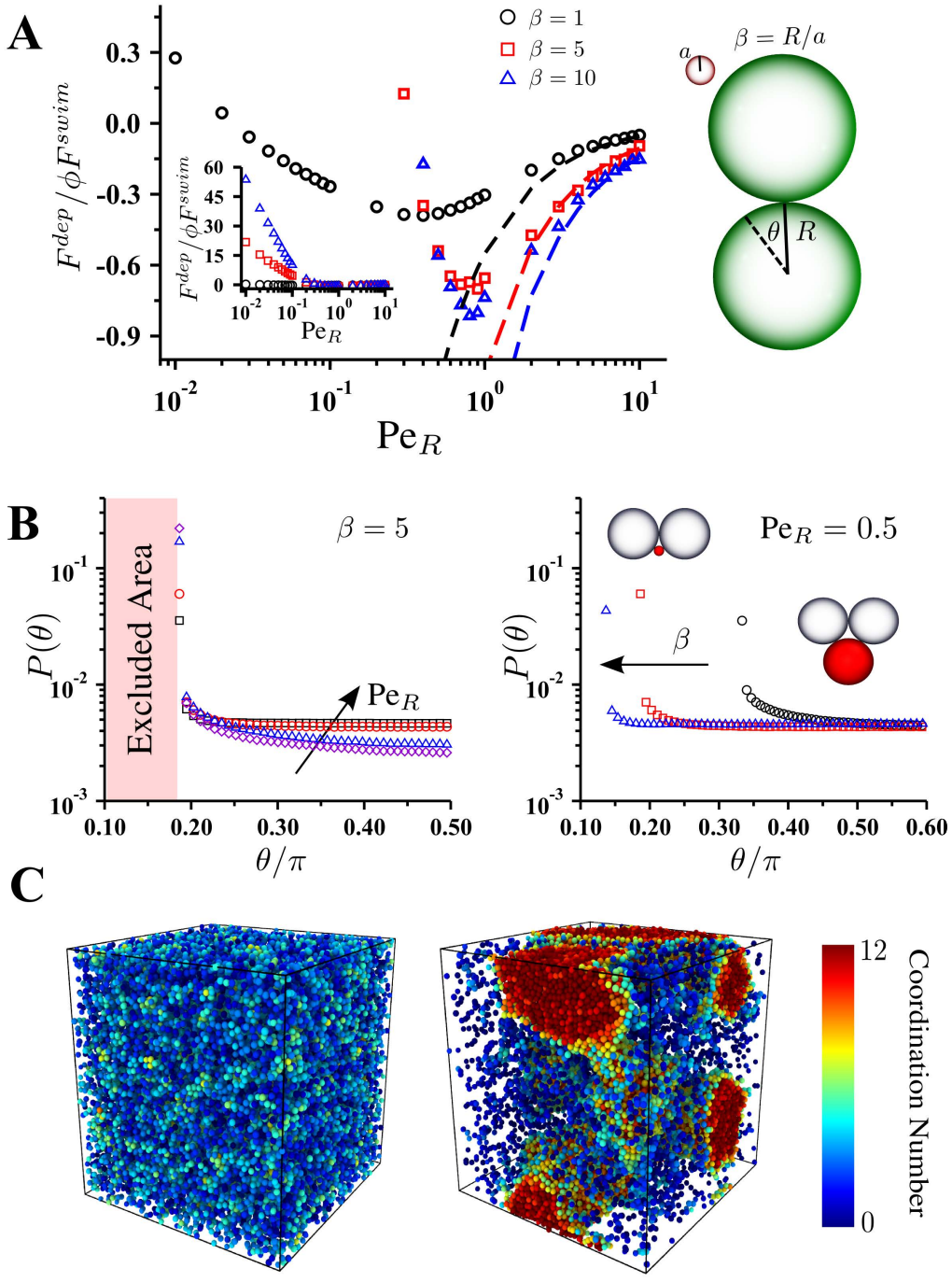

Figure 4.4: (A) The probe-swimmer size ratio and swimmer persistence length dependence of the mechanical depletion force with the lines representing eq (4.4). The non-monotonic region is magnified here, while the inset displays the complete data in its entirety. (B) Swimmer-probe contact statistics as a function of the (left) persistence (with $\mathrm{Pe}_R = 1, 0.5, 0.1, 0.05$) and (right) size ratio (symbols are the same as in panel A). (C) Representative snapshots after $100\tau_B$ of a three-dimensional system of monodisperse active particles (not shown) and polydisperse (5%) passive particles at volume fractions of $\phi_A = 0.02$ and $\phi_P = 0.20$, respectively, with $\mathrm{Pe}_S/\mathrm{Pe}_S^* = 200$ and (left) $\mathrm{Pe}_R = 10^{-2}$ and (right) $\mathrm{Pe}_R = 1$. Particles are colored by coordination number to aid in cluster visualization.

to no longer be pairwise, with the resulting multibody interactions deepening the effective attraction between the passive bodies [68]. Furthermore, the classical AO picture of treating the depletant as ideal will invariably break down with larger depletant particles, which are subjected to excluded-volume-related correlations. Nevertheless, in an effort to isolate the leading order role of the size ratio in active depletion, here we explore only the two-body interaction between passive particles in an ideal active bath. We fix two identical passive disks at contact in a bath of non-Brownian (to isolate the role of activity) active particles at an area fraction of ϕ. In the limit of infinitesimal persistence length ($\mathrm{Pe}_R \to \infty$), the active particles behave as Brownian particles with the force acting between the passive bodies *at contact* given by an AO form

$$F^{dep} = -\frac{\zeta U_0^2 \tau_R \phi}{a\pi}\sqrt{1+2\beta}, \tag{4.3}$$

where $\beta = R/a$ is the size ratio and we have substituted the activity $\zeta U_0^2 \tau_R/2$ in for what is traditionally $k_B T$ (an exact substitution in the limit $\mathrm{Pe}_R \to \infty$). (Note that this idealized AO perspective predicts a finite attractive force for *all* size ratios. This is clearly incorrect and is the result of neglecting the concentration and translational entropy loss of the passive bodies.) The active-depletion force must necessarily scale as $F^{dep} \sim \phi F^{swim}$ as the active bath is dilute and the swim force is the only force scale in the problem. The nondimensional depletion force $F^{dep}/\phi F^{swim}$ is thus entirely determined by geometric considerations (size ratio β and persistence length Pe_R) with a value of

$$F^{dep}/\phi F^{swim} = -\frac{\sqrt{1+2\beta}}{\pi \mathrm{Pe}_R}, \tag{4.4}$$

to leading order in Pe_R^{-1}. Equation (4.4) has a number of noteworthy features: (i) the depletion force is always attractive (negative); (ii) the magnitude of the force is a monotonically increasing (decreasing) function of persistence (Pe_R); and (iii) the magnitude is an increasing function of the size ratio β.

Independent of size ratio, as the persistence increases we find a nonmonotonic response in the depletion force (shown in Fig. 4.4A) with eq (4.4) serving as a lower bound as was found by Smallenburg and Löwen [65]. Initially, decreasing Pe_R results in an increased attraction (more negative) between the particles, consistent with the AO expectations: the particles are "hotter" and should result in the force decreasing with Pe_R^{-1} (eq (4.4)). However, with increasing persistence, the particles begin to accumulate at the wedge created by the two passive disks, with the distribution of

swimmers on the passive disk surfaces transitioning from homogeneous (with the exception of the exclusion zone) to sharply peaked at the wedge (see Fig. 4.4B). This results in a repulsive force that competes with the traditional AO attractive force, resulting in the depletion force reaching a minimum followed by a sharp increase – particularly for $\beta > 1$. Interestingly, while the traditional AO picture (eq (4.4)) suggests that larger depletants reduce attraction – and indeed, we find the minimum force is an increasing function of size ratio – here we find that reducing the size ratio β significantly broadens the range of Pe_R where the depletion force is attractive, with an order of magnitude increase in the persistence length at which the attraction inverts to repulsion. This stems from the reduction in swimmer accumulation within the wedge with increasing swimmer size – larger swimmers are less likely to be "trapped" in the wedge as illustrated in Fig. 4.4C. Thus, like-size swimmer depletants not only reveal and emphasize the important notion of activity asymmetry driven interactions but fundamentally broaden the window of persistence lengths in which swimmer-mediated attraction is observed.

The effective repulsion found when the persistence length is large compared to the passive body size ($R/l_p = \mathrm{Pe}_R\beta \ll 1$) is in agreement with the homogenization observed in our full mixture simulations at small Pe_R. This picture – while mechanically intuitive – results in the active particles conceding free volume, a result which appears at odds with the intuition offered by phenomenological active-matter thermodynamic theories previously referenced [30, 56, 57]. While interesting, reconciling this is beyond the scope of this work.

We emphasize that the depletion physics described above should hold for three dimensions as well. We explicitly verify this by simulating the 3D analog of our system in the regimes of swimmer-induced repulsion ($\mathrm{Pe}_S > \mathrm{Pe}_S^*$ and $\mathrm{Pe}_R \ll 1$) and attraction ($\mathrm{Pe}_S > \mathrm{Pe}_S^*$ and $\mathrm{Pe}_R \sim O(1)$), with representative snapshots of terminal configurations shown in Fig. 4.4C (see the figure caption for simulation details). We indeed find activity-induced rapid homogenization/phase separation in the expected regimes.

Microstructural Dependence of Active Depletion. We argued above that the boundary delineating the activity-induced attraction and repulsion regimes is entirely dictated by Pe_R and β – with β being the size ratio between the passive and active particles. That we can think of the active particles as interacting with individual passive particles suggests that the swimmers have sufficient propulsive force to "dislodge" the passive particle from whatever latent structure the particles form. This is

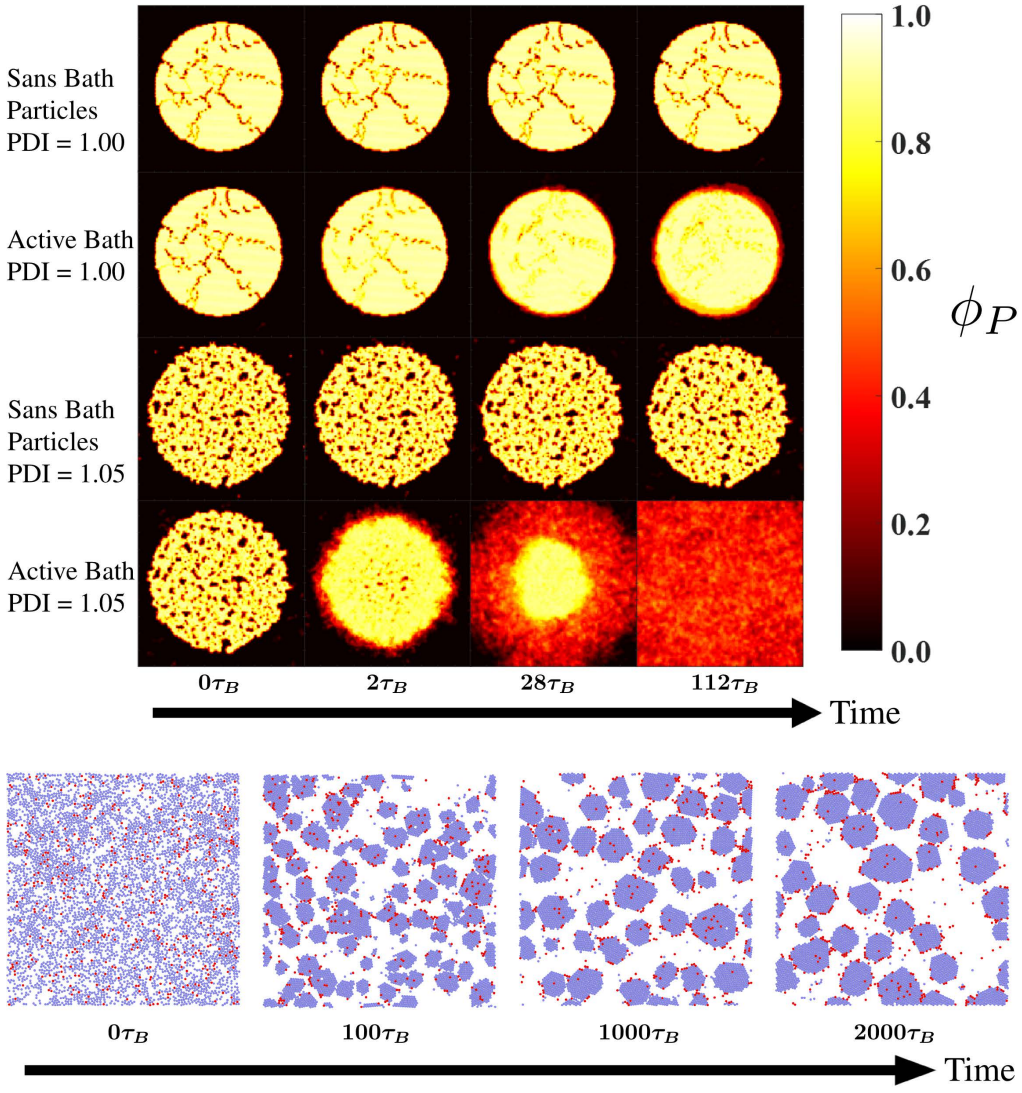

Figure 4.5: (Top) Rows represent the time evolution of a prepared passive disk consisting of either monodisperse or polydisperse particles with and without surrounding active particles with $\mathrm{Pe}_S/\mathrm{Pe}_S^* = 1.25$ and $\mathrm{Pe}_R = 10^{-2}$ (e.g., the activity-induced repulsion regime). (Bottom) Time evolution of a monodisperse system with identical parameters as the above disk simulations but beginning from a spatially homogeneous configuration. Active particles are shown in red.

indeed the case for our system when the propulsive swim force exceeds the critical value Pe_S^*. However, this may not generally hold as, in principle, the latent microstructure of the passive particles may prove too formidable for an active particle to disrupt. To illustrate this point, we prepare two systems that nominally differ only in the local microstructure by varying the passive particle size distribution. We initialize our systems by arranging all of the passive particles into a close-packed disk at the center of the simulation cell, with one system consisting of polydisperse (5%) passive particles and the other consisting of monodisperse passive particles. Both disks are stable over time in the absence of active particles as macroscopic phase separation is the globally stable configuration. The monodisperse system is crystalline (with some defects), while the polydisperse system is disordered with a number of large defects (see Fig. 4.5). We next insert active particles into the open space outside of the disks. With $\mathrm{Pe}_S = 1.25\mathrm{Pe}_S^*$ and $\beta\mathrm{Pe}_R \ll 1$, we anticipate that the active particles should induce an effective repulsion between particles and homogenize the system, which is indeed true for the polydisperse system. However, for the crystalline system no such mixing was observed. Rather, we find that active particles build up on the surface – they are unable to penetrate the material – and compress the disk (the details regarding the transience of this compression were explored by Stenhammar et al. [39]) as shown in Fig. 4.5.

That the active particles appear unable to induce repulsion between the monodisperse particles stems from their inability to dislodge individual particles from the crystalline microstructure. However, this does not mean that the swimmers are unable to induce effective interactions. Rather, we argue that the crystallinity alters the interaction from the expected repulsion to attraction. This implies that the structures that active particles mediate interactions between are not necessarily individual particles, but rather the smallest length scale structure that the swimmers can "push" – an implicitly necessary criteria for depletion-like interactions. The ratio of the length scale of this intrinsic structural unit L_0 to the swimmer size a is the relevant size ratio (along with Pe_R) in determining the strength/sign of the active depletion force.

This length scale L_0 is sensitive to the underlying microstructure (characterizable by the passive-particle pair distribution function $g_0(r)$) that the swimmer must compete with, the swim force Pe_S and perhaps even the preparation conditions of the material. Consider the monodisperse system but now prepared from a homogeneous initial configuration. Nearly instantly after we begin the simulation, the passive particles

nucleate into several small crystalline "islands" that the swimmers cannot penetrate (see Fig. 4.5). Initially when the island size L_0 is small compared to the persistence length, the swimmers induce repulsion between islands as $L_0/l_p = \beta \mathrm{Pe}_R \ll 1$. However, over time islands eventually collide and merge, with the swimmers unable to break apart the resulting structure. The average island size L_0 will *eventually* become much larger than the persistence length ($L_0/l_p \gg 1$) as activity and thermal energy are unable to break the islands. In this limit, the swimmers would induce interisland attraction and *facilitate* island coalescence. Intriguingly, the influence of "microstructural integrity" (which the polydisperse system lacks) is to *expand* the window of activity-induced attraction by driving up the effective size ratio $\beta_{eff} = L_0/a$ where L_0 is a functional of $g_0(r)$, Pe_S and possibly the preparation history of the material.

We caution that *only* when the persistence length is much smaller than all of the other geometric length scales of the passive bodies ($L_0/l_p \gg 1$) is activity-mediated attraction *ensured*. It is precisely in this limit wherein the active particles become equivalent to "hot" Brownian particles and traditional AO physics is applicable (e.g., eq (4.4)). Short of this limit, geometric details – which may strongly influence the distribution of swimmers on the passive body surface – must be considered, as highlighted in Fig. 4.4A.

Dynamic Consequences of $Pe_S > Pe_S^*$. With $\mathrm{Pe}_S > \mathrm{Pe}_S^*$, the active particles not only modify the effective interactions between the passive particles, but also dramatically alter the kinetics of phase separation. Figure 4.6 illustrates representative snapshots of the coarsening process in the activity-induced attraction regime. Note that here the system size (number of particles) is 10 times larger than the systems shown in Fig. 4.2A and the growth of the domains is monotonic in time, indicative of true macrophase separation. While increasing the magnitude of attraction is typically thought to slow particle dynamics, with increasing $\mathrm{Pe}_S/\mathrm{Pe}_S^*$ we find an increase in the coarsening rate of the domains. This highlights the important point that, dynamically, active particles can "share" their diffusivity with the passive particles: providing both strong attractive interactions and the necessary "kicks" to rapidly assemble the material. The material is structurally cool but dynamically hot.

Fascinatingly, as we increase the activity-induced attraction by increasing Pe_S further beyond Pe_S^*, the connectivity of the strands begins to decrease, with the dense phase no longer a bicontinuous percolating cluster (a gel) at the largest Pe_S explored. While strand connectivity is of course expected to be reduced with increasing strand

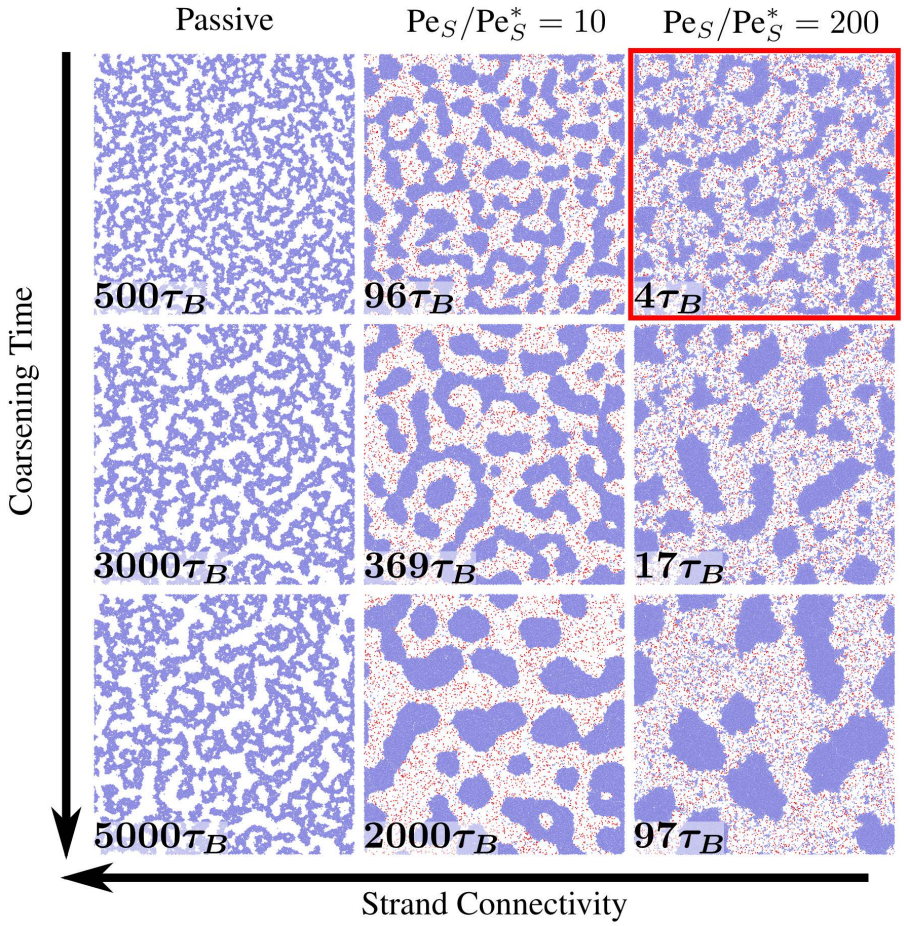

Figure 4.6: Qualitative illustration of both the rapid coarsening in the activity-induced attraction regime and the transition from bicontinuous to droplet-like spinodal decomposition with increasing Pe_S for $\mathrm{Pe}_S > \mathrm{Pe}_S^*$ and $\mathrm{Pe}_R = 1$. Active particles are shown in red. The left-most column illustrates the coarsening process for a passive system.

thickness, we emphasize that this change in the coarsening process is observed even in the early stages of phase separation (see the snapshot enclosed in a red square in Fig. 4.6). This suggests a fundamental alteration of the coarsening mechanism from bicontinuous spinodal decomposition – wherein a gel-like space-spanning structure thickens with time – to a mechanism that appears similar to droplet spinodal decomposition (see Fig. 4.6), where demixing is achieved by the rapid formation of particle-rich drops that merge over time [69].

For traditional passive systems, transitioning from bicontinuous to droplet spinodal decomposition is expected to only occur by modulating the global particle concentration; the different behavior observed here highlights the crucial dynamic role of activity. It was recently shown that the mechanism for droplet coalescence is

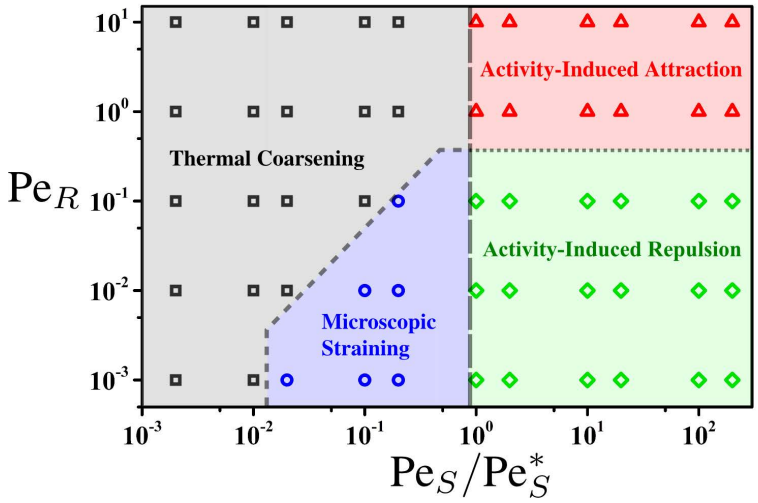

Figure 4.7: Dynamic phase diagram of an active doped gel. Materials embedded with active particles in the microscopic straining regime will exhibit improved coarsening rates on length scales L that correlate with swimmer persistence l_p. The regimes of activity-induced attraction/repulsion are due to depletion-like forces and are separated by a geometrically controlled boundary that depends on β_{eff} and Pe_R.

due to Marangoni-type forces that induce an interdroplet correlation in addition to typical Brownian diffusion [70]. The rapid droplet coalescence observed in our simulations is likely due to the nonthermal diffusion provided by the swimmers to the droplets, in a manner similar to the oft-studied tracer diffusion problems in active matter [71, 72]. It will be interesting to see if the scalar active matter theories [57] used to explore the phase separation dynamics of purely active systems can capture the coarsening behavior reported here.

4.4 Conclusions

We explored the use of active dopants for material design using a simple model system of a suspension of gel-forming sticky particles seeded with a small fraction of swimmers. We found that the active dopants provide a wide range of structural and dynamical control as a function of the swim force (Pe_S) and persistence length (Pe_R), the two properties governing the underlying microscopic swimmer dynamics. By systematically exploring the full $\mathrm{Pe}_S - \mathrm{Pe}_R$ space, we observed three distinct regimes afforded by the active dopants: microscopic straining, activity-induced attraction and activity-induced repulsion, as summarized in the dynamic phase diagram presented in Fig. 4.7. We stress that the boundaries have a degree of "fuzziness" as there are finite transition zones, perhaps best represented in Fig. 4.2D. Nevertheless, the

distinctions between the regimes are clear.

In the microscopic straining regime, the swim force is near its critical value ($\mathrm{Pe}_S \rightarrow \mathrm{Pe}_S^*$), allowing swimmers to strain the material structure and provide kinetic control at length scales L comparable to the persistence length l_p of the particles, a feature that is perhaps attractive for microphase separating systems. Here, the swimmers are unable to generate enough force to fundamentally alter the underlying globally stable configuration of the material. In contrast, when the propulsive swim fore is increased beyond its critical value Pe_S^*, the swimmers mediate strong effective interactions that entirely alter the material phase behavior while also fundamentally altering the system dynamics.

In this regime, active particles are found to act as depletants despite there being no geometric size asymmetry between them and the passive particles, revealing the notion of "activity asymmetry" driven depletion. The effective attraction regime is broadened with increasing "microstructural integrity" with coarsening dynamics that are fundamentally altered in comparison to analogous passive systems. While the effective attraction mediated by the swimmers will deepen the phase separation, the remarkable kinetics afforded by this regime introduces the intriguing prospect of using activity to quickly complete the phase separation process with a resulting configuration that is "supercooled" with respect to the globally stable configuration in the absence of activity. This idea would be particularly applicable to materials in which the underlying globally stable configuration is not fundamentally altered with increasing attraction, as is the case with many close-packed structures. Activity could then simply be "switched off" (e.g., by ceasing to provide the necessary fuel for the active particles to swim) with the resulting structure achieved on a time scale that is orders of magnitude smaller than passive dynamics would allow for.

The clear delineation between regimes in which active particles preserve the underlying globally stable configuration ($\mathrm{Pe}_S < \mathrm{Pe}_S^*$) and those in which swimmers entirely alter the underlying phase behavior ($\mathrm{Pe}_S > \mathrm{Pe}_S^*$) is an enticing feature of active dopants. That the swim force plays the decisive role in dictating the location on the phase diagram results in a number of intriguing effects. Principal among these is that simply by increasing the system viscosity (in a manner that does not alter the particle chemistry) one can modulate the swim force exerted by many biological microswimmers and can therefore dramatically alter the phase behavior of the entire material, e.g., a macroscopic transport property can alter the state or phase of a system.

Active doping for material design has a number of appealing features. In contrast to macroscopic deformation protocols, active doping does not intrinsically break the rotational symmetry of the system and can therefore be used to improve the self-assembly of ordered structures with various symmetries. Further, the properties of the swimmers are in principle entirely orthogonal to those of the host material. It is our hope that by establishing the dynamic phase diagram for a model material and elucidating the key length, force and time scales delineating the dynamic phase boundaries, our results can be directly tested in experiment and can be applied quite generally to a host of colloidal materials with varying chemistries, interaction potentials and free energy landscapes. While we have focused primarily on the implications of our work for material design, it would be intriguing to probe the applicability of our results toward naturally occurring systems of swimming microorganisms embedded in "sticky" gel-like environments such as biofilms [73]. Our findings suggest that, armed with a sufficient amount of activity and depending on the length/force scales of the surroundings, microorganisms can fundamentally reshape their environment – an interesting conjecture that merits further examination.

4.5 Appendix

We model our passive particles as polydisperse disks with a mean radius a and a polydispersity of 5%. The polydispersity is included by normally distributing the particle radii between 21 discrete sizes that are evenly spaced apart with a size range of $a \pm 15\%a$. The drag coefficient ζ_i of particle i is linearly scaled with the particle size a_i. The active particles are modeled as monodisperse disks with radius a. Initial configurations are generated by placing the particles randomly followed by applying the potential-free algorithm [74] to move overlapping disks to contact.

The motion of the particles is governed by the overdamped Langevin equation which, upon integration over a discrete time step Δt, results in the displacement equation

$$\Delta \boldsymbol{x_i} = \Delta \boldsymbol{x_i^B} + \frac{1}{\zeta_i}\left(\boldsymbol{F_i^{swim}} + \sum_{j\neq i} \boldsymbol{F_{ij}^P}\right)\Delta t, \tag{4.5}$$

where $\Delta \boldsymbol{x_i}$ is the particle displacement over the simulation time step and $\Delta \boldsymbol{x_i^B}$ is the stochastic Brownian displacement (taken to be a white noise with a mean of $\mathbf{0}$ and variance of $2D^B\Delta t\boldsymbol{I}$ with $D^B = k_BT/\zeta_i$), while $\boldsymbol{F_i^{swim}}$ and $\boldsymbol{F_{ij}^P}$ are the swim force and interparticle forces from particle j, respectively. For passive particles, the swim force is identically zero, while for active particles it is defined as $\boldsymbol{F_i^{swim}} = \zeta U_0 \boldsymbol{q_i}$.

We model the reorientation dynamics of $\boldsymbol{q_i}$ as a continuous random process (as opposed to, for example, run-and-tumble motion) with the magnitude of random torques selected such that the rotational diffusivity is τ_R^{-1}. In two dimensions, $\boldsymbol{q_i} = (\cos(\theta_i), \sin(\theta_i))$ where the angle θ_i evolves according to

$$\Delta\theta_i = \frac{1}{\zeta_i^R} L_i^R \Delta t, \tag{4.6}$$

where $\Delta\theta_i$ is the angular displacement over the simulation time step, ζ_i^R is the rotational drag and L_i^R is a random torque with a mean of 0 and a variance of $2(\zeta_i^R)^2/(\tau_R \Delta t)$. Note that the rotational drag has no dynamical consequence as eq (4.6) can be rewritten as $\Delta\theta_i = \tilde{L}_i^R \Delta t$ where the redefined torque $\tilde{L}_i^R$ now has a variance of $2/\tau_R \Delta t$. Note that we do not assume that the rotational diffusion is thermal in origin and thus, τ_R is entirely decoupled from all other system parameters. The interparticle force $\boldsymbol{F_{ij}^P} = -\partial E_{ij}(r_{ij})/\partial \boldsymbol{r_{ij}}$ derives from the Morse potential

$$E_{ij}(r)/E_0 = \exp[-2\kappa(r - d_{ij})] - 2\exp[-\kappa(r - d_{ij})], \tag{4.7}$$

where d_{ij} is the sum of the radii of the interacting particles $d_{ij} = a_i + a_j$ and κ is an inverse screening length set to $\kappa a = 30$. Pair interactions are cutoff beyond distances of $1.25 d_{ij}$. The simulation time step must be reduced with increasing particle activity to ensure numerical stability of eq (4.5). For $\mathrm{Pe}_S/\mathrm{Pe}_S^* \leq 2$, we use a time step of $\Delta t = 5 \times 10^{-6}$, while for $\mathrm{Pe}_S/\mathrm{Pe}_S^* = 10$, 20, 100 and 200 we use time steps of $\Delta t = 1 \times 10^{-6}$, 5×10^{-7}, 1×10^{-7} and 5×10^{-8}, respectively.

The large-scale simulations conducted for the data in Fig. 4.3C, D, Fig. 4.4C and Fig. 4.6 were performed using the GPU-enabled HOOMD-blue molecular dynamics package with a total of 33000 particles [75, 76]. All other data were obtained using our in-house CPU-based code with the simulations presented in Fig. 4.2 and Fig. 4.3A consisting of 3300 particles and the simulations presented in Fig. 4.5 consisting of 5500 total particles.

We obtained the simulation results in Fig. 4.4 by using the potential-free algorithm to model truly hard spheres [74]. The force required to hold a probe particle fixed is simply the sum of the collisional forces [77] imparted by the active bath particles. For these simulations, we select a time step of $\Delta t = 10^{-3} a/U_0$. Simulations were run for a duration of $1000\tau_R$ with 10000 independent swimmers. Swimmers can induce incredibly long-ranged ($\sim O(l_p)$) interactions between passive probes, requiring the simulation box size to be made sufficiently large to prevent self-interactions of the fixed probes with their periodic images.

The characteristic largest length scale in the simulation was taken to be inversely proportional to the first moment of the static structure factor q_1

$$q_1(t) = \frac{\int_{q_m}^{q_c} S(q;t) q dq}{\int_{q_m}^{q_c} S(q;t) dq}, \tag{4.8}$$

where q_m is the minimum possible wavenumber (physically bounded by the size of our simulation cell) and q_c is the cutoff wavenumber which we set to $2q_c a = 3$ to include the contribution of all large wavelengths as was done in the experiments of Lu et al. [14] The static structure is computed directly from the particle coordinates

$$S(q;t) = \frac{1}{N} \left\langle \left| \sum_{j=1}^{N} \exp(i\boldsymbol{q} \cdot \boldsymbol{x_j}(t)) \right|^2 \right\rangle, \tag{4.9}$$

where N is the total number of *passive* particles.

The interaction component to the pressure Π^P was computed using the standard virial approach with $\Pi^P = n\langle \boldsymbol{x_{ij}} \cdot \boldsymbol{F_{ij}} \rangle / 2$ where $\boldsymbol{x_{ij}}$ and $\boldsymbol{F_{ij}}$ are the interparticle distance and force between particles i and j, respectively, n is the number density of the system and the brackets denote an ensemble average over all particle pairs. We compute the swim pressure using the "impulse" expression [32] that is valid for active particles which feel no interparticle or external torques

$$\Pi^{swim} = n \left\langle \tau_R \boldsymbol{v_i} \cdot \boldsymbol{F_i^{swim}} \right\rangle / 2, \tag{4.10}$$

where $\boldsymbol{v_i}$ is the net velocity of particle i (e.g., eq (4.5) divided by Δt). This expression results exactly in the correct swim pressure for ideal active particles and has been shown [78] to reproduce the traditional virial method [30, 31] for computing the swim pressure.

References

[1] Glotzer, S. C.; Solomon, M. J. Anisotropy of Building Blocks and Their Assembly into Complex Structures. *Nat. Mater.* **2007**, *6*, 557.

[2] Grzelczak, M.; Vermant, J.; Furst, E. M.; Liz-Marzán, L. M. Directed Self-assembly of Nanoparticles. *ACS Nano* **2010**, *4*, 3591–3605.

[3] Sacanna, S.; Pine, D. J. Shape-anisotropic Colloids: Building Blocks for Complex Assemblies. *Curr. Opin. Colloid Interface Sci.* **2011**, *16*, 96–105.

[4] Boles, M. A.; Engel, M.; Talapin, D. V. Self-assembly of Colloidal Nanocrystals: From Intricate Structures to Functional Materials. *Chem. Rev.* **2016**, *116*, 11220–11289.

[5] Damasceno, P. F.; Engel, M.; Glotzer, S. C. Predictive Self-assembly of Polyhedra into Complex Structures. *Science* **2012**, *337*, 453–457.

[6] Van Anders, G.; Ahmed, N. K.; Smith, R.; Engel, M.; Glotzer, S. C. Entropically Patchy Particles: Engineering Valence through Shape Entropy. *ACS Nano* **2014**, *8*, 931–940.

[7] Zhang, Z.; Glotzer, S. C. Self-assembly of Patchy Particles. *Nano Lett.* **2004**, *4*, 1407–1413.

[8] Jiang, S.; Chen, Q.; Tripathy, M.; Luijten, E.; Schweizer, K. S.; Granick, S. Janus Particle Synthesis and Assembly. *Adv. Mater. 22*, 1060–1071.

[9] Mirkin, C. A.; Letsinger, R. L.; Mucic, R. C.; Storhoff, J. J. A DNA-based Method for Rationally Assembling Nanoparticles into Macroscopic Materials. *Nature* **1996**, *382*, 607.

[10] Wang, Y.; Wang, Y.; Breed, D. R.; Manoharan, V. N.; Feng, L.; Hollingsworth, A. D.; Weck, M.; Pine, D. J. Colloids with Valence and Specific Directional Bonding. *Nature* **2012**, *491*, 51.

[11] Obana, M.; Silverman, B. R.; Tirrell, D. A. Protein-mediated Colloidal Assembly. *J. Am. Chem. Soc.* **2017**, *139*, 14251–14256.

[12] Li, F.; Josephson, D. P.; Stein, A. Colloidal Assembly: The Road from Particles to Colloidal Molecules and Crystals. *Angew. Chem., Int. Ed.* **2011**, *50*, 360–388.

[13] Anderson, V. J.; Lekkerkerker, H. N. W. Insights into Phase Transition Kinetics from Colloid Science. *Nature* **2002**, *416*, 811.

[14] Lu, P. J.; Zaccarelli, E.; Ciulla, F.; Schofield, A. B.; Sciortino, F.; Weitz, D. A. Gelation of Particles with Short-range Attraction. *Nature* **2008**, *453*, 499.

[15] Ruzicka, B.; Zaccarelli, E.; Zulian, L.; Angelini, R.; Sztucki, M.; Moussaïd, A.; Narayanan, T.; Sciortino, F. Observation of Empty Liquids and Equilibrium Gels in a Colloidal Clay. *Nat. Mater.* **2010**, *10*, 56.

[16] Swan, J. W.; Vasquez, P. A.; Whitson, P. A.; Fincke, E. M.; Wakata, K.; Magnus, S. H.; Winne, F. D.; Barratt, M. R.; Agui, J. H.; Green, R. D.; Hall, N. R.; Bohman, D. Y.; Bunnell, C. T.; Gast, A. P.; Furst, E. M. Multiscale Kinetics of a Field-directed Colloidal Phase Transition. *Proc. Natl. Acad. Sci. USA* **2012**, *109*, 16023–16028.

[17] Swan, J. W.; Bauer, J. L.; Liu, Y.; Furst, E. M. Directed Colloidal Self-assembly in Toggled Magnetic Fields. *Soft Matter* **2014**, *10*, 1102–1109.

[18] Risbud, S. R.; Swan, J. W. Dynamic Self-assembly of Colloids through Periodic Variation of Inter-particle Potentials. *Soft Matter* **2015**, *11*, 3232–3240.

[19] Sherman, Z. M.; Swan, J. W. Dynamic, Directed Self-assembly of Nanoparticles *via* Toggled Interactions. *ACS Nano* **2016**, *10*, 5260–5271.

[20] Sherman, Z. M.; Rosenthal, H.; Swan, J. W. Phase Separation Kinetics of Dynamically Self-assembling Nanoparticles with Toggled Interactions. *Langmuir* **2018**, *34*, 1029–1041.

[21] Liu, A. J.; Nagel, S. R. Jamming Is Not Just Cool Any More. *Nature* **1998**, *396*, 21.

[22] Trappe, V.; Prasad, V.; Cipelletti, L.; Segre, P. N.; Weitz, D. A. Jamming Phase Diagram for Attractive Particles. *Nature* **2001**, *411*, 772.

[23] Colombo, J.; Del Gado, E. Stress Localization, Stiffening, and Yielding in a Model Colloidal Gel. *J. Rheol.* **2014**, *58*, 1089–1116.

[24] Koumakis, N.; Moghimi, E.; Besseling, R.; Poon, W. C. K.; Brady, J. F.; Petekidis, G. Tuning Colloidal Gels by Shear. *Soft Matter* **2015**, *11*, 4640–4648.

[25] Landrum, b. J.; Russel, w. B.; Zia, r. N. Delayed Yield in Colloidal Gels: Creep, Flow, and Re-entrant Solid Regimes. *J. Rheol.* **2016**, *60*, 783–807.

[26] Johnson, L. C.; Landrum, B. J.; Zia, R. N. Yield of Reversible Colloidal Gels during Flow Start-up: Release from Kinetic Arrest. *Soft Matter* **2018**, *14*, 5048–5068.

[27] Bechinger, C.; Di Leonardo, R.; Löwen, H.; Reichhardt, C.; Volpe, G.; Volpe, G. Active Particles in Complex and Crowded Environments. *Rev. Mod. Phys.* **2016**, *88*, 045006.

[28] Takatori, S. C.; Brady, J. F. Forces, Stresses and the (thermo?) Dynamics of Active Matter. *Curr. Opin. Colloid Interface Sci.* **2016**, *21*, 24–33.

[29] Mallory, S. A.; Valeriani, C.; Cacciuto, A. An Active Approach to Colloidal Self-assembly. *Annu. Rev. Phys. Chem.* **2018**, *69*, 59–79.

[30] Takatori, S. C.; Yan, W.; Brady, J. F. Swim Pressure: Stress Generation in Active Matter. *Phys. Rev. Lett.* **2014**, *113*, 028103.

[31] Fily, Y.; Henkes, S.; Marchetti, M. C. Freezing and Phase Separation of Self-propelled Disks. *Soft Matter* **2014**, *10*, 2132–2140.

[32] Solon, A. P.; Stenhammar, J.; Wittkowski, R.; Kardar, M.; Kafri, Y.; Cates, M. E.; Tailleur, J. Pressure and Phase Equilibria in Interacting Active Brownian Spheres. *Phys. Rev. Lett.* **2015**, *114*, 198301.

[33] Redner, G. S.; Baskaran, A.; Hagan, M. F. Reentrant Phase Behavior in Active Colloids with Attraction. *Phys. Rev. E* **2013**, *88*, 012305.

[34] Prymidis, V.; Sielcken, H.; Filion, L. Self-assembly of Active Attractive Spheres. *Soft Matter* **2015**, *11*, 4158–4166.

[35] Mallory, S. A.; Cacciuto, A. Activity-assisted Self-assembly of Colloidal Particles. *Phys. Rev. E* **2016**, *94*, 022607.

[36] Mallory, S. A.; Alarcon, F.; Cacciuto, A.; Valeriani, C. Self-assembly of Active Amphiphilic Janus Particles. *New J. Phys.* **2017**, *19*, 125014.

[37] Massana-Cid, H.; Codina, J.; Pagonabarraga, I.; Tierno, P. Active Apolar Doping Determines Routes to Colloidal Clusters and Gels. *Proc. Natl. Acad. Sci. USA* **2018**, *115*, 10618–10623.

[38] Ni, R.; Cohen Stuart, M. A.; Dijkstra, M.; Bolhuis, P. G. Crystallizing Hard-sphere Glasses by Doping with Active Particles. *Soft Matter* **2014**, *10*, 6609–6613.

[39] Stenhammar, J.; Wittkowski, R.; Marenduzzo, D.; Cates, M. E. Activity-induced Phase Separation and Self-assembly in Mixtures of Active and Passive Particles. *Phys. Rev. Lett.* **2015**, *114*, 018301.

[40] Takatori, S. C.; Brady, J. F. A Theory for the Phase Behavior of Mixtures of Active Particles. *Soft Matter* **2015**, *11*, 7920–7931.

[41] Cates, M. E.; Tailleur, J. Motility-induced Phase Separation. *Annu. Rev. Condens. Matter Phys.* **2015**, *6*, 219–244.

[42] Berg, H. C. *Random Walks in Biology*; Princeton University Press, 1993.

[43] Zaccarelli, E.; Lu, P. J.; Ciulla, F.; Weitz, D. A.; Sciortino, F. Gelation As Arrested Phase Separation in Short-ranged Attractive Colloid-polymer Mixtures. *J. Phys. Condens. Matter* **2008**, *20*, 494242.

[44] Fily, Y.; Marchetti, M. C. Athermal Phase Separation of Self-propelled Particles with No Alignment. *Phys. Rev. Lett.* **2012**, *108*, 235702.

[45] Sokolov, A.; Apodaca, M. M.; Grzybowski, B. A.; Aranson, I. S. Swimming Bacteria Power Microscopic Gears. *Proc. Natl. Acad. Sci. USA* **2010**, *107*, 969–974.

[46] Takatori, S. C.; Brady, J. F. Towards a Thermodynamics of Active Matter. *Phys. Rev. E* **2015**, *91*, 032117.

[47] Yan, W.; Brady, J. F. The Force on a Boundary in Active Matter. *J. Fluid Mech.* **2015**, *785*.

[48] Saintillan, D. Rheology of Active Fluids. *Annu. Rev. Fluid Mech.* **2018**, *50*, 563–592.

[49] Anderson, J. L. Colloid Transport by Interfacial Forces. *Annu. Rev. Fluid Mech.* **1989**, *21*, 61–99.

[50] Brady, J. F. Particle Motion Driven by Solute Gradients with Application to Autonomous Motion: Continuum and Colloidal Perspectives. *J. Fluid Mech.* **2011**, *667*, 216–259.

[51] Szakasits, M. E.; Zhang, W.; Solomon, M. J. Dynamics of Fractal Cluster Gels with Embedded Active Colloids. *Phys. Rev. Lett.* **2017**, *119*, 058001.

[52] Zia, R. N.; Landrum, B. J.; Russel, W. B. A Micro-mechanical Study of Coarsening and Rheology of Colloidal Gels: Cage Building, Cage Hopping, and Smoluchowski's Ratchet. *J. Rheol.* **2014**, *58*, 1121–1157.

[53] Van Doorn, J. M.; Bronkhorst, J.; Higler, R.; Van De Laar, T.; Sprakel, J. Linking Particle Dynamics to Local Connectivity in Colloidal Gels. *Phys. Rev. Lett.* **2017**, *118*, 188001.

[54] Tanaka, H.; Araki, T. Spontaneous Coarsening of a Colloidal Network Driven by Self-generated Mechanical Stress. *EPL* **2007**, *79*, 58003.

[55] Padmanabhan, P.; Zia, R. Gravitational Collapse of Colloidal Gels: Non-equilibrium Phase Separation Driven by Osmotic Pressure. *Soft Matter* **2018**, *14*, 3265–3287.

[56] Tailleur, J.; Cates, M. E. Statistical Mechanics of Interacting Run-and-tumble Bacteria. *Phys. Rev. Lett.* **2008**, *100*, 218103.

[57] Wittkowski, R.; Tiribocchi, A.; Stenhammar, J.; Allen, R. J.; Marenduzzo, D.; Cates, M. E. Scalar ϕ^4 Field Theory for Active-particle Phase Separation. *Nat. Commun.* **2014**, *5*, 4351.

[58] Solon, A. P.; Stenhammar, J.; Cates, M. E.; Kafri, Y.; Tailleur, J. Generalized Thermodynamics of Phase Equilibria in Scalar Active Matter. *Phys. Rev. E* **2018**, *97*, 020602(R).

[59] Paliwal, S.; Rodenburg, J.; Roij, R. V.; Dijkstra, M. Chemical Potential in Active Systems: Predicting Phase Equilibrium from Bulk Equations of State? *New J. Phys.* **2018**, *20*, 015003.

[60] Angelani, L.; Maggi, C.; Bernardini, M. L.; Rizzo, A.; Di Leonardo, R. Effective Interactions between Colloidal Particles Suspended in a Bath of Swimming Cells. *Phys. Rev. Lett.* **2011**, *107*, 138302.

[61] Ray, D.; Reichhardt, C.; Reichhardt, C. J. O. Casimir Effect in Active Matter Systems. *Phys. Rev. E* **2014**, *90*, 013019.

[62] Parra-Rojas, C.; Soto, R. Casimir Effect in Swimmer Suspensions. *Phys. Rev. E* **2014**, *90*, 013024.

[63] Harder, J.; Mallory, S. A.; Tung, C.; Valeriani, C.; Cacciuto, A. The Role of Particle Shape in Active Depletion. *J. Chem. Phys.* **2014**, *141*, 194901.

[64] Ni, R.; Cohen Stuart, M. A.; Bolhuis, P. G. Tunable Long Range Forces Mediated by Self-propelled Colloidal Hard Spheres. *Phys. Rev. Lett.* **2015**, *114*, 018302.

[65] Smallenburg, F.; Löwen, H. Swim Pressure on Walls with Curves and Corners. *Phys. Rev. E* **2015**, *92*, 032304.

[66] Asakura, S.; Oosawa, F. On Interaction between Two Bodies Immersed in a Solution of Macromolecules. *J. Chem. Phys.* **1954**, *22*, 1255–1256.

[67] Asakura, S.; Oosawa, F. Interaction between Particles Suspended in Solutions of Macromolecules. *J. Polym. Sci.* **1958**, *33*, 183–192.

[68] Lekkerkerker, H. N.; Tuinier, R. *Colloids and the Depletion Interaction*; Springer, 2011.

[69] Tanaka, H. Viscoelastic Phase Separation. *J. Phys.: Condens. Matter* **2000**, *12*, R207–R264.

[70] Shimizu, R.; Tanaka, H. A Novel Coarsening Mechanism of Droplets in Immiscible Fluid Mixtures. *Nat. Commun.* **2015**, *6*, 7407.

[71] Peng, Y.; Lai, L.; Tai, Y.-s.; Zhang, K.; Xu, X.; Cheng, X. Diffusion of Ellipsoids in Bacterial Suspensions. *Phys. Rev. Lett.* **2016**, *116*, 068303.

[72] Burkholder, E. W.; Brady, J. F. Tracer Diffusion in Active Suspensions. *Phys. Rev. E* **2017**, *95*, 052605.

[73] Flemming, H.-C.; Wingender, J. The Biofilm Matrix. *Nat. Rev. Microbiol.* **2010**, *8*, 623.

[74] Heyes, D.; Melrose, J. Brownian Dynamics Simulations of Model Hard-sphere Suspensions. *J. Non-Newtonian Fluid Mech.* **1993**, *46*, 1–28.

[75] Anderson, J. A.; Lorenz, C. D.; Travesset, A. General Purpose Molecular Dynamics Simulations Fully Implemented on Graphics Processing Units. *J. Comput. Phys.* **2008**, *227*, 5342–5359.

[76] Glaser, J.; Nguyen, T. D.; Anderson, J. A.; Lui, P.; Spiga, F.; Millan, J. A.; Morse, D. C.; Glotzer, S. C. Strong Scaling of General-purpose Molecular Dynamics Simulations on Gpus. *Comput. Phys. Commun.* **2015**, *192*, 97–107.

[77] Foss, D. R.; Brady, J. F. Brownian Dynamics Simulation of Hard-sphere Colloidal Dispersions. *J. Rheol.* **2000**, *44*, 629–651.

[78] Patch, A.; Sussman, D. M.; Yllanes, D.; Marchetti, M. C. Curvature-dependent Tension and Tangential Flows at the Interface of Motility-induced Phases. *Soft Matter* **2018**, *14*, 7435–7445.

Chapter 5

INTERFACIAL MECHANICS OF ACTIVE MATTER

Purely repulsive active particles can phase separate into dilute and dense regions, a phenomenon that bears a striking resemblance to a traditional liquid-gas phase transition. The success of the active pressure in characterizing this phase behavior makes it all the more puzzling that this very same pressure results in defining a surface tension between the coexisting phases that is extremely *negative*, sharply contrasting with the observation of a mechanically stable interface. Here, we demonstrate that this contradiction stems from a misinterpretation of the swim stress as a true surface force. Rather, activity manifests in a momentum balance as a *body force* in the form of a swim force density that balances the traditional surface forces such as those that arise from interparticle interactions and Brownian motion. Upon using these surface forces we recover a physically plausible surface tension. Just as in the case of a gravitational body force, the swim force density can be absorbed into the definition of stress to define an "equivalent" stress – the active stress – which is the relevant mechanical quantity for a number of phenomena, including phase coexistence.

5.1 Introduction

The time-irreversible motion of self-propelling or "active" particles results in fascinating phenomena whose description is beyond the applicability of traditional equilibrium thermodynamics and statistical mechanics. While the development of a formal nonequilibrium statistical description of active particles remains an exciting and ongoing challenge [1–8], *mechanical descriptions* have proven to be a powerful tool in describing many of the seemingly confounding behaviors of active particles. Work, pressure and tension are well-defined mechanical concepts and can thus be computed for materials arbitrarily far from equilibrium.

In recent years, the pressure of active matter [9–12] has aided in the description of many phenomena including instabilities exhibited by expanding bacterial droplets [13], the dynamics of gels [14, 15] and membranes [16] embedded with active particles, and even the phase behavior of living systems [17]. Among the phenomena that active pressure has successfully described is the stability limit [18, 19, 19, 20] (the spinodal) of *purely repulsive* active particles which are

observed to phase separate into "liquid" and "gas-like" regions, commonly referred to as motility-induced phase separation [21, 22]. Yet upon using this same active pressure to compute a surface tension (cf., eq. (5.2)) between the coexisting phases, one alarmingly finds that it is *extremely negative* despite the presence of a stable interface.

The above issue raises a number of questions: is the active pressure the appropriate mechanical quantity within the interface? do we need to revisit the formulation of the microscopic expression for surface tension? and, are there other contributions that may mechanically stabilize the interface against such an unphysical surface tension? In this chapter, we provide insight into these questions by demonstrating that the active stress is not the surface force to be used in an interfacial momentum balance. Rather, activity manifests as a volumetric (e.g., body) force that induces spatial variations in the true surface forces. This body force can, in some cases, be expressed as the divergence of a tensor in which case an *equivalent* stress can be defined; it is this stress that is often the relevant mechanical quantity and is used throughout the active matter literature, but *should not* be used in the formulation of the surface tension.

The enabling concept that allows for a theory for the pressure of active matter can be understood quite simply. Consider a simple model for an overdamped active particle. Each particle exerts a constant self-propulsive force $\boldsymbol{F}^{\boldsymbol{swim}} = \zeta U_0 \boldsymbol{q}$ in a direction $\boldsymbol{q}$ in order to move at a speed U_0 in a medium of resistance ζ. The particle orientation $\boldsymbol{q}$ undergoes random reorientation events that result in a characteristic reorientation time τ_R and run length (the distance a particle travels before reorienting) of $U_0\tau_R$. On timescales longer than τ_R, these dynamics give rise to a diffusivity $D^{swim} = \zeta U_0^2 \tau_R/6$ (in 3D [23]) which can be entirely athermal in origin. This swim diffusivity results in a dilute suspension of active particles with number density n_0 exerting a single-body *diffusive* pressure on a boundary $\Pi^{swim} = n_0 \zeta U_0^2 \tau_R/6 = n_0 \zeta D^{swim}$ [9–11]. This diffusive pressure can be thought of as the nonequilibrium extension of the thermal osmotic pressure exerted by equilibrium Brownian colloids $\Pi^B = n_0 k_B T = n_0 \zeta D_T$ (where $k_B T$ is thermal energy and D_T is the Brownian diffusivity). By analogy to thermal systems, one can define an active energy scale $k_s T_s \equiv \zeta U_0^2 \tau_R/6$ such that $\Pi^{swim} = n_0 k_s T_s$ [18].

Unlike the diffusive pressure of thermal Brownian colloids (the nk_BT contribution to the total pressure), the swim pressure; (1) need not be isotropic (and is therefore more aptly described as a swim stress $\boldsymbol{\sigma}^{\boldsymbol{swim}}$ with $\Pi^{swim} = -\mathrm{tr}(\boldsymbol{\sigma}^{\boldsymbol{swim}})/3$) as the

direction of swimming could be biased (e.g., by an applied orienting field [24]); and (2) explicitly depends on the volume fraction ϕ of active particles. The latter effect is a consequence of interparticle interactions impeding a particle's ability to swim, reducing the actual swimming velocity (and thus, the run length and swim pressure) from the intrinsic swim speed U_0 with increasing particle concentration. We can include this effect as well as the influence of anisotropic swimming in the general expression for the local swim stress [11, 24] for particles interacting with isotropic conservative interactions (particle orientations $\boldsymbol{q}$ are independent):

$$\boldsymbol{\sigma}^{swim} = -\frac{\zeta U_0 U \tau_R}{2}\left[\boldsymbol{Q} + n\boldsymbol{I}/3\right], \tag{5.1}$$

where U is the magnitude of the particle velocity in the direction of swimming, $\boldsymbol{Q} = \int P(\boldsymbol{x},\boldsymbol{q})(\boldsymbol{qq} - \boldsymbol{I}/3)d\boldsymbol{q}$ is the traceless nematic order ($\boldsymbol{0}$ for an isotropic system), $n = \int P(\boldsymbol{x},\boldsymbol{q})d\boldsymbol{q}$ is the local number density, $P(\boldsymbol{x},\boldsymbol{q})$ is the probability density of an active particle having position $\boldsymbol{x}$ and orientation $\boldsymbol{q}$, and $\boldsymbol{I}$ is the identity tensor.

Active Phase Separation

The reduction in swim pressure with concentration occurs for large run lengths ($U_0\tau_R \gg a$ or $\mathrm{Pe}_R \equiv a/U_0\tau_R \ll 1$ where a is the particle radius) and can lead the total pressure or the "active pressure" (the sum of the swim pressure and any other sources of pressure, such as interparticle interactions) to become nonmonotonic. This mechanical instability manifests through the phase separation of active particles. Figure 5.1A illustrates a phase separated active matter simulation [25, 26] for highly persistent ($\mathrm{Pe}_R = 0.0025$), overdamped and non-Brownian active particles interacting with a steeply repulsive WCA [27] potential ($\mathrm{Pe}_S \equiv \zeta U_0 a/\epsilon = 0.01$ where the Lennard-Jones diameter is taken to be $2a$ and ϵ is the Lennard-Jones energy). The active dynamics are fully encapsulated in Pe_R and Pe_S, the latter of which will be held constant throughout this chapter. One immediately appreciates that the liquid region forms a stable spherical domain, tending to minimize the surface area.

While an interfacial or surface tension cannot be defined thermodynamically as the excess free energy for this driven system, one can define it *mechanically* [28] as the "minimum" work required to create a differential area (at fixed volume) of interface in a planar (slab) geometry, resulting in:

$$\gamma = -\int_{-\infty}^{+\infty}[\sigma_{zz} - \sigma_{yy}]dz, \tag{5.2}$$

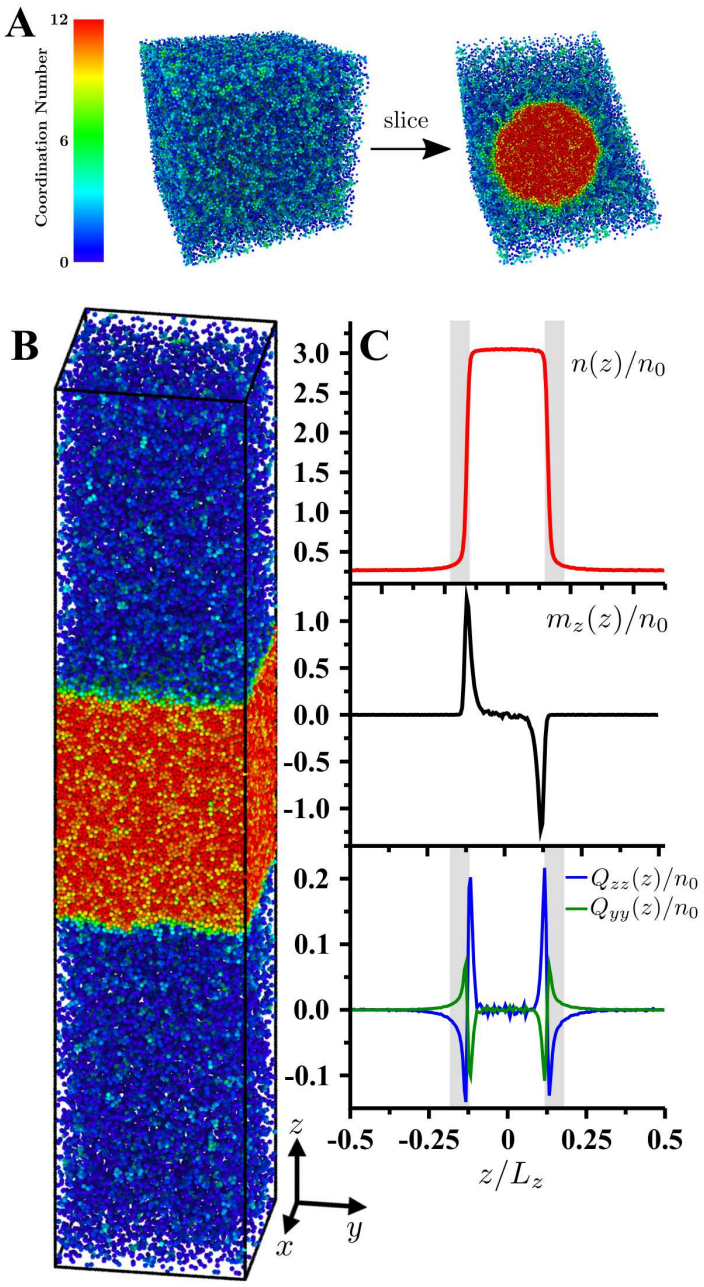

Figure 5.1: (A) A spherical active "liquid" droplet with a system total of 108000 active particles (volume fraction of $\phi = 4\pi a^3 n_0/3 = 0.14$ where n_0 is the number density) with $\mathrm{Pe}_R = 0.0025$ and $\mathrm{Pe}_S = 0.01$. (B) A characteristic simulation snapshot for $\mathrm{Pe}_R = 0.0025$ and $\phi = 0.15$ with 148716 particles and an asymmetric box with dimensions $L_z = 5L_x = 5L_y$. (C) The accompanying number density, polar order and nematic field profiles along the long axis (z) of the simulation cell. The data is translated such that the dense phase is centered along the long axis. Shaded regions represent the domains in which active particles are preferentially oriented tangential to the interface ($Q_{yy} > 0$).

where σ_{ij} are the components of the appropriate stress tensor $\boldsymbol{\sigma}$ and z is the direction normal to the interface. (σ_{xx} could be substituted for σ_{yy} without loss of generality due to the isotropy of the interface in the tangential directions. For finite-sized simulation with periodic boundaries, eq. (5.2) must be divided by two as there are two interfaces (see Fig. 5.1) and the integration limits are now the box size.) Upon defining the stress tensor as the sum of the swim stress and interparticle stress (we refer to this sum as the active stress, $\boldsymbol{\sigma^{act}} \equiv \boldsymbol{\sigma^{P}} + \boldsymbol{\sigma^{swim}}$), eq. (5.2) results in a surface tension that is *extremely negative* $\gamma = O(-nk_sT_sa)$ [29, 30], in striking contrast to our physical intuition that a mechanically stable interface must have a positive surface tension.

5.2 Stress Generation and the Active Interface

In a typical attractive colloidal or molecular fluid, there is an excess of tangential stress (i.e., $\sigma_{yy} > \sigma_{zz}$ and $\gamma > 0$) within the interface. In contrast, Bialké et al. [29] observed that within the low density region of the interface where $U \approx U_0$ (see the shaded regions in Fig. 5.1C), the particles are aligned tangential to the interface [31], generating a strongly anisotropic local swim stress ($|\sigma_{yy}^{swim}| \gg |\sigma_{zz}^{swim}|$ where both stresses are negative) and a negative surface tension.

The active interface, however, cannot simply be described by the density and nematic order: an unavoidable feature of the interface is that the particles, on average, point towards the liquid phase as particles pointing towards the gas are free to escape. This polarization of active particles can be quantified through the polar order defined as $\boldsymbol{m} = \int P(\boldsymbol{x}, \boldsymbol{q})\boldsymbol{q}d\boldsymbol{q}$ as is shown in Fig. 5.1C. This polarization of the particles results in volume elements within the interface having a *swim force density* $\zeta U_0 \boldsymbol{m}$. In the absence of particle currents, acceleration or any applied external forces, a simple point-wise momentum balance results in:

$$\nabla \cdot \boldsymbol{\sigma} + \zeta U_0 \boldsymbol{m} = \boldsymbol{0}, \tag{5.3}$$

where $\boldsymbol{\sigma}$ is the surface stress that must balance the force density created by the polarization of the active particles. Several works [20, 32–34] have derived the microscopic form of the above conservation equation, implicitly (explicitly in the case of Epstein et al. [32]) identifying $\boldsymbol{\sigma} = \boldsymbol{\sigma^{P}}$ as the traditional stress used in passive colloidal systems that arises due to interparticle interactions, Brownian motion, momentum diffusion, etc. Equation (5.3) suggests that these traditional surface stresses will adopt a spatial profile that precisely balances the swim force density, implying a pressure difference between the coexisting liquid and gas phases.

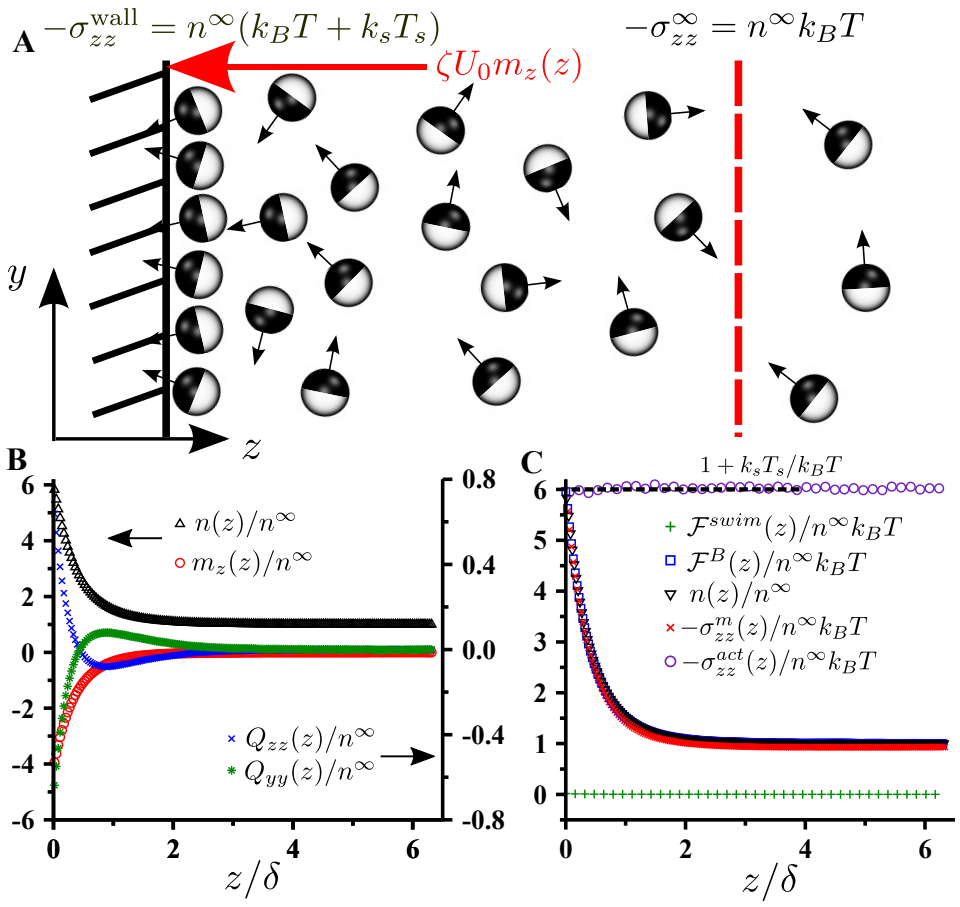

Figure 5.2: (A) A 2D schematic system of active Brownian particles near an impenetrable hard wall. For $k_sT_s/k_BT = 5$ (B) the number density, polar order and nematic fields and the (C) force flux, number density and local stress profiles.

To gain a physical intuition for the consequences of eq. (5.3), consider a simple 2D system of noninteracting active Brownian particles in the presence of an impenetrable wall with a normal in the $+z$-direction, shown schematically in Fig. 5.2A. The active particles accumulate on and orient towards the boundary (see Fig. 5.2B), forming a boundary layer with a thickness proportional to a microscopic length scale $\delta = \sqrt{D_T\tau_R}$ [34]. The presence of a swim force density $\zeta U_0 m_z$ within the boundary layer suggest that the stress *is not spatially constant*.

We can determine the spatial profile of the stress that is required to mechanically balance the swim force density by numerical integration of eq. (5.3), i.e. $-\sigma_{zz}^{m}(z) = \int_{z_{ref}}^{z} \zeta U_0 m_z(z')dz' - \sigma(z_{ref})$ (where $-\sigma(z_{ref} = 0)$ is the measured wall pressure). Figure 5.2C reveals that the stress profile is exactly the anticipated Brownian osmotic stress ($-\sigma_{zz}^{m} = n(z)k_BT$). In fact, this *must* be true as the flux of density n is

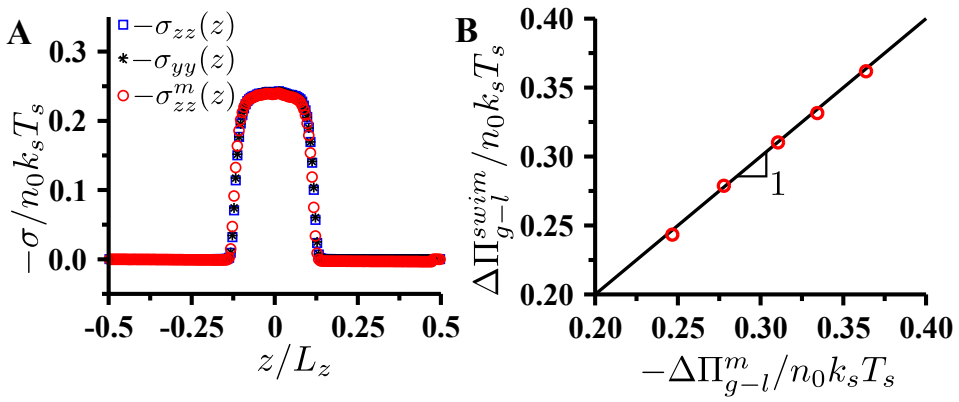

Figure 5.3: (A) The directly measured interparticle stress profile and the profile predicted through the integral of the swim force density for the identical system in Fig. 5.1C. (B) The difference in the swim pressure between the liquid and gas phases for various values of Pe_R.

zero everywhere $\boldsymbol{j_n} = -D_T\nabla n + U_0\boldsymbol{m} = 0$ which is equivalent to eq (5.3) with $\boldsymbol{\sigma} = \boldsymbol{\sigma}^P = -nk_BT\boldsymbol{I}$. Inserting an infinitely thin wall into the bulk region of the active particles, one would *instantaneously* measure a stress of $-\sigma_{zz} = n^\infty k_BT$. It is only after a time τ_R that the accumulation boundary layer forms and raises the traditional Brownian pressure (via an increase in density) at the wall to be $n^{wall}k_BT = n^\infty(k_BT + k_sT_s)$, which is the sum of the Brownian and swim pressure. However, the swim stress need not be directly invoked – the swim force density and Brownian stress are all that are needed to mechanically describe the system. This holds for our original system of interest; the measured particle stress (which now is entirely due to interparticle interactions) profile (Fig. 5.3A) exactly matches the stress profile obtained from integrating the swim force density.

The stress spatial profile can also be *explicitly* found through a method similar in spirit to the "method-of-planes" procedure [35] (see the Appendix for details). While the local stress generated by the Brownian force $-\mathcal{F}^B$ is precisely the anticipated Brownian osmotic stress $-n(z)k_BT$, the local stress generated by the swim force $-\mathcal{F}^{swim}$ is *negligible*. This as a consequence of the fact that the diffusivity of a swimmer – the previously argued origin of the swim stress generated by the particle – requires knowledge of the particle trajectory (in contrast with δ-correlated Brownian statistics) and thus cannot be known at an individual point in time (and, thus, space) which is consistent with the perspective offered by Speck and Jack [36].

How can we understand the absence of the swim stress from the above discussion yet its success in describing a host of behaviors? Let us now consider the steady-state conservation equation for the polar field which can readily be derived from the full

Smoluchowski equation [20, 33, 34, 37, 38] as:

$$-\nabla \cdot \boldsymbol{j_m} - \frac{2}{\tau_R}\boldsymbol{m} + \boldsymbol{\Gamma} = \boldsymbol{0}, \tag{5.4}$$

where Γ represents any externally applied sink or sources of the polar order (including torque-exerting boundaries [12, 38, 39]) and $-2\boldsymbol{m}/\tau_R$ is a natural sink that arises due to rotary diffusion of the active particles and the flux of polar order is $\boldsymbol{j_m} = U[\boldsymbol{Q} + n\boldsymbol{I}/3] - D_T\nabla\boldsymbol{m}$. Substituting the polar order conservation equation into eq. (5.3) gives:

$$\nabla \cdot \boldsymbol{\sigma^{act}} + \zeta U_0 \boldsymbol{\Gamma} = 0, \tag{5.5}$$

where $\boldsymbol{\sigma^{act}} = \boldsymbol{\sigma^P} - \frac{1}{2}\zeta\tau_R U_0 \boldsymbol{j_m} = \boldsymbol{\sigma^P} + \boldsymbol{\sigma^{swim}} + \frac{1}{2}\zeta\tau_R U_0 D_T \nabla\boldsymbol{m}$. Figure 5.2C illustrates that the 2D active pressure $-\sigma_{zz}^{act}$ (using $\boldsymbol{j_m}$ for 2D [34]) is indeed a constant and equal to the pressure at the wall. Note that in the absence of Brownian motion or strong gradients of polar order $\boldsymbol{\sigma^{act}} = \boldsymbol{\sigma^P} + \boldsymbol{\sigma^{swim}}$ and eq. (5.5) reduces to the continuum momentum balance derived by Yan and Brady [39].

It is crucial to appreciate that $\boldsymbol{\sigma^{act}}$ is no longer the system stress as it contains elements (those that could be expressed as a divergence of a tensor) from the original body force $\zeta U_0 \boldsymbol{m}$, recast as $\boldsymbol{\sigma^{swim}}$. The "true" stress remains $\boldsymbol{\sigma^P}$. This is analogous to the pressure field p of a static liquid of density ρ subject to a gravitational field g (acting in the $-z$-direction). The momentum balance for this system $\nabla p + \rho g = 0$ is often expressed as $\nabla\mathcal{P} = 0$ where $\mathcal{P} = p + \rho g z$ is often referred to as an "equivalent" pressure. One would obviously not conclude that the hydrostatic pressure is independent of the depth simply because $\mathcal{P}$ is a constant – the true pressure is p just as the true stress of active matter is encapsulated in $\boldsymbol{\sigma^P}$, with the swim stress playing a similar role as the gravitational potential $\rho g z$ [20]. A similar analogy can be made between the swim stress and the Maxwell stress in electrostatics, which represents the body force acting on charge density from an electric field [40].

Both the utility as well as the potential pitfalls of the active stress can be appreciated in the present context of active phase separation. In the absence of external sources/sinks of polar order (i.e., torques), eq. (5.5) suggests a convenient coexistence criterion of equal active pressures between the liquid and gas. Indeed, the difference in interaction pressure between the two phases is equal and opposite to the difference in their swim pressures (see Fig. 5.3B). Thus, utilizing the active stress perspective allows one to bypass resolving the polar order within microscopic boundary layers.

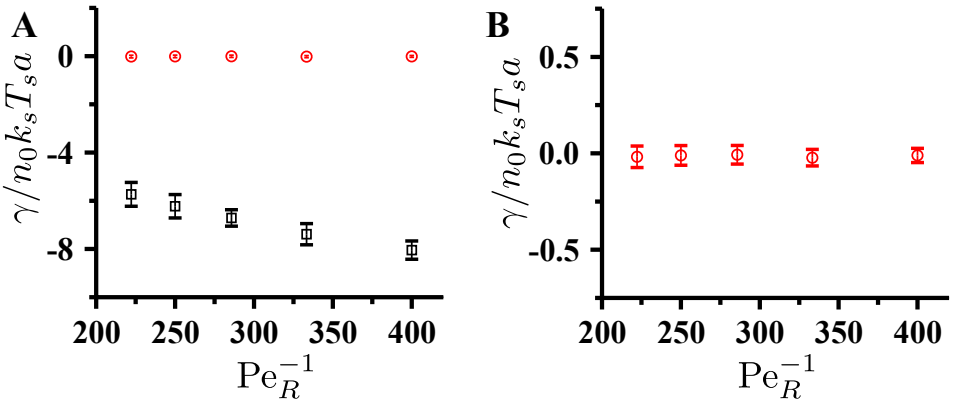

Figure 5.4: (A) The surface tension of active particles obtained through use of the true stress (○) of active particles (see (B) for a magnified view) in comparison to that obtained by using the active stress (□).

However, using the active stress to compute the surface tension results in the extremely negative interfacial tension (see Fig. 5.4A) that strongly contrasts with our physical observations. We can now recognize that this is because the surface tension requires the use of the true surface forces encapsulated in $\boldsymbol{\sigma}^{\boldsymbol{P}}$. By using the correct stress in eq. (5.2) (which remains valid in the presence of a body force (see Appendix), we find that the surface tension is almost negligible and displays little dependence on the level of particle activity. One can appreciate the smallness of γ through the nearly perfect isotropy in the stress (Fig. 5.3).

That the surface tension is vanishingly small (rather than significantly negative) is reassuring, but might suggest that the active interface should be quite volatile. We note that relating the interfacial height fluctuations of driven systems to surface tension using standard capillary wave theory (CWT) can be problematic as the theory is formulated using equilibrium statistical physics. Studies [29, 30, 41–43] on the interface of driven systems that have used CWT explicitly included thermal noise in their systems and implicitly made the ansatz that thermal fluctuations dominate over nonequilibrium effects, which clearly is not the case for our system (in fact, our system is athermal).

While directly relating interfacial height fluctuations to the surface tension is an outstanding challenge, we can begin to identify the physical contributions that would describe the forces resisting interfacial height fluctuation. The surface tension computed in this work (Fig. 5.4C) should be viewed as the *intrinsic surface tension* that penalizes the creation of interfacial area. Just as gravity reduces the capillary fluctuations of liquids [44, 45], we speculate that the swim force density localized

within the interface may also act to suppress height fluctuations. Unlike gravity, the swim force density is an *internal body force* (rather than externally imposed) and as such must be self-consistently computed to fully determine its influence on interfacial fluctuations. Furthermore, active particles are known to accumulate on convex surfaces and disperse from concave surfaces [30, 34, 46]. This migration effect naturally suppresses interfacial height fluctuations and is more akin to a bending stiffness than a surface tension. Finally, the anisotropic swimming within the interface bears similarities to the system investigated by Zia and Leung where the particles within the interface experienced an anistropic diffusivity with a larger diffusion in the tangential direction, which was found to suppress interfacial fluctuations [47].

5.3 Conclusions

Much remains to be explored in providing a complete mechanical description of an active interface. In showing that interfacial mechanics are described by the true stress $\boldsymbol{\sigma^P}$, we hope the present study clarifies the subtleties of using the active stress perspective. Just as in the case with any "effective stress", care must be exercised in interpreting the active stress as an actual stress. This is not to say that the active stress is without utility. On the contrary, $\boldsymbol{\sigma^{act}}$ allows one to readily compute the force exerted by active particles on a boundary without the need to resolve microscopic boundary layers (to find $\boldsymbol{m}$ within the boundary), as shown in the several examples explored by Yan and Brady [39] and in the case of phase coexistence. The question of which stress ($\boldsymbol{\sigma^{act}}$ or $\boldsymbol{\sigma^P}$) provides the appropriate level of description for a problem is a matter of the length scale of interest.

5.4 Appendix

Interacting, Athermal Active Particles

In all simulations except for those shown in Fig. 2 (the details for those simulations are provided below), the motion of particle i is governed by the overdamped Langevin equation $\boldsymbol{F_i^{swim}} + \sum_{j\neq i} \boldsymbol{F_{ij}^P} - \zeta \boldsymbol{U_i} = \boldsymbol{0}$ where $\boldsymbol{F_i^{swim}} = \zeta U_0 \boldsymbol{q_i}$ is the swim force, $\boldsymbol{F_{ij}^P}$ is interparticle force from particle j, and $\boldsymbol{U_i}$ is the instantaneous particle velocity. The orientation dynamics also follow an overdamped Langevin equation $\boldsymbol{L_i^R} - \zeta_R \boldsymbol{\Omega_i} = \boldsymbol{0}$ where $\boldsymbol{\Omega_i}$ is the angular velocity of $\boldsymbol{q_i}$, $\boldsymbol{L_i^R}$ is the random reorientation torque and ζ_R is the rotational drag. Note that the rotational drag has no dynamical consequences as we can rewrite the angular equation-of-motion as $\tilde{\boldsymbol{L}}_{\boldsymbol{i}}^{\boldsymbol{R}} - \boldsymbol{\Omega_i} = \boldsymbol{0}$ with a redefined torque $\tilde{\boldsymbol{L}}_{\boldsymbol{i}}^{\boldsymbol{R}}$ which has white noise statistics $\overline{\tilde{\boldsymbol{L}}_{\boldsymbol{i}}^{\boldsymbol{R}}} = \boldsymbol{0}$ and $\overline{\tilde{\boldsymbol{L}}_{\boldsymbol{i}}^{\boldsymbol{R}}(t)\tilde{\boldsymbol{L}}_{\boldsymbol{j}}^{\boldsymbol{R}}(0)} = 2\delta(t)\delta_{ij}\boldsymbol{I}/\tau_R$

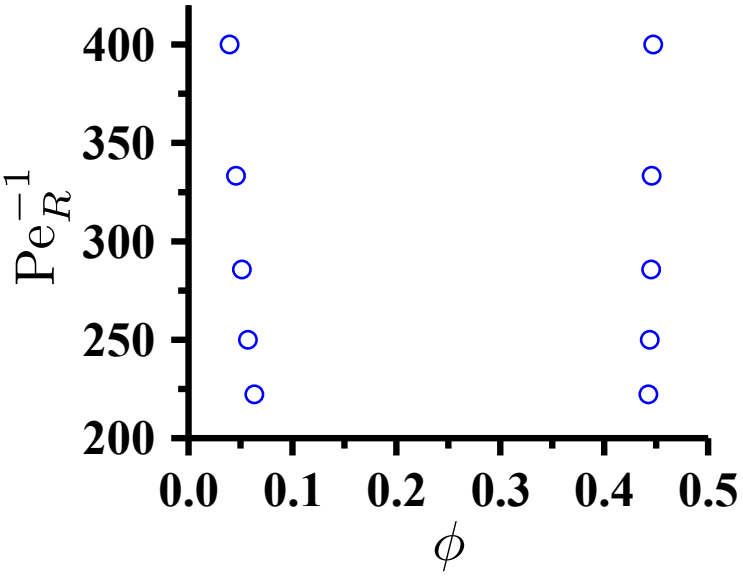

Figure 5.5: Region of the coexistence curve explored in this work (obtained via simulation).

where $\delta(t)$ and δ_{ij} are Dirac and Kroneker deltas, respectively. These orientation dynamics give rise to a rotational diffusivity τ_R^{-1} that need not be thermal in origin. We emphasize that these equations of motion are *entirely athermal* as we do not include (thermal) Brownian motion.

The interparticle force is derived from a steeply repulsive WCA potential [27] with an interaction energy ϵ and a Lennard-Jones diameter of $2a$. Dimensional analysis of the equations of motion reveals that the dynamics are completely described by the reorientation Péclet number $\mathrm{Pe}_R \equiv a/U_0\tau_R$ and a swim Péclet number $\mathrm{Pe}_S \equiv \zeta U_0 a/\epsilon$. The phase behavior of hardsphere active particles is entirely controlled by the run length of the particles (Pe_R) [18]. However, for finite particle softness there can additionally be a swim force (Pe_S) dependence and we therefore hold $\mathrm{Pe}_S = 0.01$ fixed as a control for all of our simulations.

For the isotropic simulation shown in Fig. 5.1A in the main text, the particles were initially placed in an FCC packing with a lattice constant of $3.47a$. The resulting crystal is centered within the simulation box and does not fill the entire box. This initial configuration biases the system towards rapidly forming a single liquid-droplet rather than multiple liquid domains scattered throughout the box. The latter situation would require longer simulation times to allow the isolated liquid domains to coalesce into a single drop. The simulation was run for a duration of $13000a/U_0$. For the slab geometries, the particles were initially placed in a space-spanning FCC packing with a reduced initial box size L_{z0} in the z-direction and a

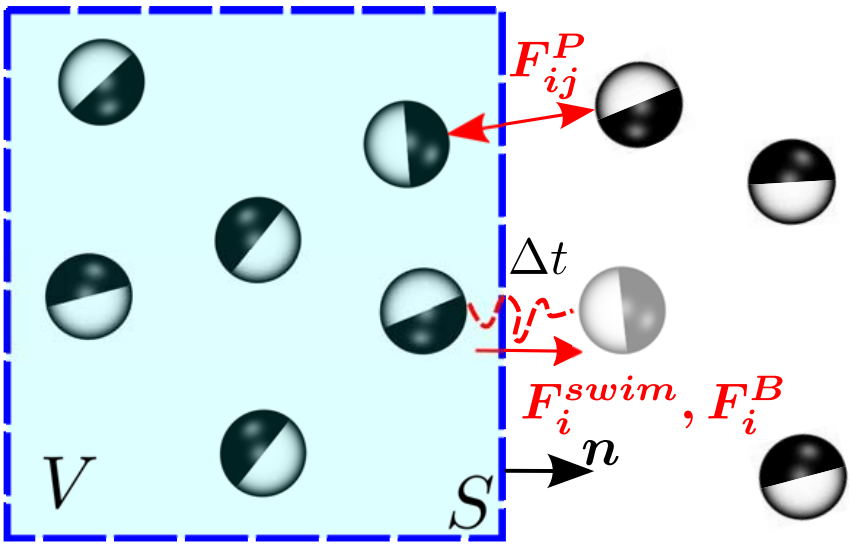

Figure 5.6: Schematic for computing the local stress (flux of force across a plane).

final box size of $L_z = 2.66L_{z0}$. The box is symmetrically elongated about the z-axis at a speed of $\approx 0.25U_0$ until a length of L_z is achieved. This procedure again biases the formation of a single liquid domain. Upon reaching the final box size, the system is evolved for $\approx 9000a/U_0$. The data displayed in the figures of the main text are the block average of data collected during the final $2000a/U_0$ of the simulations and error bars represent the standard deviation of the data sampled over this time. All simulations were performed using the GPU-enabled HOOMD-blue molecular dynamics package [25, 26].

The interaction stress $\boldsymbol{\sigma}^P$ was computed using the standard virial approach with $\boldsymbol{\sigma}^P = -n\langle \boldsymbol{x}_{ij}\boldsymbol{F}_{ij}^{\boldsymbol{P}}\rangle$ where $\boldsymbol{x}_{ij}$ is the distance between particles i and j, n is the local number density of the system, and the brackets denote an ensemble average over all particle pairs. The local swim stress is computed using eq. (5.1) in the main text. The local number density, polar order, nematic order and stress profiles are found by dividing the slab geometry into bins of thickness $\delta z \approx 2.4a$ in the z-direction and averaging over the particles within each bin. The swim pressure difference between the liquid and gas phases shown in Fig. 3B were found using the local value of the swim stress in the two phases for various values of Pe_R. The region of the coexistence curve examined is shown in Fig. 5.5.

Noninteracting Active Brownian Particles

The system simulated in Fig. 5.2 in the main text consisted of noninteracting $\boldsymbol{F}_{ij} = 0$ active Brownian particles (ABPs) with an equation of motion $\boldsymbol{F}_i^{swim} + \boldsymbol{F}^B + \boldsymbol{F}^{wall} -$

$\zeta \boldsymbol{U_i} = \boldsymbol{0}$ where we have now introduced a stochastic Brownian force with white noise statistics $\overline{\boldsymbol{F^B}} = \boldsymbol{0}$ and $\overline{\boldsymbol{F_i^B}(t)\boldsymbol{F_j^B}(0)} = 2k_BT\zeta\delta(t)\delta_{ij}\boldsymbol{I}$. The presence of an impenetrable wall is reflected in the force the wall must exert on a particle to prevent it from penetrating the boundary. The reorientation dynamics are identical to those described for the interacting system described above. We choose to simulate a system with modest activity ($k_sT_s/k_BT = 5$) such that we can easily resolve the boundary layer which becomes increasingly thin with increasing activity [34].

The local pressure – the flux of force across the surface S of a control volume V (cf. Fig. 5.6)– exerted by ABPs was computed in Fig. 5.2A in the main text by making the following elemental arguments. From a thermodynamic perspective, the ideal Brownian osmotic pressure of colloids $\Pi^B = nk_BT$ is the result of the translational entropy of the particles. However, mechanically, this pressure manifests in different ways depending on the details of the particle dynamics. In the case of colloidal particles *with inertia* Π^B arises from the momenta of the particles with $\Pi^B = n\langle m\boldsymbol{U}\cdot\boldsymbol{U}/2\rangle$ where m is the mass of the particle and $\langle ...\rangle$ represents an average over all particles. From equipartition it follows that $\Pi^B = nk_BT$.

In the case of overdamped dynamics, the particle momentum is ill-defined and the Brownian osmotic pressure must be thought of us a *diffusive pressure*. To see this, we use the standard virial approach for computing the stress (e.g., taking the first spatial moment of the Brownian force) and find $\Pi^B = n\langle \boldsymbol{x}\cdot\boldsymbol{F^B}\rangle = n\zeta\int\langle \boldsymbol{U^B}(t')\cdot\boldsymbol{U^B}(t)\rangle dt$ where we now recognize $\int\langle \boldsymbol{U^B}(t')\cdot\boldsymbol{U^B}(t)\rangle dt$ as the particle's Brownian diffusivity D^B and $\Pi^B = n\zeta D^B$. The Brownian velocity is trivially related to the Brownian force $\boldsymbol{U^B} = \boldsymbol{F^B}/\zeta$ and is therefore also δ-correlated in time. This has the important implication that the Brownian osmotic pressure can be measured at any instant in time as the diffusivity can be instantaneously measured, in contrast to the swim diffusivity of active matter which requires a duration of τ_R before it can be measured [10].

Computing the local pressure of interacting particles with inertia can be readily achieved using the method-of-planes procedure [35] which, in a nutshell, computes the sum of interparticle force acting across a surface (see Fig. 5.6) and the rate of change of momentum in the control volume due to particles entering and exiting the surfaces. Importantly, the latter two fluxes can be measured *instantaneously* at the surface. We now propose an extension of the method-of-planes procedure to measure the local stresses generated by single-body forces, such as the Brownian and swim forces.

As a particle moves across a surface with a Brownian F^B and swim force F^{swim}, it will exert a surface force on the particles in the neighboring control volume. We can compute this force by asking a simple question: what is the force required to keep the particles from crossing the imaginary surface plane? In other words, if the imaginary surface was an infinitely thin impenetrable wall, what force would the particles exert on the wall? This is precisely what we compute in Fig. 5.2 in the main text: at each simulate timestep we compute the force per unit area a hard wall would exert on the particles $\mathcal{F}$. The forces this hypothetical wall must exert to counteract the Brownian $\mathcal{F}^B$ and swim forces $\mathcal{F}^{swim}$ can be readily distinguished (with $\mathcal{F} = \mathcal{F}^B + \mathcal{F}^{swim}$). We note, however, that these quantities are not entirely decoupled as the frequency a particle crosses the surface is a function of both the Brownian and swim force. We further note that, as $\mathcal{F}$ should be interpreted as a local stress, its value is independent of which side of the hypothetical wall is used to measure it.

Single-body forces only contribute to surface-force flux *the instant* the particle is at the surface. It is for this reason that, when computing the swim force flux, we recover a local swim stress that is vanishingly small in comparison to the magnitude of the swim pressure. The swim diffusivity requires knowledge of the trajectory (the run length) of the particle. In contrast, the Brownian force at any instant in time fully encapsulates the Brownian diffusivity D_T of the particle and results in finding exactly the anticipated diffusive pressure $\mathcal{F}^B = n(z)\zeta D_T = n(z)k_BT$ at any instant in time and, hence, space, as shown in Fig. 5.2 in the main text.

Surface Tension Definition

Let us revisit the mechanical definition of surface tension in order to explore if a force density within the interface alters the traditional definition (eq. (5.2) in the main text). Consider a rectangular control volume within the interface, shown schematically in Fig. 5.7. The interfacial tension is typically defined as the work required to expand the box in the tangential (y and x) directions by a width δy while compressing the volume in the normal direction (z) by a width δz such that the total volume is conserved. The latter constraint results in $\delta y = -\delta z L_y/2L_z$ where L_y and L_z are shown schematically in Fig. 5.7. We note that the x and y directions are equivalent.

The work required to displace a surface of the control volume is directly proportional to the true surface stress acting on the surface of interest. The presence of a body

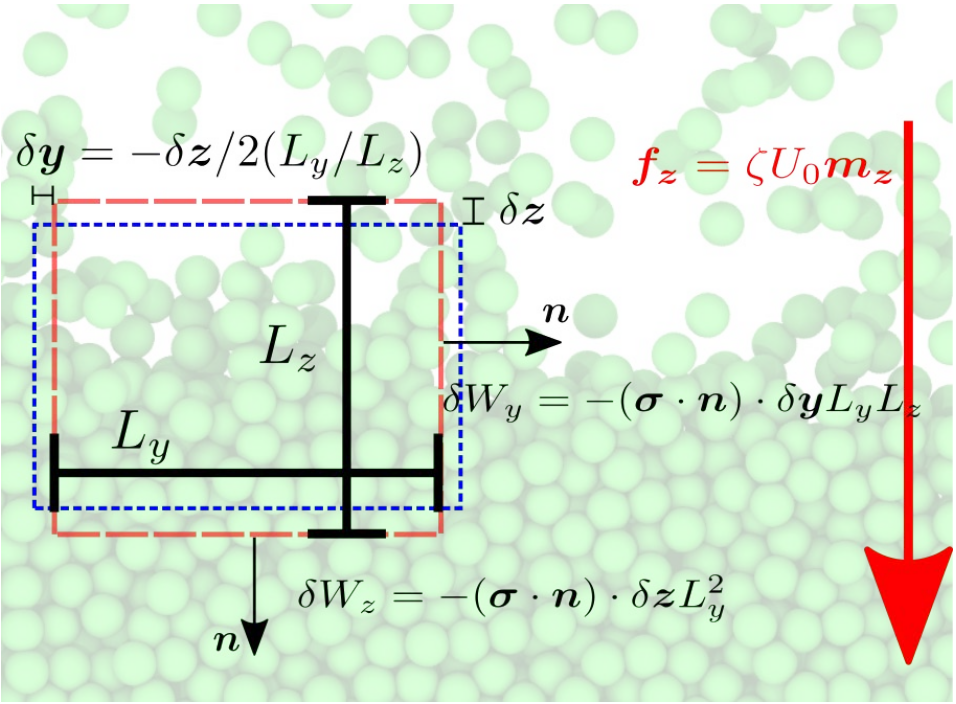

Figure 5.7: Schematic of the interfacial mechanical balance used to define the surface tension. The dashed red box represents a 2D projection of the original control volume and the dotted blue line represents the isochorically deformed volume.

force ($\zeta U_0 \boldsymbol{m}$) within the interface results in a normal stress σ_{zz} variation across the interface, a feature that distinguishes an active interface from traditional equilibrium interfaces which only exhibit tangential stress variation σ_{yy}. We therefore take the limit of $L_z \to dz$ (where dz is a differential length) such that now the local stresses are approximately constant across the control volume. Adding the work required to move each of the six faces of the now infinitesimal volume results in:

$$\delta W = -\delta A[\sigma_{zz} - \sigma_{yy}]dz, \tag{5.6}$$

where $\delta A = 2L_y \delta y$ is the change in tangential surface area of the system. We integrate this expression across the normal direction to obtain the total work required to expand the interface:

$$W = -\delta A \int_{-\infty}^{+\infty} [\sigma_{zz} - \sigma_{yy}]dz, \tag{5.7}$$

where we can now invoke that the definition of the interfacial tension as $W/\delta A$ with:

$$\gamma = -\int_{-\infty}^{+\infty} [\sigma_{zz} - \sigma_{yy}]dz, \tag{5.8}$$

where we assume that only a single interface is present within the system. This is identical to the traditional mechanical definition of surface tension and highlights that the presence of a body force has no *explicit* effect on the surface tension; it must be recalled, however, that σ_{zz} now varies across the interface due to the local swim force.

References

[1] Fodor, É.; Nardini, C.; Cates, M. E.; Tailleur, J.; Visco, P.; van Wijland, F. How Far from Equilibrium Is Active Matter? *Phys. Rev. Lett.* **2016**, *117*, 038103.

[2] Marconi, U. M. B.; Puglisi, A.; Maggi, C. Heat, Temperature and Clausius Inequality in a Model for Active Brownian Particles. *Sci. Rep.* **2017**, *7*, 46496.

[3] Puglisi, A.; Marini Bettolo Marconi, U. Clausius Relation for Active Particles: What Can We Learn from Fluctuations. *Entropy* **2017**, *19*, 356.

[4] Nardini, C.; Fodor, É.; Tjhung, E.; van Wijland, F.; Tailleur, J.; Cates, M. E. Entropy Production in Field Theories without Time-reversal Symmetry: Quantifying the Non-equilibrium Character of Active Matter. *Phys. Rev. X* **2017**, *7*, 021007.

[5] Mandal, D.; Klymko, K.; DeWeese, M. R. Entropy Production and Fluctuation Theorems for Active Matter. *Phys. Rev. Lett.* **2017**, *119*, 258001.

[6] GrandPre, T.; Limmer, D. T. Current Fluctuations of Interacting Active Brownian Particles. *Phys. Rev. E* **2018**, *98*, 060601(R).

[7] Shankar, S.; Marchetti, M. C. Hidden Entropy Production and Work Fluctuations in an Ideal Active Gas. *Phys. Rev. E* **2018**, *98*, 020604(R).

[8] Dabelow, L.; Bo, S.; Eichhorn, R. Irreversibility in Active Matter Systems: Fluctuation Theorem and Mutual Information. *Phys. Rev. X* **2019**, *9*, 021009.

[9] Fily, Y.; Henkes, S.; Marchetti, M. C. Freezing and Phase Separation of Self-propelled Disks. *Soft Matter* **2014**, *10*, 2132–2140.

[10] Takatori, S. C.; Yan, W.; Brady, J. F. Swim Pressure: Stress Generation in Active Matter. *Phys. Rev. Lett.* **2014**, *113*, 028103.

[11] Solon, A. P.; Stenhammar, J.; Wittkowski, R.; Kardar, M.; Kafri, Y.; Cates, M. E.; Tailleur, J. Pressure and Phase Equilibria in Interacting Active Brownian Spheres. *Phys. Rev. Lett.* **2015**, *114*, 198301.

[12] Solon, A.; Fily, Y.; Baskaran, A.; Cates, M.; Kafri, Y.; Kardar, M.; Tailleur, J. Pressure Is Not a State Function for Generic Active Fluids. *Nat. Phys.* **2015**, *11*, 673.

[13] Sokolov, A.; Rubio, L. D.; Brady, J. F.; Aranson, I. S. Instability of Expanding Bacterial Droplets. *Nat. Commun.* **2018**, *9*, 1322.

[14] Szakasits, M. E.; Zhang, W.; Solomon, M. J. Dynamics of Fractal Cluster Gels with Embedded Active Colloids. *Phys. Rev. Lett.* **2017**, *119*, 058001.

[15] Omar, A. K.; Wu, Y.; Wang, Z.-G.; Brady, J. F. Swimming to Stability: Structural and Dynamical Control via Active Doping. *ACS Nano* **2019**, *13*, 560–572.

[16] Paoluzzi, M.; Di Leonardo, R.; Marchetti, M. C.; Angelani, L. Shape and Displacement Fluctuations in Soft Vesicles Filled by Active Particles. *Sci. Rep.* **2016**, *6*, 34146.

[17] Sinhuber, M.; Ouellette, N. T. Phase Coexistence in Insect Swarms. *Phys. Rev. Lett.* **2017**, *119*, 178003.

[18] Takatori, S. C.; Brady, J. F. Towards a Thermodynamics of Active Matter. *Phys. Rev. E* **2015**, *91*, 032117.

[19] Solon, A. P.; Stenhammar, J.; Cates, M. E.; Kafri, Y.; Tailleur, J. Generalized Thermodynamics of Phase Equilibria in Scalar Active Matter. *Phys. Rev. E* **2018**, *97*, 020602(R).

[20] Paliwal, S.; Rodenburg, J.; Roij, R. V.; Dijkstra, M. Chemical Potential in Active Systems: Predicting Phase Equilibrium from Bulk Equations of State? *New J. Phys.* **2018**, *20*, 015003.

[21] Fily, Y.; Marchetti, M. C. Athermal Phase Separation of Self-propelled Particles with No Alignment. *Phys. Rev. Lett.* **2012**, *108*, 235702.

[22] Cates, M. E.; Tailleur, J. Motility-induced Phase Separation. *Annu. Rev. Condens. Matter Phys.* **2015**, *6*, 219–244.

[23] Berg, H. C. *Random Walks in Biology*; Princeton University Press, 1993.

[24] Takatori, S. C.; Brady, J. F. Swim Stress, Motion, and Deformation of Active Matter: Effect of an External Field. *Soft Matter* **2014**, *10*, 9433–9445.

[25] Anderson, J. A.; Lorenz, C. D.; Travesset, A. General Purpose Molecular Dynamics Simulations Fully Implemented on Graphics Processing Units. *J. Comput. Phys.* **2008**, *227*, 5342–5359.

[26] Glaser, J.; Nguyen, T. D.; Anderson, J. A.; Lui, P.; Spiga, F.; Millan, J. A.; Morse, D. C.; Glotzer, S. C. Strong Scaling of General-purpose Molecular Dynamics Simulations on Gpus. *Comput. Phys. Commun.* **2015**, *192*, 97–107.

[27] Weeks, J. D.; Chandler, D.; Andersen, H. C. Role of Repulsive Forces in Determining the Equilibrium Structure of Simple Liquids. *J. Chem. Phys.* **1971**, *54*, 5237–5247.

[28] Kirkwood, J. G.; Buff, F. P. The Statistical Mechanical Theory of Surface Tension. *J. Chem. Phys.* **1949**, *17*, 338–343.

[29] Bialké, J.; Siebert, J. T.; Löwen, H.; Speck, T. Negative Interfacial Tension in Phase-separated Active Brownian Particles. *Phys. Rev. Lett.* **2015**, *115*, 098301.

[30] Patch, A.; Sussman, D. M.; Yllanes, D.; Marchetti, M. C. Curvature-dependent Tension and Tangential Flows at the Interface of Motility-induced Phases. *Soft Matter* **2018**, *14*, 7435–7445.

[31] Lee, C. F. Interface Stability, Interface Fluctuations, and the Gibbs-Thomson Relationship in Motility-induced Phase Separations. *Soft Matter* **2017**, *13*, 376–385.

[32] Epstein, J. M.; Klymko, K.; Mandadapu, K. K. Statistical mechanics of transport processes in active fluids. II. Equations of hydrodynamics for active Brownian particles. *J. Chem. Phys.* **2019**, *150*, 164111.

[33] Solon, A. P.; Stenhammar, J.; Cates, M. E.; Kafri, Y.; Tailleur, J. Generalized thermodynamics of motility-induced phase separation: phase equilibria, Laplace pressure, and change of ensembles. *New J. Phys.* **2018**, *20*, 075001.

[34] Yan, W.; Brady, J. F. The Force on a Boundary in Active Matter. *J. Fluid Mech.* **2015**, *785*.

[35] Todd, B. D.; Evans, D. J.; Daivis, P. J. Pressure tensor for inhomogeneous fluids. *Phys. Rev. E* **1995**, *52*, 1627–1638.

[36] Speck, T.; Jack, R. L. Ideal Bulk Pressure of Active Brownian Particles. *Phys. Rev. E* **2016**, *93*, 062605.

[37] Saintillan, D.; Shelley, M. J. *Complex Fluids in Biological Systems*; Springer, 2015; pp 319–355.

[38] Fily, Y.; Kafri, Y.; Solon, A. P.; Tailleur, J.; Turner, A. Mechanical Pressure and Momentum Conservation in Dry Active Matter. *J. Phys. A: Math. Theor.* **2017**, *51*, 044003.

[39] Yan, W.; Brady, J. F. The Swim Force As a Body Force. *Soft Matter* **2015**, *11*, 6235–6244.

[40] Woodson, H. H.; Melcher, J. R. *Electromechanical Dynamics*; Wiley, 1968.

[41] Derks, D.; Aarts, D. G. A. L.; Bonn, D.; Lekkerkerker, H. N. W.; Imhof, A. Suppression of Thermally Excited Capillary Waves by Shear Flow. *Phys. Rev. Lett.* **2006**, *97*, 038301.

[42] Paliwal, S.; Prymidis, V.; Filion, L.; Dijkstra, M. Non-equilibrium Surface Tension of the Vapour-liquid Interface of Active Lennard-jones Particles. *J. Chem. Phys.* **2017**, *147*, 084902.

[43] del Junco, C.; Vaikuntanathan, S. Interface height fluctuations and surface tension of driven liquids with time-dependent dynamics. *J. Chem. Phys.* **2019**, *150*, 094708.

[44] Evans, R. The Nature of the Liquid-vapour Interface and Other Topics in the Statistical Mechanics of Non-uniform, Classical Fluids. *Adv. Phys.* **1979**, *28*, 143–200.

[45] Buff, F. P.; Lovett, R. A.; Stillinger, F. H. Interfacial Density Profile for Fluids in the Critical Region. *Phys. Rev. Lett.* **1965**, *15*, 621–623.

[46] Mallory, S. A.; Valeriani, C.; Cacciuto, A. Curvature-induced activation of a passive tracer in an active bath. *Phys. Rev. E* **2014**, *90*, 032309.

[47] Zia, R.; Leung, K.-t. Interfacial Correlation and Dispersion in a Non-equilibrium Steady State System. *J. Phys. A: Math. Gen.* **1991**, *24*, L1399.